

Measurement and Prediction of Texture Evolution During Processing: Application to Rolled
α-Uranium and Extruded Magnesium Alloys

A Thesis

Presented to
the faculty of the School of Engineering and Applied Science
University of Virginia

in partial fulfillment
of the requirements for the degree

Master of Science

by

Robert Klein

August

2016

APPROVAL SHEET

The thesis
is submitted in partial fulfillment of the requirements
for the degree of
Master of Science



AUTHOR

The thesis has been read and approved by the examining committee:

Sean Agnew

Advisor

Leonid Zhigilei

Baoxing Xu

Accepted for the School of Engineering and Applied Science:



Craig H. Benson, Dean, School of Engineering and Applied Science

August
2016

Acknowledgements

Funding for the uranium material research was provided by the Y-12 National Security Complex's Plant Directed Research and Development program. This work of authorship and those incorporated herein were prepared by Contractor as accounts of work sponsored by an agency of the United States Government. Neither the United States Government nor any agency thereof, nor Contractor, nor any of their employees, makes any warranty, express or implied, or assumes any legal liability or responsibility for the accuracy, completeness, use made, or usefulness of any information, apparatus, product, or process disclosed, or represents that its use would not infringe privately owned rights. Reference herein to any specific commercial product, process, or service by trade name, trademark, manufacturer, or otherwise, does not necessarily constitute or imply its endorsement, recommendation, or favoring by the United States Government or any agency or Contractor thereof. The views and opinions of authors expressed herein do not necessarily state or reflect those of the United States Government or any agency or Contractor thereof.

For the magnesium material research, the author would like to thank Dr. Amjad Javaid and the casting team at CanmetMATERIALS for casting the ZEK100 billets. The authors would also like to thank Lucian Blaga of CanmetMATERIALS for performing the extrusions. Funding for this magnesium material work was also provided by Natural Resources Canada through the Program of Energy Research and Development.

The author would like to thank the many collaborators involved in this research. Their contributions are highlighted at the beginning of each section.

Abstract:

The goal of this thesis research was to enhance the understanding of the property and texture evolution of non-cubic metals and alloys during industrial deformation processes: cold-rolling and hot extrusion.

Low-enriched uranium foil is a candidate target material for production of the medical isotope Tc-99m. To explore the effects of thermo-mechanical processing on these foils, surrogate depleted uranium foils were prepared for study by cold-rolling a cast plate to the target thickness with intermediate annealing steps. The post-rolling texture of the samples was measured by x-ray diffraction and their microstructure was examined by optical microscopy. Continuum finite element (FE) analysis, with an isotropic J_2 (von Mises) plasticity constitutive law, was used to simulate the strain history experienced by the material during rolling. This strain history was used as an input for viscoplastic self-consistent (VPSC) polycrystal plasticity simulations of texture evolution. The ultimate goal of the combined FE-VPSC framework is to allow the effect of variations in rolling process parameters on the texture to be predicted *a priori*. Measured texture data of uranium samples reveals that (020) poles will align with the rolling direction of the foil. An additional feature of the texture has the (002) poles aligning close to the normal direction of the foil, but tilted towards the transverse direction. Predicted textures via the FE-VPSC system capture the alignment of the (020) poles along the rolling direction, and predict that the (002) poles will align with the normal direction with a tilt towards the rolling direction. Comparison of predicted and measured textures with other texture data in the literature reveal that the effect of recrystallization must be considered.

The elastic and thermal properties were predicted based upon the functional forms of single crystal thermo-elastic properties and self-consistent polycrystal averaging. Plastic properties were predicted via VPSC's capability to generate yield surfaces and stress-strain curves based upon inputs consisting of the single crystal plastic behavior and a texture input. The property predictions reveal that

the resulting foil will exhibit near elastic isotropy, moderate thermal expansion anisotropy, and strong plastic anisotropy.

Magnesium alloy tubes offer an attractive combination of strength and density. However, their poor crushing behavior under axial loads has prevented their use in crash-sensitive automotive structures such as crush rails. Previous investigations suggest that it is possible to achieve dramatic modifications to both strength and ductility of magnesium alloys through a combination of alloying, grain refinement, and texture control. The texture evolution was predicted using the viscoplastic self-consistent (VPSC) crystal plasticity model, with strain path input from continuum-based FE simulations of extrusion. Magnesium alloy tube samples were created and post-extrusion textures were measured both by x-ray diffraction and electron backscatter diffraction. The measured textures had a combination of features commonly observed in extruded and rolled magnesium textures. Pole figure plots of these textures show the (00.2) poles aligning with the radial direction of the tube as well as the (10.0) poles sweeping from the extrusion direction to the hoop direction of the tubes. Crush testing of the tubes reveal that the WE43 magnesium alloy exhibits superior energy absorption. The crush behavior of the Mg alloy tubes is discussed in terms of their crystallographic texture. Textures from the WE43 samples contain additional features, with some (00.2) poles aligning 45° from the extrusion direction, as well as along the extrusion direction. These additional features orient favorably for basal slip deformation and impede c-type extension twinning, respectively. This situation in which the texture causes the sample to accommodate strain by slip rather than twinning mechanisms helps to explain the absence of a twinning-type plateau in the force versus displacement curves generated via the axial crush tests performed on the WE43 samples.

Table of Contents

Acknowledgements.....	iii
Abstract:.....	iv
Table of Contents.....	vi
List of Figures.....	viii
List of Tables.....	xv
Abbreviations & Symbols.....	xvi
1 Introduction.....	1
1.1 Cold Rolling of α -uranium Foils.....	1
1.2 Extrusion of Thin-walled Mg Components.....	3
2 Experimental Methods.....	5
2.1 Rolling of α -U Foils.....	5
2.2 Extrusion of Mg Tubes.....	5
2.3 Texture Measurement by X-Ray Diffraction.....	8
2.4 Microstructure characterization by Optical Microscopy and Electron Backscatter Diffraction.....	9
2.5 Axial Crush Testing.....	10
3 Simulation.....	12
3.1 ABAQUS.....	12
3.1.1 Three-Dimensional Rolling Model.....	12
3.1.3 Extrusion.....	23
3.1.4 Hydroforming of Irradiation Assembly.....	24

3.2 Crystal Plasticity Simulations and Property Prediction	27
3.2.1 Uranium – Rolling	27
3.2.2 Magnesium – Extrusion	28
4 Results and Discussion	29
4.1 Cold Rolling of Uranium	29
4.1.1 FE Model Results.....	29
4.1.2 Microstructure Results	31
4.2 Extrusion of Magnesium.....	44
4.2.1 Model Results	44
4.2.2 Microstructure Results	51
4.2.3 Axial Crush Results	62
5 Conclusions.....	68
5.1 Microstructure and Properties of Cold-rolled α -U Foil	68
5.3 Texture Control of Extruded Mg-Alloy Thin-Walled Tube Components	69
Appendix A: Experimental Pole Figures	70
A.1 DU Pole Figures.....	70
A.2 Mg Pole Figures	73
Appendix B: Cold Rolling FE Model Parameters.....	75
Appendix C: VPSC Model Parameters.....	78

List of Figures

Figure 1 - Schematic design of the extrusion press used to create thin-walled Mg alloy tube components. The starting material, location shown in blue, is extruded downwards.	6
Figure 2 - Schematic design of the extrusion tooling to create a round-tube. The punch and mandrel (purple) force the pierced-billet (starting position shown in gray) to form a tube as it passes through the punch (gold).	6
Figure 3 - Bridge-die used for the extrusion of thin-walled tube components visualized as a CAD schematic. The creation of four seams is apparent from the rendering.	7
Figure 4 - Top-hat extrusion rendered as a CAD drawing. Specimens used in this paper are the horizontal segment, which connects the two vertical portions. Dotted lines on the right show the cuts made to generate an investigated specimen.	8
Figure 5 – Experimental setup for an axial crush test being performed on a thin-walled Mg alloy tube component.	11
Figure 6 – Isometric rendering of the simulated foil exiting the roll-gap. The inset bordered with red provides a side, magnified view of the strain variations through the foil. The LE12 (in-plane shear component) color map shows near zero shear at the foil center and significant levels of shear (similar magnitude to the thinning strain imparted by the rolls) at the foil surface, for the level of friction explored in this case.	13
Figure 7 – Visualization of undeformed elements for the strip material. 8-node linear bricks are pictured with an aspect ratio of 0.01 if calculated as element thickness divided by element length along the rolling direction. The x-axis, shown in the bottom-left corner, contains the rolling direction.	14
Figure 8 – Results of the literature study pertaining to relevant values for the Coulomb coefficient of friction between the rollers and the strip material in the deformation process [21 – 25].	16
Figure 9 - Tracking of a material point in the EnSight software, visualized as a dark blue stream. From this removed visual perspective, it is impossible to show the small nuances of the material point's travel,	

but it is possible to determine the overall trajectory of the particle. The rigid rollers have been removed for an improved image. 17

Figure 10 - The strain in the normal direction for the fully deformed strip material along the entirety of its simulated length. 18

Figure 11 - The strain in the normal direction for the fully deformed strip material as viewed in the ABAQUS output viewer. 19

Figure 12 - The equivalent strain experienced by the elements midway through the workpiece, plotted against time. 20

Figure 13 - The CPU time necessary to simulate the corresponding element count, showing the results of the mesh refinement study performed on the two-dimensional cold rolling model. The quadratic fit has an r-squared value of 0.9999. 21

Figure 14 - ABAQUS schematic drawing of the irradiation target assembly model. The foil is contained between two aluminum tubes, each noted in the figure. 26

Figure 15 – Plots of the velocity gradient history for the L_{12} and L_{22} components for a material point trace at the midplane of the workpiece. 30

Figure 16 – Plots of the velocity gradient history for the L_{12} and L_{22} components for a material point trace at the surface of the workpiece. 30

Figure 17 – Polarized light optical micrograph, viewing the foil along the ND, with RD oriented along the horizontal axis, showing few twins in the equiaxed grains, impurity banding along RD and weaker banding along TD (vertical). 31

Figure 18 – Linear intercept calculation on the ND surface of the sample, yielding a 10.3 μm average diameter. Magnified section of a polarized light micrograph. Twin boundaries were not counted. 32

Figure 19 – Experimental texture, recalculated pole figure from complete ODF averaged across three foil samples. RD points upward, TD points right, and ND points out of the page. Intensity values are given as multiples of random (MRD), which is consistently used as the convention throughout the thesis. 33

Figure 20 – FE-VPSC texture from midplane material point trace (1 pass). RD points upward, TD points right, and ND points out of the page.....	34
Figure 21 - FE-VPSC texture from midplane material point trace (2 passes). RD points upward, TD points right, and ND points out of the page.....	35
Figure 22 - FE-VPSC texture from midplane material point trace (3 passes). RD points upward, TD points right, and ND points out of the page.....	35
Figure 23 – FE-VPSC texture from surface material point trace. RD points upward, TD points right, and ND points out of the page.....	35
Figure 24 - FE-VPSC texture from surface material point trace (2 passes). RD points upward, TD points right, and ND points out of the page.....	36
Figure 25 - FE-VPSC texture from surface material point trace (2 passes). RD points upward, TD points right, and ND points out of the page.....	36
Figure 26 – Recontoured pole figure plots of the recrystallized texture of a rolled uranium sample from Lloyd et al. [32]. The recontouring was performed by Dr. Steiner. The RaD points upward, the TD points to the right, and ND faces out of the page.....	37
Figure 27 - The predicted coefficient of thermal expansion for single crystal (left) and polycrystal (right) α -uranium.....	38
Figure 28 - The predicted stiffness tensor values (C_{11} , C_{22} , C_{33}) for single crystal (left) and polycrystal (right).....	39
Figure 29 - The predicted stiffness tensor values (C_{44} , C_{55} , C_{66}) for single crystal (left) and polycrystal (right).....	39
Figure 30 - The predicted stiffness tensor values (C_{23} , C_{13} , C_{12}) for single crystal (left) and polycrystal (right).....	40
Figure 31 - VPSC based simulated curves of the stress-strain response of a random texture.....	41
Figure 32 - Relative activities for slip and twin systems plotted against strain for the case of tension (left) and compression (right) parallel to the ND for the random texture.....	41

Figure 33 - VPSC based simulated curves of stress-strain response of the experimentally measured foil texture.	42
Figure 34 - Relative activities for slip and twin systems plotted against strain for the case of tension (left) and compression (right) parallel to the ND for the foil texture.....	43
Figure 35 - π -plane projections of the yield surfaces for a random texture as well as the measured texture from the foil.	44
Figure 36 - Path line utilized to track deformation gradient during extrusion simulations from Profile #3. Contours of von Mises effective stress, max = 105 MPa. The color contouring represents von Mises effective stress, max = 105 MPa is colored red.	46
Figure 37 - Time evolution of the components of a) the deformation and b) the velocity gradient predicted from the simulation of Profile #3.....	47
Figure 38 - Path line utilized to track deformation gradient during extrusion simulations from Profile #8. Contours of von Mises effective stress, max = 105 MPa. The color contouring represents von Mises effective stress, max = 105 MPa is colored red.	48
Figure 39 - Time evolution of the components of a) the deformation and b) the velocity gradient predicted from the simulation of Profile #8.....	49
Figure 40 - Basal and prismatic pole figure resulting from the extrusion of Profile #3 with CRSS ratio of 1:6:6. RaD points upward, and ED points to the right.....	50
Figure 41 - Basal and prismatic pole figure resulting from the extrusion of Profile #8 with CRSS ratio of 1:6:6. RaD points upward, and ED points to the right.....	50
Figure 42 - Recalculated pole figures from the pre-extruded billet of AZ31B (a) and the as-cast ingot of ZEK100 (b). Pole figures are viewed down the axis of the samples (Note all of the Mg-alloy pole figures employ the same contouring and color spectrum).	52
Figure 43 - Recalculated pole figures for the AZ31B top-hat specimen at the a) surface and b) mid-plane. Pole figures plotted with the ND pointing upwards and the ED facing left.....	53

Figure 44 - Recalculated pole figures for the ZEK100 top-hat specimen at the a) surface texture and b) mid-plane. Pole figures plotted with the ND pointing upwards, and the ED facing left.	54
Figure 45 - Schematic representation of site locations for EBSD performed on the thin-walled tube of AZ31B.	56
Figure 46 - Schematic representation of site locations for EBSD performed on the thin-walled tube of ZEK100.....	56
Figure 47 - Extrusion direction (ED) inverse pole figure maps showing the microstructures of a) AZ31B and b) ZEK100 extruded tubes.	57
Figure 48 - Full pole figures recalculated from the complete ODF of an AZ31B thin-walled tube specimen. Pole figures plotted with the RaD points upwards, and the ED faces left.	58
Figure 49 - Full pole figures recalculated from the complete ODF of a ZEK100 thin-walled tube specimen. Pole figures plotted with the RaD pointing upwards, and the ED pointing left.....	58
Figure 50 - Extrusion direction (ED) inverse pole figure maps showing the microstructures of a) as-extruded WE43 and b) annealed WE43 extruded tubes.....	60
Figure 51 - Full pole figures recalculated from the complete ODF of an as-extruded WE43 thin-walled tube specimen. Pole figures plotted with the RaD pointing upwards, and the ED facing left.	61
Figure 52 - Full pole figures recalculated from the complete ODF of an annealed WE43 thin-walled tube specimen. Pole figures plotted with the RaD pointing upwards, and the ED facing left.	61
Figure 53 - Final specimen condition of the axial crush tests performed on AZ31B thin-walled tubes extruded at (from left to right): 250, 300, 350, 250 (and annealed), 300 (and annealed), and 350 and annealed.	62
Figure 54 - Final specimen condition of the axial crush tests performed on ZEK100 thin-walled tubes extruded at (from left to right): 275, 300, 450, 275 (and annealed), 300 (and annealed), and 450 and annealed.	62

Figure 55 - Final specimen condition of the axial crush tests performed on WE43 thin-walled tubes extruded at (from left to right): 350, 400, 450, 350 (and annealed), 400 (and annealed), and 450 and annealed. 63

Figure 56 - AZ31B Axial Crush Results displayed as a curve measuring force against displacement. Different lines represent the different processing history of the tubes subjected to the crush test. 64

Figure 57 - ZEK100 Axial Crush Results displayed as a curve measuring force against displacement. Different lines represent the different processing history of the tubes subjected to the crush test. 64

Figure 58 - WE43 Axial Crush Results displayed as a curve measuring force against displacement. Different lines represent the different processing history of the tubes subjected to the crush test. 65

Figure 59 - Portrays the figure of merit, energy absorption, as a function of alloy and processing history (extrusion temperature and anneal conditions). 67

Figure 60 - Experimentally measured texture of first DU foil sample via Cu radiation source. RD points upward, TD points right, and ND points out of the page. 70

Figure 61 - Experimentally measured texture of second DU foil sample via Cu radiation source. RD points upward, TD points right, and ND points out of the page. 70

Figure 62 - Experimentally measured texture of third DU foil sample via Cu radiation source. RD points upward, TD points right, and ND points out of the page. 71

Figure 63 - Experimentally measured texture of first DU foil sample via Mo radiation source. RD points upward, TD points right, and ND points out of the page. 71

Figure 64 - Experimentally measured texture of second DU foil sample via Mo radiation source. RD points upward, TD points right, and ND points out of the page. 72

Figure 65 - Experimentally measured texture of third DU foil sample via Mo radiation source. RD points upward, TD points right, and ND points out of the page. 72

Figure 66 - Experimentally measured texture of the DU foil samples. Generated via an averaged ODF across all three samples measured with Mo radiation. RD points upward, TD points right, and ND points out of the page. 73

Figure 67 - Strip sample configuration, viewed down the ED of the strips. Schematic is not drawn to scale, but rather to be illustrative of the series of radial cuts and flattening of the curved surface..... 73

Figure 68 - Recalculated pole figures from the complete ODF measured on an as-extruded WE43 sample.
..... 74

Figure 69 - Recalculated pole figures from the complete ODF measured on an as-extruded WE43 sample.
..... 74

Figure 70 - Elastic properties of the workpiece used in the cold rolling FE model of uranium [16]..... 75

Figure 71 - Tabular data, from the Holloman equation, for the plastic behavior of uranium [15] [17]..... 77

List of Tables

Table 1 - Extrusion temperature conditions for each of the Mg alloys used to create the thin-walled tube components.	7
Table 2 - Shows the number of elements employed and the computational cost of each degree of mesh refinement.	20
Table 3 - Description of extrusion simulation profiles	24

Abbreviations & Symbols

2D	Two-dimensional
3D	Three-dimensional
ALE	Adaptive Lagrangian-Eulerian
CAD	Computer aided design
CRSS	Critical Resolved Shear Stress
ED	Extrusion Direction
FEA	Finite Element Analysis
FEM	Finite Element Method
HD	Hoop Direction
K	Kelvin
Mg	Magnesium
MRD	Multiples of Random
ND	Normal Direction
PCYS	Polycrystal Yield Surface
RD	Rolling Direction
TD	Transverse Direction
(D)U	Depleted Uranium
VPSC	Viscoplastic Self-Consistent
wt%	Weight Percent
μ	Coefficient of Friction

Chapter I

1 Introduction

The goal of this thesis research was to enhance understanding of the property and texture evolution of advantageous materials during industrial deformation processes. This thesis is organized to present the parallel development of the research on uranium foils and thin-walled magnesium components. Both materials are first introduced in regards to their potential applications to demonstrate the motivation of further research into their property and texture evolution.

This thesis next details the creation of samples relevant to the thermo-mechanical processing history of interest. Both sets of samples had their texture evaluated via x-ray diffraction (XRD) while their microstructures were investigated with either optical microscopy or electron backscatter diffraction (EBSD). Following the experimental setup section, the thesis contains information on how each processing route was modeled via a continuum level approach with finite elements, followed by subsequent crystal plasticity modeling. The insight gained from this simulation methodology is then used to discuss the materials and their properties.

1.1 Cold Rolling of α -uranium Foils

This section partially adapted from, "Texture Measurement and Property Prediction of Rolled α -uranium," by Robert W. Klein, John R. Einhorn, Matthew Steiner, Christopher Calhoun, Elena Garlea, and Sean R. Agnew [1]. The author would like to thank Matthew Steiner for his help with assembling the background information and optical micrograph analysis, Christopher Calhoun for guidance in using the Viscoplastic Self-Consistent (VPSC) crystal plasticity code and generating elastic properties, John Einhorn for his assistance in texture measurements. Further, the author would like to thank Elena Garlea and Sean Agnew for providing direction and analysis of the data.

Uranium is vital in the production of certain radioactive isotopes, particularly Technetium-99m (Tc-99m), which is employed in medical diagnoses. Tc-99m's relatively short half-life of 6.02 hours makes it practical for medical applications, and its 140 keV γ -ray photons emitted during decay are ideal for efficient detection by scintillation instruments [2]. While a current technique utilizes neutron irradiation of highly enriched uranium (HEU) targets to produce molybdenum-99, the precursor to Tc-99m, there exists a desire to develop manufacturing methodologies for production of Tc-99m from low enriched uranium (LEU) [2]. Use of LEU constitutes a lower proliferation risk, in comparison with HEU.

A particular strategy of interest for production of Tc-99m involves the irradiation of LEU foils encased in Al tubes. Despite LEU targets producing less fission products, their relative lack of proliferation risk means they have less stringent export controls and can be irradiated in a larger fraction of the world's nuclear reactors [2] [3]. In principal, LEU targets result in a similar waste stream and a higher volume compared to HEU targets. However, additional waste can be mitigated by pursuing novel neutron irradiation target designs such as foil encasement.

In previous iterations of irradiating targets, uranium targets have been contained in silicide-aluminum mixtures, which not only contain the fission products, but facilitate cooling. Cladding LEU (or HEU foils) in a recoil barrier, placing the assembly between two Al tubes, and then closing the gap between the tubes by expanding the inner tube with hydraulic pressure would enable thermal contact such that heat could be removed during irradiation, as seen elsewhere [4 – 7]. The recoil barrier is constructed of Ni, which prevents the LEU foil from bonding with the tubes, whereas Al is selected for the tubes due to its small neutron absorption cross-section [4]. This sort of overall product could be disassembled post-irradiation, with the uranium foil product processed separately from the tubes, significantly reducing the waste stream.

The foil encasement method requires intimate contact of the foil within an Al tube in order to achieve particular temperatures by transferring heat to a surrounding water coolant. Physical gaps between the tube and clad foil can result during manufacture, heating, and irradiation. Uranium's anisotropic material properties increase the chance of gap development. In order to implement design or processing features to minimize the chance of gap creation, it is necessary to advance an understanding of how uranium's anisotropic properties develop through the rolling process.

The internal stress state of the irradiation target for production of technetium can either support or impede the assembly process as described in Govindarajan et al. [4]. The outer aluminum tube must be cut longitudinally for the retrieval of the uranium foil post-irradiation. Tensile residual stresses present in the outer aluminum will cause it to spring open upon being cut [4]. This facilitates retrieval of the foil, whereas compressive residual stresses will hinder the retrieval of the foil by causing the outer tube to collapse [4]. The finite element simulation developed by Govindarajan et al., recreated above, allows prediction of the residual stress state of the hydroformed assembly [4]. Changes in the processing conditions for the rolled α -uranium can impact the material parameters of the foil, and could hence impact the internal stress state of the assembly.

1.2 Extrusion of Thin-walled Mg Components

This section adapted from, "Exploration of Thin-walled Magnesium Alloy Tube Extrusion for Improved Crash Performance," by Robert W. Klein, Bruce W. Williams, Jonathan McKinley, John R. Einhorn, and Sean R. Agnew [5]. Further, this section contains material from, "Development of Thin-walled Magnesium Alloy Extrusions for Improved Crash Performance Based Upon Texture Control," by Bruce W. Williams, Sean R. Agnew, Robert W. Klein, and Jonathan McKinley [6]. The author would specifically like to thank Bruce Williams and Jonathan McKinley for their contributions in creating the Mg components, performing the axial crush tests, and developing a FE model for the extrusion process. Further, the author would like to thank John Einhorn for his assistance in the texture measurements, and Sean Agnew for his guidance in texture analysis.

Components made of Mg alloy offer an appealing combination of strength and density for use as structural components, notably in automobile construction. Despite these advantages, poor crushing behavior axially compressed tubes has thus far prevented their use in crash-sensitive automotive structures such as crush rails. This poor crushing behavior is rooted in the low room temperature compressive ductility of Mg alloys and is responsible for their low crash energy absorption [7]. Axial crush response is highly dependent upon the ductility of the material and can yield information regarding the acceptability of these components for use in automotive design.

Recent studies have helped develop the understanding of how texture in Mg components influences the mechanical properties of the material. For example, Chino et al. [8] and Orlov et al. [9] demonstrated that the texture of the material can influence the ductility of the material. Previous work suggests that different extrusion methods can yield a variety of resultant textures in Mg alloys [10]. Other investigators have begun to investigate precisely how Mg's mechanical properties can be tailored through different processing routes [11]. The research presented here was initiated to determine if the texture evolved during thin-walled extrusion of Mg alloys varies with from one alloy to the next, with impacts the final axial crush performance of the material.

Chapter II

2 Experimental Methods

2.1 Rolling of α -U Foils

A depleted uranium foil was manufactured at the Y-12 National Security complex. The foil began as a rectangular prism cast in a graphite mold with dimensions of approximately 2" x 4" x 0.5". It was then subjected to a series of cold rolls and annealing steps at 630 °C. Cold rolling was used to bring the material incrementally down to a thickness of near 270 μm before it was subjected to a final anneal step.

2.2 Extrusion of Mg Tubes

This section partially adapted from, "Exploration of Thin-walled Magnesium Alloy Tube Extrusion for Improved Crash Performance," by Robert W. Klein, Bruce W. Williams, Jonathan McKinley, John R. Einhorn, and Sean R. Agnew [5].

Three Mg alloys were selected for investigation: AZ31B, ZEK100, and WE43. Conventional alloy, AZ31B, containing 3wt% Al and 1wt% Zn is the most common Mg alloy used to fabricate extrusions. Alloy ZEK100, including 1wt% Zn, 0.2wt% rare earth elements (such as Ce or Nd), and 0.5% wt Zr, is of interest because this alloy has been shown to exhibit a unique texture, which in turn has led to improved mechanical properties such as formability, e.g., [12]. WE43 (4wt% Y, 3.2wt% rare-earth elements including a majority Nd, 0.41wt% Zr, 0.15wt% Li) has shown promise as an alloy selection for extruded parts intended for improved energy absorption under dynamic loading conditions [13].

A vertical extrusion press at CanmetMATERIALS (Figure 1) was utilized to extrude thin-walled Mg alloy components via three extrusion configurations: porthole-die, bridge-die, and conventional die [6]. An enhanced view of an example extrusion tooling for this system is depicted in Figure 2, in which a pre-extruded (AZ31B) or an as-cast (ZEK100 or WE43) billet of 88.9 mm can be extruded into thin-walled

components. The extrusions were all produced either at a rate of 254 mm/min, referred to as slow, or at a rate of 2032 mm/min, referred to as fast. Axial crush tests were performed on tube extruded at both rates, but all of the texture measurements and analysis were performed on samples extruded at the slower rate.

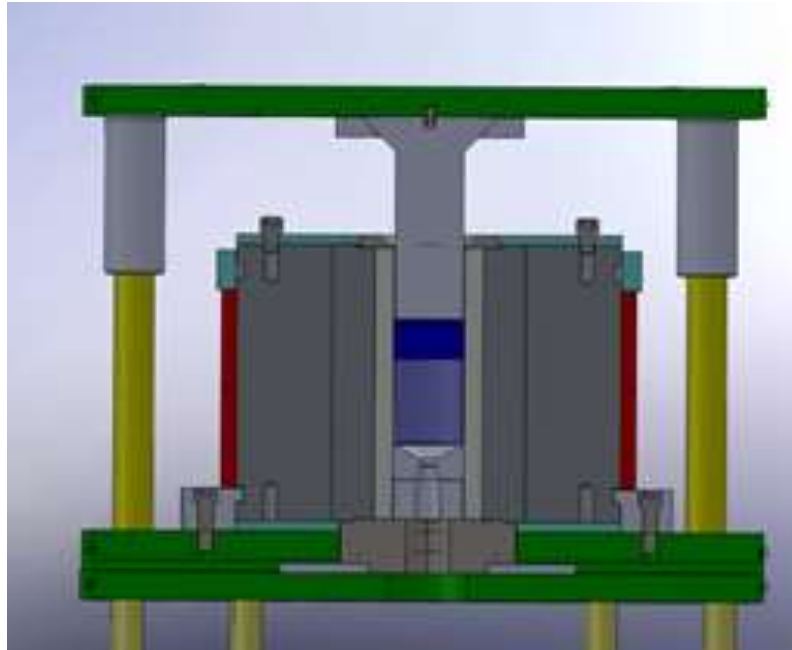


Figure 1 - Schematic design of the extrusion press used to create thin-walled Mg alloy tube components. The starting material, location shown in blue, is extruded downwards.

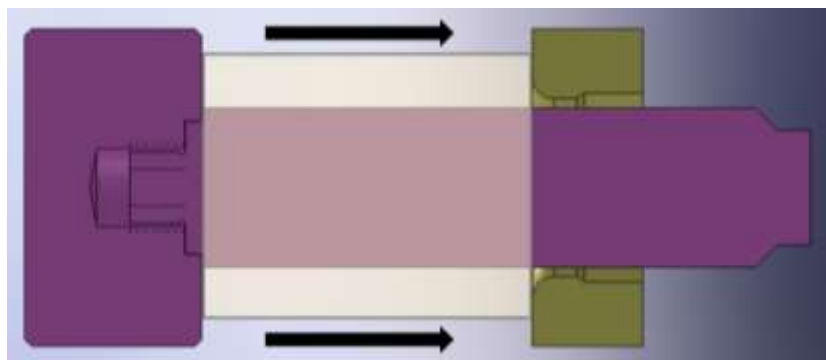


Figure 2 - Schematic design of the extrusion tooling to create a round-tube. The punch and mandrel (purple) force the pierced-billet (starting position shown in gray) to form a tube as it passes through the punch (gold).

Circular tubes with a wall-thickness of 2 mm and an outer diameter of 50 mm were extruded using a pierced billet and mandrel (Figure 2) which enforces an area reduction of 15:1 and results in a seamless

extrusion product or using a circular bridge-die, often referred to as a porthole-die [14] (Figure 3). The bridge-die enforces a higher extrusion ratio, 20:1, and creates a product with four extrusion seams. The focus of this research shifted towards the mandrel extrusion as previous studies revealed failures at the seams in tubes made using a bridge-die [14]. Technical difficulties with the extrusion of tubes through the bridge die, such as deformation of the bridges, made use of the mandrel expedient for the current study. Pierced billet extrusions were produced at a range of temperatures (Table 1), and studied in the as-extruded and annealed (450 °C for three hours) conditions.

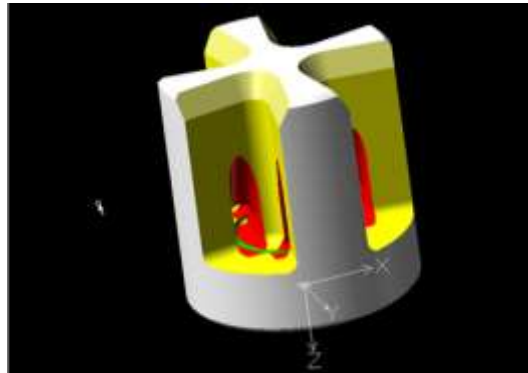


Figure 3 - Bridge-die used for the extrusion of thin-walled tube components visualized as a CAD schematic. The creation of four seams is apparent from the rendering.

Table 1 - Extrusion temperature conditions for each of the Mg alloys used to create the thin-walled tube components.

Alloy Name	AZ31B	ZEK100	WE43
Extrusion Temperature #1	250 °C	275 °C	350 °C
Extrusion Temperature #2	300 °C	300 °C	400 °C
Extrusion Temperature #3	350 °C	450 °C	450 °C

C-channel (top-hat) shaped extrusions with a wall-thickness of 2 mm, width of 40 mm, and height of 20 mm (Figure 4) were created using a conventional die from billets pre-heated to 400 °C. Notably, the

extrusion process used to create these components enforced an area reduction of about 80:1 from the billet's initial area of 254 cm². In Figure 4, a top-hat is visualized alongside a schematic showing how specimens were excised for texture measurement from the extruded component. Though the top-hat profiles have no extrusion seams, it should be noted that they must be welded together to create a final square tube. Although texture data was obtained from samples of this geometry, no tube crush tests were performed on the c-channel tubes.

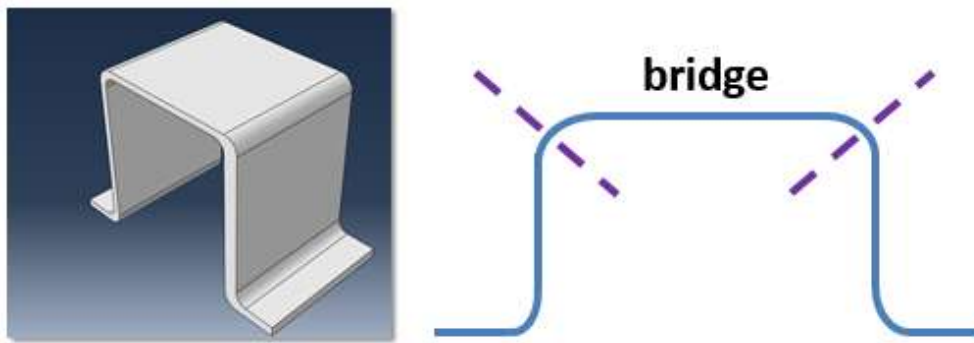


Figure 4 - Top-hat extrusion rendered as a CAD drawing. Specimens used in this paper are the horizontal segment, which connects the two vertical portions. Dotted lines on the right show the cuts made to generate an investigated specimen.

2.3 Texture Measurement by X-Ray Diffraction

This section partially adapted from, "Exploration of Thin-walled Magnesium Alloy Tube Extrusion for Improved Crash Performance," by Robert W. Klein, Bruce W. Williams, Jonathan McKinley, John R. Einhorn, and Sean R. Agnew and partially adapted from, "Texture Measurement and Property Prediction of Rolled α -uranium," by Robert W. Klein, John R. Einhorn, Matthew Steiner, Christopher Calhoun, Elena Garlea, and Sean R. Agnew [5] [6].

A PANalytical X'Pert Pro MPD powder diffractometer equipped with an open Eulerian cradle and a Cu K _{α} source was employed to measure the crystallographic texture of three distinct DU foil samples. The samples were cut in equal sizes across the width of the foil, allowing for comparison of different locations in the foil. Prior to measurements, the foils were dipped in a nitric acid bath in order to remove the oxide

layer on the foils. Incident radiation was put through a point-focus collimator with 1 mm x 2 mm (Shulz reflection geometry to minimize defocusing effects). The (110), (111), and (112) partial pole figures were all experimentally evaluated, and then the subsequent data were passed into the MATLAB toolbox known as MTEX, from which the complete orientation distribution functions (ODF) were calculated. For the first sample, the (131) partial pole figure was also collected, but its inclusion did not alter the ODF calculation, so its measurement for further samples was omitted. The complete (002), (020), and (200) pole figures were calculated using the ODF's for visualization of the texture.

The same PANalytical XRD was employed to measure the crystallographic texture of pre-extruded Mg material and C-channel Mg components. These samples received standard metallographic preparation consisting of mechanical and final chemical polishing (using a 5% nital solution). These measurements employed the same point-focus collimator as described for the DU sample measurements. Uncorrected, partial (up to 70°) (10.0), (10.1), and (00.2) pole figure data was measured and then imported into MTEX, from which full ODF's were calculated. Recalculated full (10.0) and (00.2) pole figures were generated using the calculated ODF's for visualization.

2.4 Microstructure characterization by Optical Microscopy and Electron

Backscatter Diffraction

Portions of this section are adapted from, "Texture Measurement and Property Prediction of Rolled α -uranium," by Robert W. Klein, John R. Einhorn, Matthew Steiner, Christopher Calhoun, Elena Garlea, and Sean R. Agnew [1]. Others are adapted from, "Exploration of Thin-walled Magnesium Alloy Tube Extrusion for Improved Crash Performance," by Robert W. Klein, Bruce W. Williams, Jonathan McKinley, John R. Einhorn, and Sean R. Agnew [5].

Optical microscopy samples were needed to characterize the microstructure of the uranium foils as alternate methods, such as electron backscatter diffraction, EBSD, would be too cumbersome given possible radioactive contamination. Three samples from the DU foil were separated off and then mounted

with their faces orthogonal to RD, TD, or ND. These samples were then polished to a mirror finish and allowed to oxidize in air. The microstructure was imaged via polarized light microscopy, with the anisotropic optical properties of the oxide layer providing orientation contrast.

Samples from the Mg thin-walled tube components were sectioned for characterization in a scanning electron microscope (SEM). An initial sample, from an AZ31B thin-walled tube, was cut along its extrusion axis, as imaged in Figure 45, so that study of its microstructure could reveal any potential gradients along the extrusion direction. Later samples were prepared by sectioning a small radial cut, represented in Figure 46, to investigate potential gradients along the radial direction. More details on these samples and the schematic illustrations for the sample preparation are available in Section 4.2.2 Microstructure Results.

A Quanta 650 Scanning Electron Microscope was used to experimentally measure the crystallographic texture of the Mg thin-walled tube components via EBSD with an accelerating voltage of 20 kV. Samples received standard metallographic preparation up to colloidal silica polish followed by ion polishing using a Hitachi IM4000. EBSD scans were run with a 1 μm step size over areas of 250 μm x 160 μm . EBSD data was also imported into MTEX, from which full ODF's were calculated. ODF's from the EBSD data were also plotted as full pole figures for the (10.0) and (00.2) planes to allow for best comparison with the other texture results.

2.5 Axial Crush Testing

This section adapted from, "Exploration of Thin-walled Magnesium Alloy Tube Extrusion for Improved Crash Performance," by Robert W. Klein, Bruce W. Williams, Jonathan McKinley, John R. Einhorn, and Sean R. Agnew [5].

Axial crush tests were performed on thin-walled tubes made of AZ31B, ZEK100, and WE43 Mg alloys.

Table 1 (from section 2.2) shows the extrusion conditions that were employed to make these tubes. Tubes

were tested in both the as-extruded and annealed condition. The tube length was about 160 mm and three crush initiators were placed at about the mid-length of the tube in a triangular pattern, in order to initiate the location of folding and reduce the peak load. All tubes were tested in a 225 kN press at a quasi-static displacement rate of 1 mm/s. The experimental setup is shown in Figure 5. Throughout the test, the load was measured as a function of displacement. Subsequently, the energy absorption of each tube was determined by integrating the load with respect to displacement, up to a total displacement of XXX mm.



Figure 5 – Experimental setup for an axial crush test being performed on a thin-walled Mg alloy tube component.

Chapter III

3 Simulation

3.1 ABAQUS

Finite element models of rolling and extrusion were developed using ABAQUS in order to predict the strain distribution during the deformation process. The end goal of this simulation was predicting crystallographic texture by interfacing with an existing viscoplastic self-consistent (VPSC) polycrystal plasticity code. Polycrystal modeling was also used to predict the anisotropic properties of the textured material. These properties can be fed back into an ABAQUS model to explore the impact of material anisotropy upon irradiation target performance.

3.1.1 Three-Dimensional Rolling Model

This section partially adapted from, "Texture Measurement and Property Prediction of Rolled α -uranium," by Robert W. Klein, John R. Einhorn, Matthew Steiner, Christopher Calhoun, Elena Garlea, and Sean R. Agnew [1].

The rolling process was investigated using both 3D and 2D models designed with two parts: a discrete, rigid surface with the shape of one of the rolls in the rolling mill and a deformable body. The deformable body's thickness dimension was assigned to be characteristic of the U foil employed in irradiation targets. Figure 6 provides a perspective of the overall model configuration, complete with an isometric rendering of the simulated foil exiting the roll-gap. Two rolling surfaces are visible because the symmetry conditions, discussed later in the document, are being visualized. The inset bordered with red provides a side, magnified view of the strain variations through the foil, which are the major objective of this modeling effort and will be described in detail below. The length and width of the foil were selected such that edge effects do not strongly influence the behavior of the material within the interior of the foil.

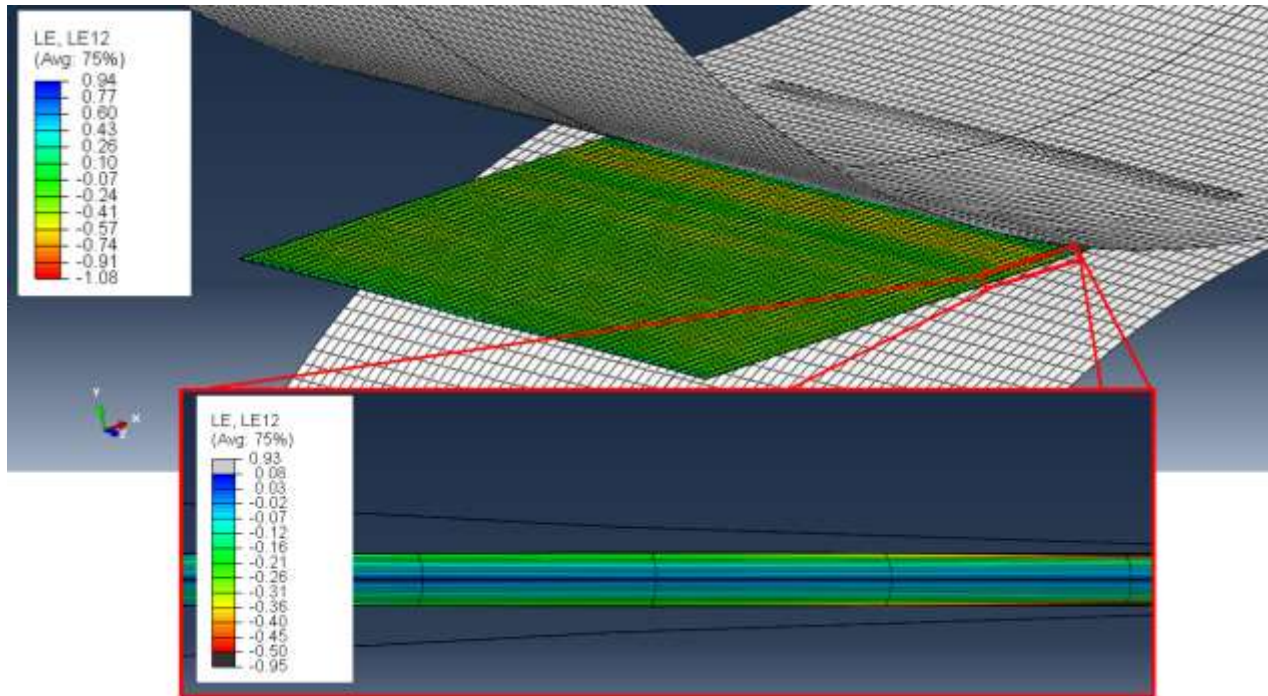


Figure 6 – Isometric rendering of the simulated foil exiting the roll-gap. The inset bordered with red provides a side, magnified view of the strain variations through the foil. The LE12 (in-plane shear component) color map shows near zero shear at the foil center and significant levels of shear (similar magnitude to the thinning strain imparted by the rolls) at the foil surface, for the level of friction explored in this case.

A rate independent, isotropic, elasto-plastic constitutive model fit to the behavior of α -uranium is used to describe the foil properties during cold rolling. [15] [16]. The overall form of a material model is a series of selection choices within the ABAQUS explicit software, where the physical property data (e.g. elastic moduli) are user-defined. Specifically, the traditional, multi-axial flow criterion known as J_2 plasticity was employed to describe yielding and flow of the workpiece. The hardening was assumed to be isotropic, and the parameters describing the effective flow stress versus the effective strain relation (Holloman equation) were obtained by fitting the behavior of the ND compression of an α -uranium plate at room temperature [17]. This constitutive modeling strategy ignores the effects of initial anisotropy as well as any anisotropy which may evolve during the rolling process. In particular, it ignores the possible effects that anisotropic crystal plasticity may have on strain localization. It further ignores the known, albeit low, strain rate sensitivity of U at room temperature [15]. It was assumed that the boundary conditions so constrain the deformation of the foil that these simplifications do not seriously undermine

the accuracy of the predictions. Modeling parameters for this FE simulation are available in detail in Appendix B.

Simulations were completed using 8-node linear brick, reduced integration, hourglass control elements from the explicit element library in ABAQUS, as shown in Figure 7. A symmetry boundary condition was enforced halfway through the thickness of the block. A z-axis symmetry boundary condition was also employed along one side of the workpiece. This symmetry condition was appropriate because the width of the material was so much greater than its thickness [18]. The z-axis symmetry boundary condition is inherent in a 2D simulation. However, in this initial 3D modeling effort was aimed at a comprehensive simulation, examining for possible edge effects along the free surface. Constant velocity was employed for both the initial movement of the block material and the boundary condition which constrains the rigid surface rotation, with values during model development set to be similar to other cold rolling cases in literature [18]. Ideal element size was determined through a dedicated mesh refinement study. Element thickness was held constant at 10% of foil thickness, while the length of each element along the rolling direction was adjusted.

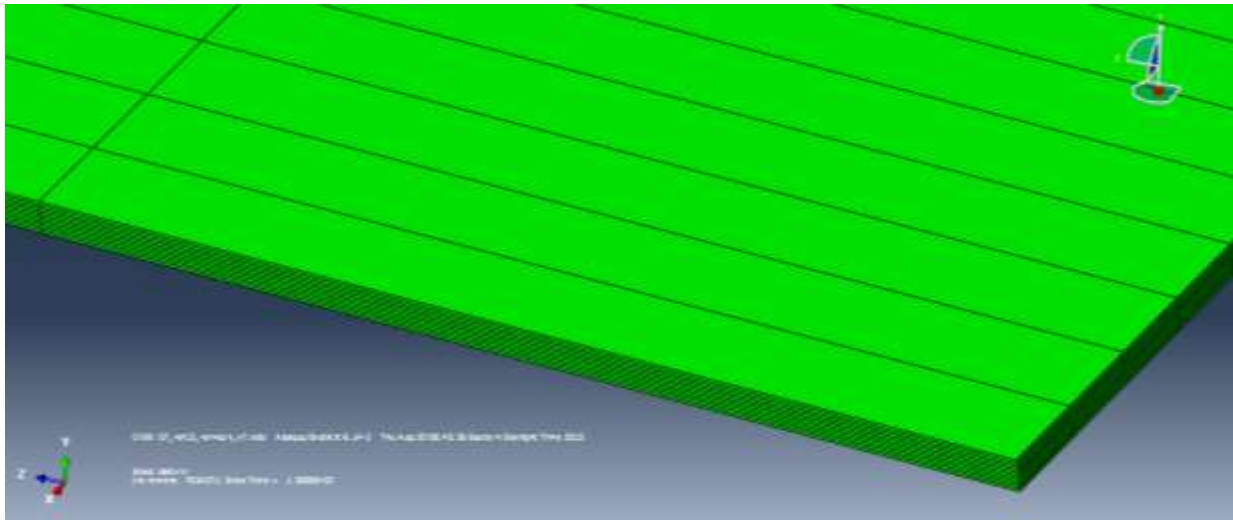


Figure 7 – Visualization of undeformed elements for the strip material. 8-node linear bricks are pictured with an aspect ratio of 0.01 if calculated as element thickness divided by element length along the rolling direction. The x-axis, shown in the bottom-left corner, contains the rolling direction.

Contact properties between the roller and the strip material were defined in the ABAQUS simulation to have both normal and tangential behavior. The selected normal behavior options minimized penetration of the strip material into the roller, and allowed the two surfaces to separate after contact (i.e. as the strip exits the roll gap). The tangential behavior of this contact was given a penalty formulation, which employed a Coulomb friction model. The value for the coefficient of friction was selected based on the results of a literature survey. As a value pertaining to the cold rolling of α -uranium was not available, a variety of other rolling processes were examined [21 – 25]. This survey, visualized in Figure 8, suggested that the actual coefficient of friction in a rolling process could take on a range of values, based upon numerous variables such as the roll speed, lubricant, and strip material. Based upon this literature survey, reasonable values vary from $\mu = 0.05$ to 0.35 . Due to this possible range of values, the finite element model was used to perform a parametric study of the impact of the coefficient of friction on the final condition of the deformed strip material. In order to capture the full possible range of behavior, three separate values were employed: $\mu = 0.05$, $\mu = 0.15$, and $\mu = 0.45$.

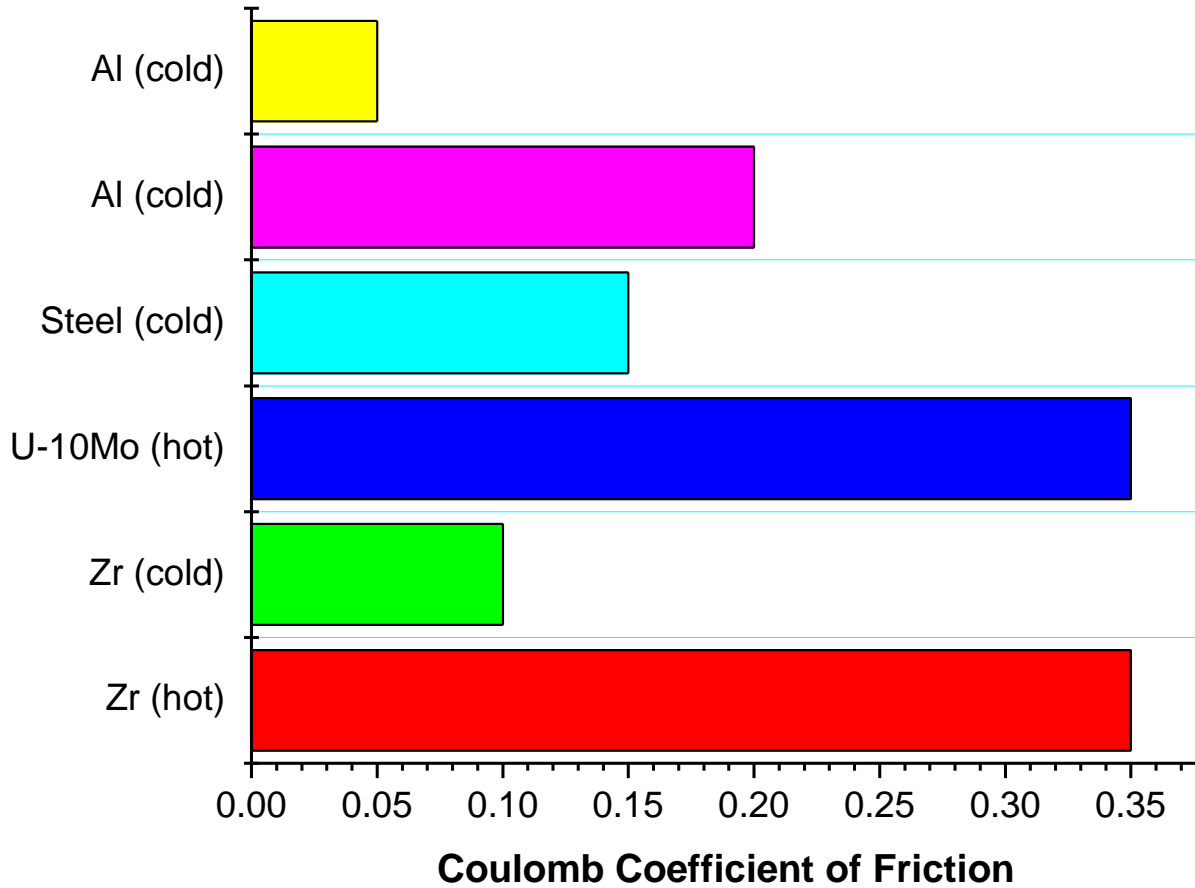


Figure 8 – Results of the literature study pertaining to relevant values for the Coulomb coefficient of friction between the rollers and the strip material in the deformation process [21 – 25].

EnSight was employed to perform post-processing of the data output by ABAQUS [19]. This software permits extraction of the forces, displacements, velocities, etc. and gradients thereof for user specified material points. In this application, the path, or trace, of these material points was determined as the foil passed through the rolling process, as visualized in Figure 9. The resulting material trace was directly calculated in EnSight based upon the velocity vector of the strip material at each time-step. Of particular interest, EnSight was used to extract the deformation gradient, $\mathbf{F}(t)$, as a function of time for the material point trace. A MATLAB script was then used to calculate the velocity gradient, $\mathbf{L}(t) = \dot{\mathbf{F}} \mathbf{F}^{-1}$, as a function of time based upon the deformation gradient results from EnSight. This velocity gradient history was used as the direct input to the VPSC code. MATLAB was also used to determine the condition

number of the velocity gradient [20]. While the velocity gradient's condition number was too high for the tensor to be considered well-conditioned, it was low enough that the data was still practically useable.

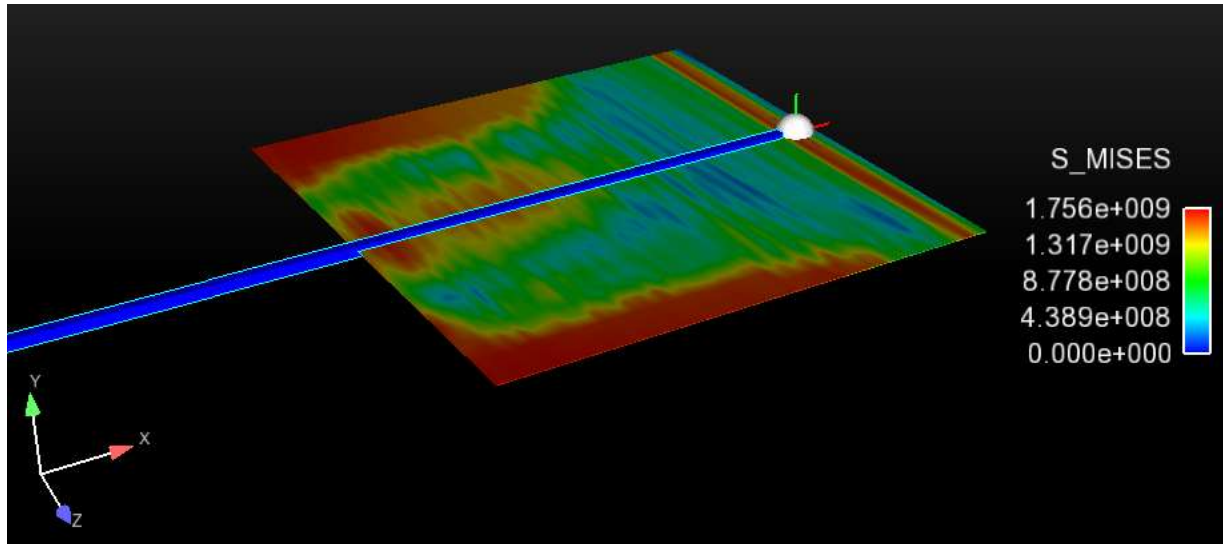


Figure 9 - Tracking of a material point in the EnSight software, visualized as a dark blue stream. From this removed visual perspective, it is impossible to show the small nuances of the material point's travel, but it is possible to determine the overall trajectory of the particle. The rigid rollers have been removed for an improved image.

The simulations were performed using 4-node bilinear plane strain quadrilateral, reduced integration, hourglass control elements for an explicit procedure. As in the 3D case, a mesh refinement study was performed to determine appropriate element sizes for the simulation. Again, a symmetry boundary condition was halfway through the thickness of the foil. Constant velocity was employed for the initial movement of the block material, as well as for the boundary condition dictating the rotation of the roller. The velocity values themselves were equivalent to the values used for the three-dimensional model, whose values were selected to be similar to cold rolling cases in literature [18].

In order to reduce the computational cost of the simulation, the roller was designed differently for the two-dimensional case. It was still modeled as a discretely rigid surface, however, the roller was partitioned into two sections, the first was the approximate area that could contact the strip material, for

which a fine meshing strategy was employed. The other roller partition, the area that would not contact the strip material, was assigned a coarse meshing strategy. This roller design enables adaptability of the model within ABAQUS to accommodate changes to the strip material's geometry, position, and initial velocity, but still yields a low computational cost. Similarly, the particular length of the simulated workpiece was minimized in order to make the solution as computationally efficient as possible. As can be seen in Figure 10 and Figure 11, edge effects seemingly stop manifesting after 0.2 mm.

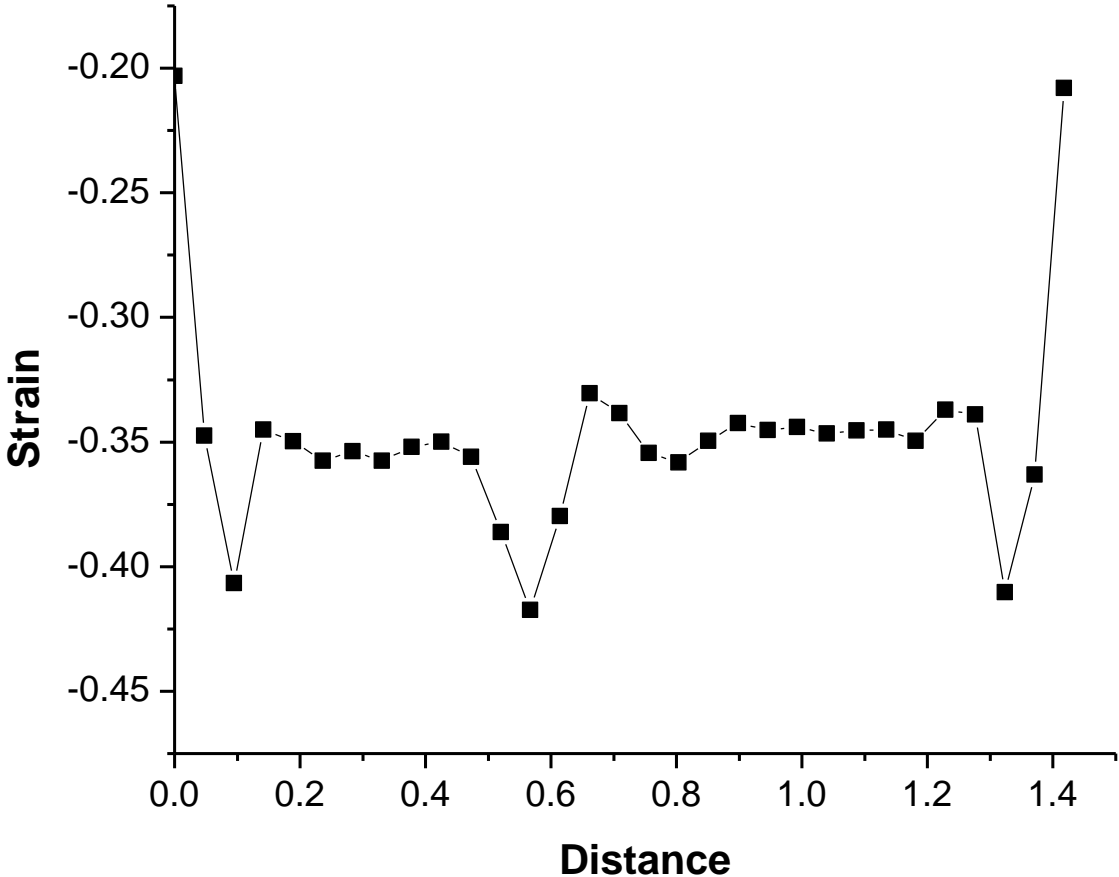


Figure 10 - The strain in the normal direction for the fully deformed strip material along the entirety of its simulated length.

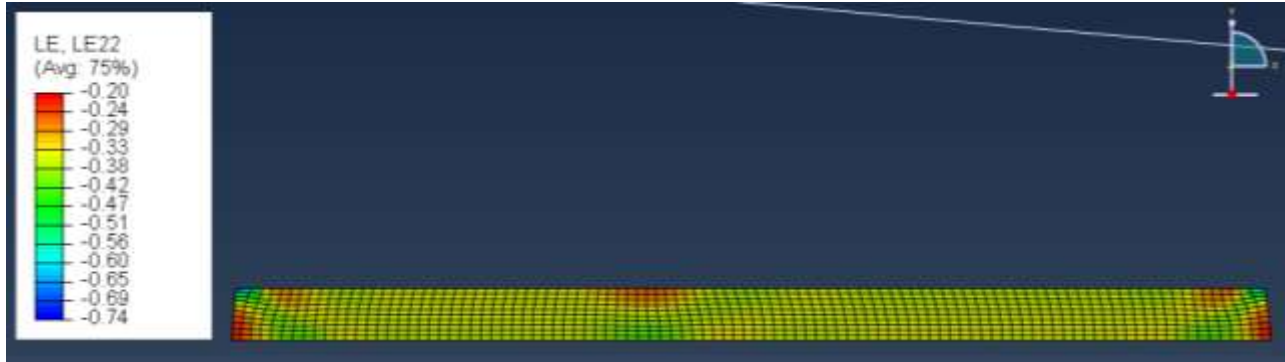


Figure 11 - The strain in the normal direction for the fully deformed strip material as viewed in the ABAQUS output viewer.

As in the three-dimensional model, contact properties between the roller and the strip material were defined in the ABAQUS simulation to have both normal and tangential behavior. The selected normal behavior options minimized penetration of the strip material into the roller, and allowed the two surfaces to separate after contact (i.e. the strip exits the roll gap). The tangential behavior of this contact was assigned a penalty formulation that used a Coulomb friction model. The value for the coefficient of friction can be calculated and updated based upon rolling conditions, but in this case a single value of $\mu = 0.15$ was selected and held constant to match the selection of the three-dimensional case.

EnSight was employed to perform post-processing of the FEM simulation data output in the same manner as in the 3D case. Table 2 details the models used for the mesh refinement study of the two-dimensional model. The fractional increase in the element count amongst the least refined meshes is low, as at that point, element count from the roller dominates the model. Figure 12 shows the equivalent strain experienced by the elements (averaged along the length) midway through the thickness of the workpiece, which was used to determine if the results of the simulation had converged. Figure 13 shows the increasing CPU cost as the element count is increased via mesh refinement.

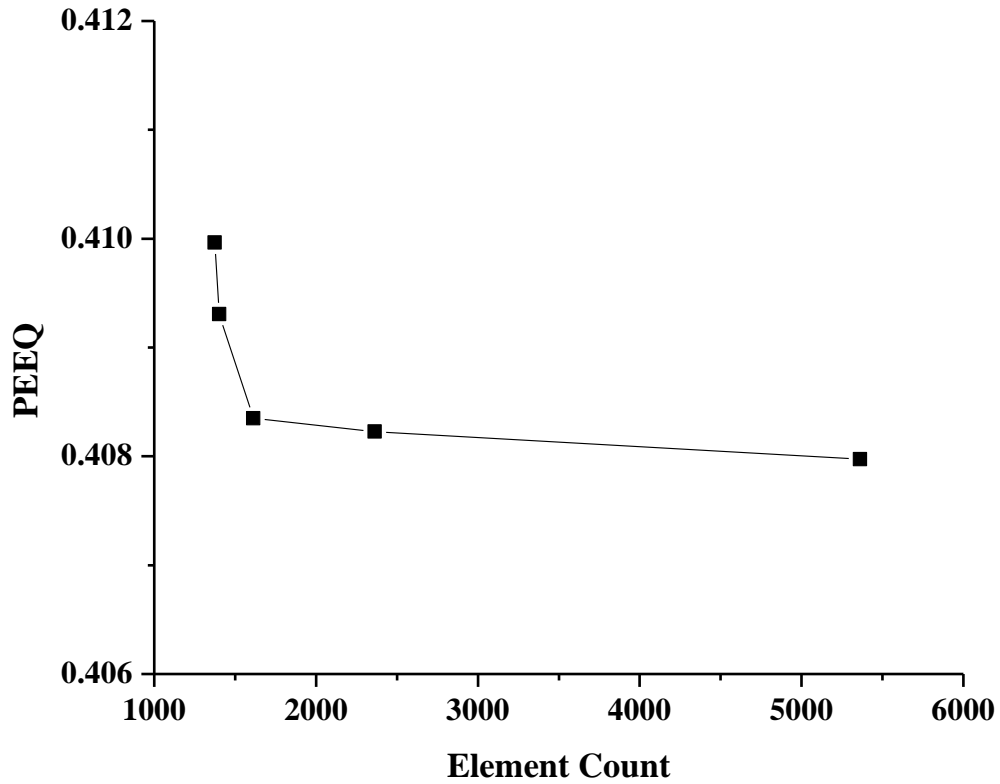


Figure 12 - The equivalent strain experienced by the elements midway through the workpiece, plotted against time.

Table 2 - Shows the number of elements employed and the computational cost of each degree of mesh refinement.

<i>Number of Elements</i>	<i>CPU Time (seconds)</i>	<i>Refinement Description</i>
1373	9	Lowest
1403	19.1	Lower
1613	61.3	Middle
2363	240.1	Higher
5363	1366.8	Highest

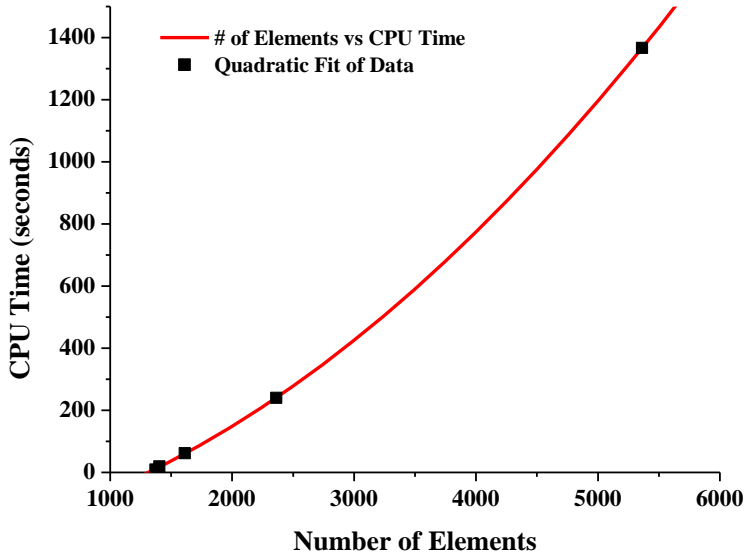


Figure 13 - The CPU time necessary to simulate the corresponding element count, showing the results of the mesh refinement study performed on the two-dimensional cold rolling model. The quadratic fit has an r-squared value of 0.9999.

The “higher” degree of mesh refinement was selected as the best result to continue work, as it divides the thickness of the workpiece to the same degree as the three-dimensional model. Further, even the “higher” degree (see Table 2) of mesh refinement does not constitute a significant investment of computational time.

CPU time required to run a simulation which employs explicit time integration with any particular mesh will be directly proportional to the time period of the event [21]. Numerical stability consideration restrict the time increment to:

$$(1) \Delta t \leq L^{el} \sqrt{\frac{\rho}{\lambda + 2\mu}}$$

In equation (1), Δt is the time increment, L^{el} is the characteristic length associated with elements in the mesh, ρ is the density of the simulated material, and λ and μ are the Lamé's constants for the material.

While the time increment for global stability may be larger, most discussions of the computational cost of an explicit procedure can assume that the inequality in (1) holds true. Further, the computational cost of a simulation which employs explicit time integration with any particular mesh will be directly proportional to the size of the mesh [21]. The result of these dependencies is:

$$(2) n \propto (\Delta t^{-1}) (N)$$

In equation (2), n is the number of computational steps taken to achieve the result. Δt is the time increment for the explicit procedure, as detailed in equation (1). N is the number of elements used in the mesh. By taking the results of equation (1) and the fact that N has a square dependence on L^{el} , equation (2) can be reduced to:

$$(3) n \propto N^2$$

As an example, if in a two-dimensional problem the characteristic element length is halved, the computational cost will increase by a factor of four. This is because there will be double the amount of elements, and twice as many time increments will be required to solve the problem.

In a like fashion, a mesh refinement study was performed on the three-dimensional FE rolling simulation. At the lowest level of refinement, the 3D simulated workpiece completely elastically recovered from the imposed deformation. As the mesh was refined, the results approached expected behavior and converged. Applying equations (1) and (2) to the 3D case indicates an expected cubic dependence for the CPU time on the number of elements employed in the simulation. The observed behavior does not match a cubic dependence, which could be the result of a low number of refinements.

3.1.3 Extrusion

This section adapted from, “Development of Thin-walled Magnesium Alloy Extrusions for Improved Crash Performance Based Upon Texture Control,” by Bruce W. Williams, Sean R. Agnew, Robert W. Klein, and Jonathan McKinley [6]. The author would specifically like to thank Bruce Williams for his contributions in developing the FE model for the extrusion.

The extrusion process was investigated using a two-dimensional finite element model that assumed radial symmetry. Like for the rolling investigation, the extrusion model employed phenomenological continuum mechanics-based finite elements in ABAQUS. The material was assigned a flow stress of 100 MPa and exhibits a perfectly-plastic behavior (i.e., no strain hardening). This approximates the flow stress of AZ31B at 300 °C at a strain-rate of 0.1 s⁻¹ [22].

Contact properties between the stationary surfaces and the flowing material were defined in the ABAQUS simulation to have both normal and tangential behavior. The selected normal behavior options minimized penetration of the flowing material into the stationary surfaces, and allowed the two surfaces to separate after contact (i.e. as the flow material exits the constrained area). The tangential behavior of this contact was given a penalty formulation, which employed a Coulomb friction model. The value for the coefficient of friction was selected as $\mu = 0.0$ to remove the prediction of any deadzones within the simulation.

Eight extrusion profiles were modeled using this arrangement. All of the extrusion profiles employed are two-dimensional axisymmetric elements, except Profile #2, which employed plane strain elements.

Table 3 – Description of the eight extrusion simulation profiles created in ABAQUS.

Table 3 - Description of extrusion simulation profiles	Description	Extrusion Velocity (mm/min)
#1	Axisymmetric bar extrusion – diameter 88.9 mm to 38.1 mm	508
#2	Plane strain strip extrusion – 88.9 mm thick to 38.1 mm thick	508
#3	Diameter 38.1 mm bar extruded to tube with 57.2 mm outer diameter and 2.5 mm thickness – gap thickness = 3 mm	254
#4	Diameter 38.1 mm bar extruded to tube with 57.2 mm outer diameter and 2.5 mm thickness – gap thickness = 10 mm	254
#5	Diameter 38.1 mm bar extruded to tube with 57.2 mm outer diameter and 2.5 mm thickness – transition zone ~ 20 mm	254
#6	Tube with 57.2 mm outer diameter and 15 mm thickness extruded to tube with 57.2 mm outer diameter and 2.5 mm thickness	508
#7	Tube with 88.9 mm outer diameter and 19 mm thickness extruded to tube with 88.9 mm outer diameters and 2.5 mm thickness	254
#8	Tube with 88.9 mm outer diameter and 19 mm thickness extruded to tube with 55.8 mm outer diameter and 2.5 mm thickness	254

An Arbitrary Lagrangian-Eulerian (ALE) adaptive meshing technique was specified due to the large distortions enforced by the extrusion die. The ALE method combines features of both a Lagrangian analysis (the mesh and material move together) and an Eulerian analysis (material moves independently of the mesh). In this joint technique, the mesh and material initially move together, but adaptive remeshing at regular intervals prevents the elements from becoming too distorted. Hence material point tracking capability of the EnSight post-processing software was used to determine the state of strain for a specified material point. First, EnSight was used to extract the deformation gradient, $\mathbf{F}(t)$, as a function of time for the material point trace. The same MATLAB script employed in the analysis of the rolling simulations was then used to calculate the velocity gradient as function of time, $\mathbf{L}(t) = \dot{\mathbf{F}} \mathbf{F}^{-1}$. The VPSC code employed this velocity gradient history as its direct input.

3.1.4 Hydroforming of Irradiation Assembly

This section of the thesis describes a reproduction of results first developed by Govindarajan et al. in, “Assembly and Irradiation Modeling of Residual Stresses in Low-Enriched Uranium Foil-Based Annular Targets for Molybdenum-99 Production.” [4].

The goal of this work was to recreate an ABAQUS finite element model developed by Govindarajan et al., which simulates the assembly and irradiation of a LEU foil-based target for molybdenum-99 production [4]. The purpose of recreating this model was to develop an awareness of desirable foil properties to improve production of these targets.

In particular, the paper describes interest in the residual stress state of the final product. If tensile stresses remain in the outer tube, it will spring open when cut along the longitudinal relief for retrieval of the foil [4]. If compressive residual stresses remain in the tube, they will cause the outer tube to collapse, which will increase the time and effort required to retrieve the target foil [4]. The other important goal of the residual stress is to maintain intimate mechanical contact between the U foil and the Al annuli, which surround it, since good contact is required to have good thermal transfer between the U, which becomes hot during irradiation, and the Al, which is in contact with cooling water.

The model was created with three two-dimensional parts, as seen in Figure 14:

- Inner Aluminum Tube
- Uranium Foil
- Outer Aluminum Tube

Material properties for both the aluminum and uranium were taken directly from the original paper for the initial run of this model. The uranium properties were then modulated to observe the impact that different uranium processing routes might have on the predicted residual stress state.

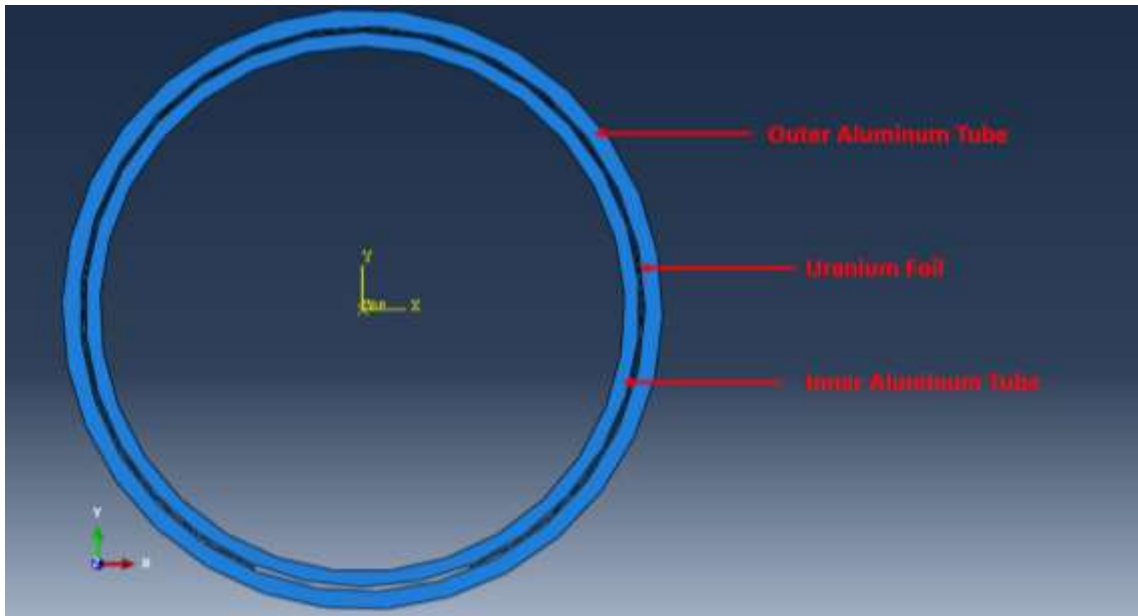


Figure 14 - ABAQUS schematic drawing of the irradiation target assembly model. The foil is contained between two aluminum tubes, each noted in the figure.

The first step of the model simulated the fabrication of an aluminum-clad foil via hydroforming. An internal pressure was applied, which plastically deformed the inner tube and foil into an assembly with the outer tube. Surface-to-surface properties were defined to have normal contact properties with a stipulation that surfaces were not allowed to separate post-release.

The second step release the pressure, and propagated the surface-to-surface properties defined in the previous step. In many ways, this process is similar to the process of autofrettage, during which pressure vessels (notably gun barrels) are internally pressurized beyond the level anticipated in service because it imparts a residual stress profile that protects them from fatiguing during the cyclic applications of pressure experienced in service. Distinctly, as mentioned previously, the goal here is not to impart higher fatigue life, but to improve thermal performance of the target and ease subsequent disassembly.

The third step simulated irradiation of the target component. This step modified the original surface-to-surface properties, and allowed them to separate post-release. Further, the surface-to-surface properties

were updated in this step to include conductance values. It was assumed that an infinite conductance existed at zero separation, and that the conductance goes to zero at a separation of 10 mm. In reality, interfaces are often observed to have a finite thermal “resistance” which is distinct from the materials on either side of the interface. However, Govindarajan et al. used this conductance assumption as well, and include in their paper that ABAQUS interpolates to find conductance values for separation values between zero and the 10 mm. The LEU foil was given a heat body flux of $1.6 \times 10^7 \text{ W/m}^2$, as described in the original paper. Surface film conditions were assigned to the outer surface of the outer aluminum tube and to the inner surface of the inner aluminum tube. The surface film conditions were both assigned a coefficient of 19000 W/m^2 and a sink temperature of 323 K. These film conditions, defined by the original paper, properly simulate the water coolant which flows along the surfaces.

3.2 Crystal Plasticity Simulations and Property Prediction

3.2.1 Uranium – Rolling

This section partially adapted from, “Texture Measurement and Property Prediction of Rolled α -uranium,” by Robert W. Klein, John R. Einhorn, Matthew Steiner, Christopher Calhoun, Elena Garlea, and Sean R. Agnew [1].

By utilizing the functional forms of single crystal thermo-elastic properties described in Calhoun et al., the thermo-elastic properties of the polycrystalline material were approximated using a self-consistent scheme [23] [24]. This approach permitted exploration of the effect of crystallographic texture on the thermo-elastic properties. Subsequent researchers may like to explore optimization of the texture to produce a desired set of properties. The plastic properties were explored in a similar manner.

Knezevic et al. recently published a methodology for the VPSC-based modeling of the plasticity and deformation texture evolution of uranium [17] . Because the grain size determined via optical microscopy ($10.3 \mu\text{m}$ - as addressed in section 4.1.2) is similar to the annealed uranium samples modeled by Knezevic et al. ($15 \mu\text{m}$) [17], it was deemed that their polycrystal plasticity model would be appropriate for

predicting texture evolution and stress-strain response of the foil, described in detail in Appendix C. The complete details of the viscoplastic self-consistent (VPSC) code used to complete the simulation process in this thesis were published by Tomé Lebensohn [25].

3.2.2 Magnesium – Extrusion

This section adapted from, “Development of Thin-walled Magnesium Alloy Extrusions for Improved Crash Performance Based Upon Texture Control,” by Bruce W. Williams, Sean R. Agnew, Robert W. Klein, and Jonathan McKinley [6]. The author would specifically like to thank Bruce Williams and Jonathan McKinley for their contributions in developing a FE model for the extrusion.

Crystal plasticity simulations were performed using the VPSC7c version of the code using a similar method to that detailed by Beyerlein et al. [26], where a strain-history file is composed from the output of ABAQUS. Agnew et al. have previously demonstrated that VPSC can reasonably predict deformation textures in wrought magnesium alloys [27]. In addition to the velocity gradient history, the critical resolved shear stress (CRSS) ratio of basal:prismatic:<c+a> slip was an important input to the model. Initially simulations were performed with an initial ratio of 1:8:6, which was the set of slip system strength ratios that seemed to best reproduce the texture evolution of a typical magnesium alloy, AZ31, during ECAE [27]. If there were difficulties in producing predictions in the current work, then the ratio would be reduced to 1:6:6 or 1:4:4. Larger values of prismatic and <c+a> slip would be expected to lead to stronger texture. Lowering the CRSS ratio could weaken the texture and is similar to an alloying or temperature effect by permitting more non-basal slip which can slow the plastic rotation below the level when basal slip dominates the strain accommodation. An initially random texture was used to represent pre-extruded state of the material.

Chapter IV

4 Results and Discussion

4.1 Cold Rolling of Uranium

4.1.1 FE Model Results

This section adapted from, "Texture Measurement and Property Prediction of Rolled α -uranium," by Robert W. Klein, John R. Einhorn, Matthew Steiner, Christopher Calhoun, Elena Garlea, and Sean R. Agnew [1].

Plots of the velocity gradient, $\mathbf{L}(t)$, from the FE simulation of rolling (Figure 15 – midway through the workpiece, Figure 16 – at the surface of the workpiece) in the ND, L_{22} , show that the material experiences an increasing rate of compressive deformation along the ND as it enters the roll gap and then the rate slows and even reverses for a moment during the elastic unload as it exits the roll gap. The same plot for the L_{12} component of the velocity gradient (Figure 15 – midway through the workpiece, Figure 16 – at the surface of the workpiece) shows that the material experiences a simultaneous shear as it is being compressed due to the friction between the rolls and the workpiece. A shear-reverse shear situation manifests itself due to the fact that the sheet is moving slower than the rolls as it enters and faster than the rolls as it exits. Only at the so-called "neutral point" or peak in the friction hill are the two moving at the same velocity [28]. Note that while the magnitudes of $\mathbf{L}(t)$ match for Figure 15 and Figure 16, different longitudinal positions on the foil create a mismatch in timesteps. Analysis of $\mathbf{L}(t)$ in MATLAB concludes that the velocity gradient is not well-conditioned, meaning that for small changes in its entries, it could become non-invertible. It is worth noting that $\mathbf{L}(t)$ is still practically useable, as its condition number is generally only a single order of magnitude greater than unity.

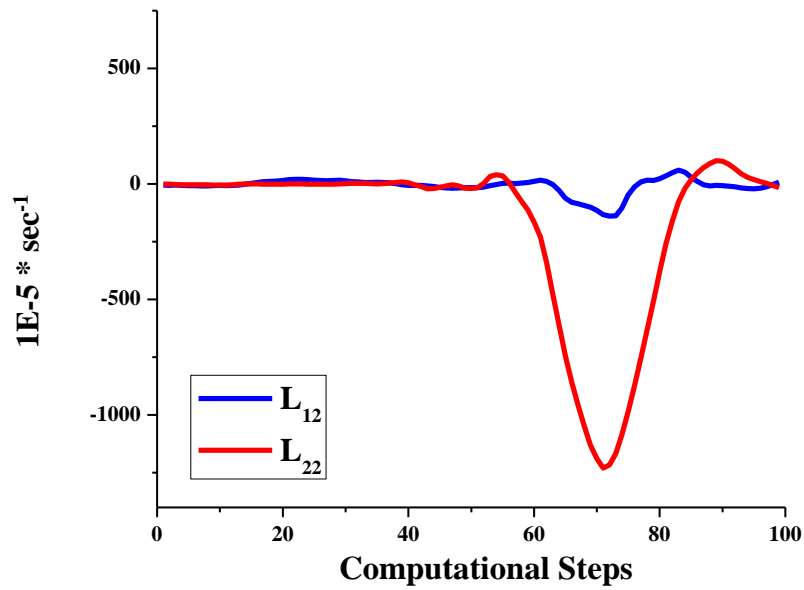


Figure 15 – Plots of the velocity gradient history for the L_{12} and L_{22} components for a material point trace at the midplane of the workpiece.

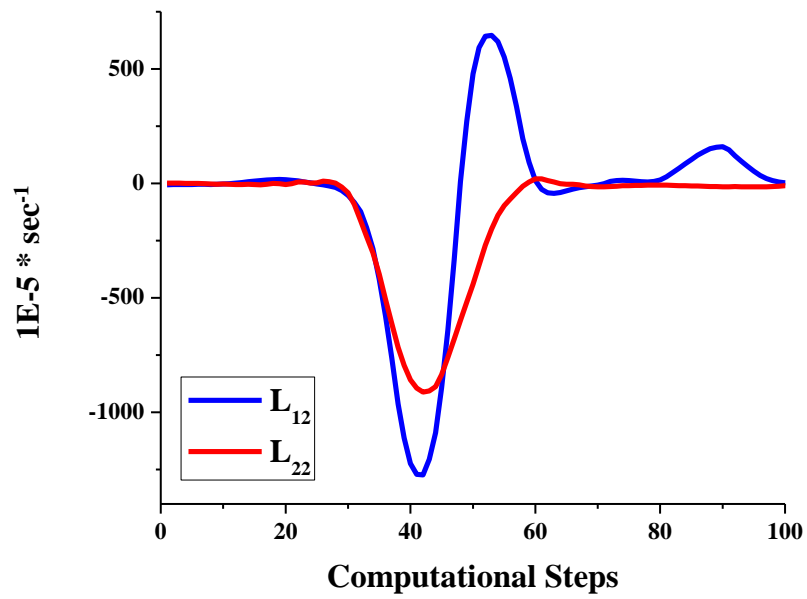


Figure 16 – Plots of the velocity gradient history for the L_{12} and L_{22} components for a material point trace at the surface of the workpiece.

4.1.2 Microstructure Results

This section partially adapted from, "Texture Measurement and Property Prediction of Rolled α -uranium," by Robert W. Klein, John R. Einhorn, Matthew Steiner, Christopher Calhoun, Elena Garlea, and Sean R. Agnew [1].

Grains of the microstructure in the optical micrographs of the polished samples, collected under polarized light, appear equiaxed along all three directions, viewable in Figure 17. The black regions in the polarized light micrographs are taken to be carbide particles and/or pits where carbide particles were removed from the surface during polishing. The linear intercept for grain size analysis was employed to determine that the grains in the microstructure have an average diameter of 10.3 μm as shown in Figure 18 [29].

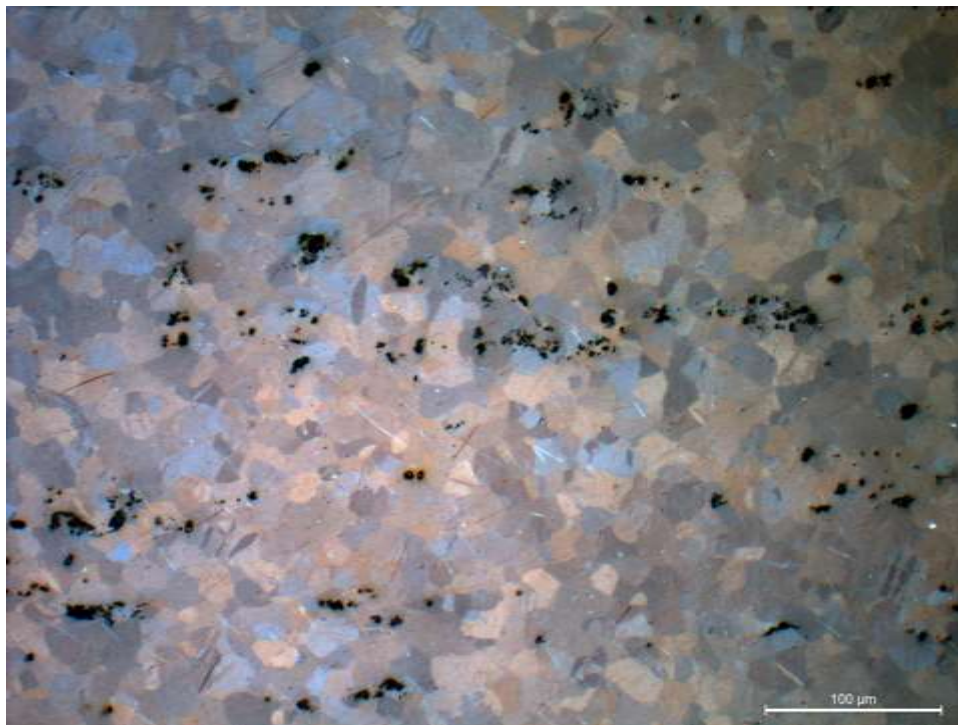


Figure 17 – Polarized light optical micrograph, viewing the foil along the ND, with RD oriented along the horizontal axis, showing few twins in the equiaxed grains, impurity banding along RD and weaker banding along TD (vertical).

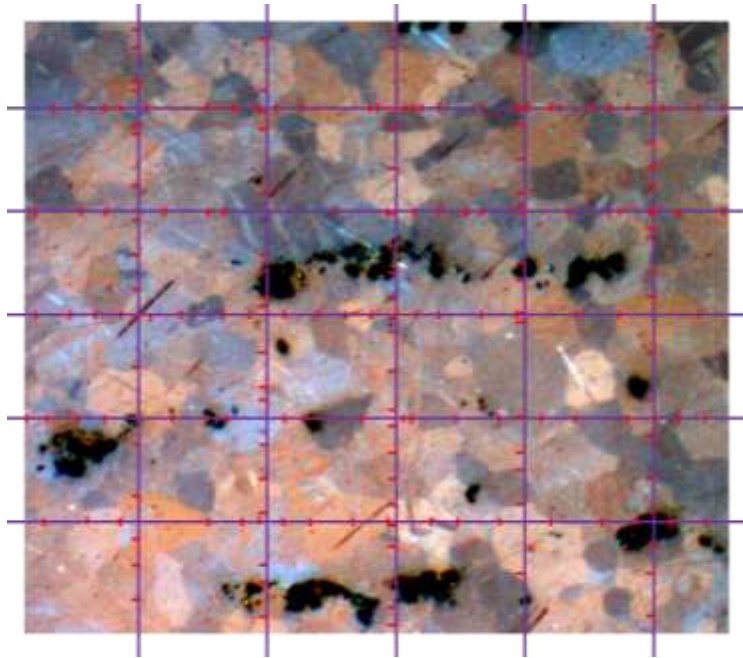


Figure 18 – Linear intercept calculation on the ND surface of the sample, yielding a 10.3 μm average diameter. Magnified section of a polarized light micrograph. Twin boundaries were not counted.

The texture measured via XRD on the α -uranium foils is presented in Figure 19 as recalculated pole figures generated from an averaged of the ODFs obtained from all three foil samples. This texture features the (020) poles oriented in all direction perpendicular to the ND, with a strong tendency to align with the RD. Further, the (002) peaks point out towards the ND, but with two symmetrically equivalent peaks tilted towards the TD. Pole figure plots of the ODFs from each individual foil sample are available in Appendix A. The maximum intensity of these pole figures is about 5 multiples of random (MRD).

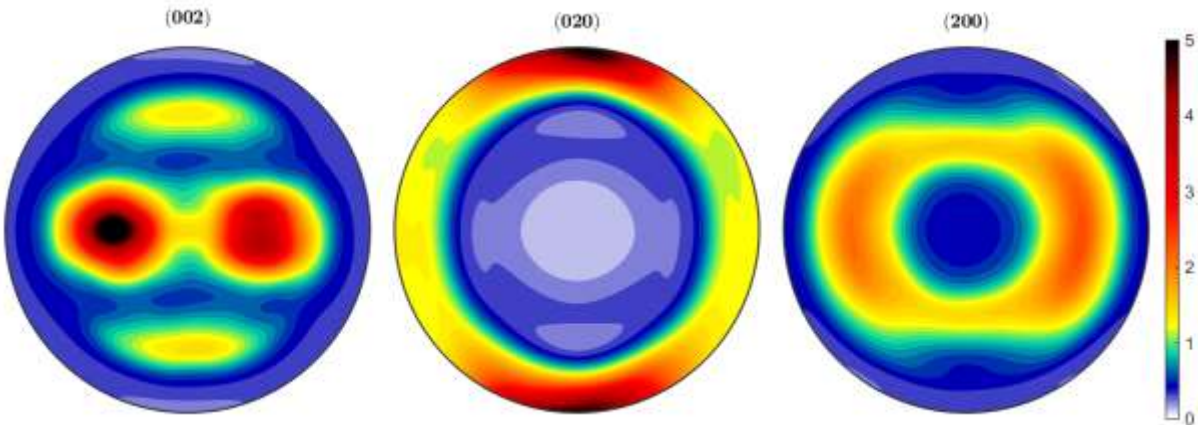


Figure 19 – Experimental texture, recalculated pole figure from complete ODF averaged across three foil samples. RD points upward, TD points right, and ND points out of the page. Intensity values are given as multiples of random (MRD), which is consistently used as the convention throughout the thesis.

Knezevic et al. recently published a rather complete treatment of the modeling of deformation of uranium utilizing VPSC, including incorporation of a state-of-the-art dislocation density-based strain hardening model [17] [30]. The crystal deformation mode properties present in Zecevic et al. are employed in the VPSC code presented in this thesis [31]. Figure 20 shows the results generated by VPSC which employ the strain history determined by FE modeling as input from a material point midway through the thickness of the workpiece to this particular model. Like the experimental texture, the (020) poles tend to align towards the RD and while the (002) poles align with the ND. However, the (002) are tilted towards the RD, by about 25° , unlike the strong TD tilt observed in the experimental texture. The maximum intensity for this set of pole figures is 5.5 MRD. The results presented in Figure 20 look quite similar to the case predicted for a case of idealized plane-strain. By appending the velocity gradient input with a copy of itself, multiple rolling passes can be simulated in the VPSC code. Figure 21 shows the results of simulating two passes of rolling for a point at the midplane of the workpiece, while Figure 22 shows the results of simulating three passes of rolling for a point at the midplane of the workpiece. A qualitatively similar texture is shown to that of the single pass result, but the texture has acquired additional intensity. One possible explanation for the disparity between the (002) experimental and simulated results is that the XRD experimental texture only evaluates surface conditions, due to the limited penetration of the Cu-K_α

X-rays in U. This is where the material is strongly influenced by the shear-reverse shear induced by the foil-roller contact during processing. If the velocity gradient history of a material point at the surface of the thickness of the workpiece is modeled, the resulting texture (Figure 23), lacks symmetry in the tilting of the (002) from ND and instead points forward towards RD, instead of evenly splitting fore and aft as was the case for the midplane point. This can be traced back to the differences in the velocity gradient history of the two points (Figure 15 and Figure 16), but it does not explain difference between the experimental and observed textures. Two-pass and three-pass simulations were constructed for the surface point condition in the same manner as for the midplane condition, with the results in Figure 24 and Figure 25, respectively. Both of these textures are qualitatively similar to the one-pass simulation, but contain additional intensity.

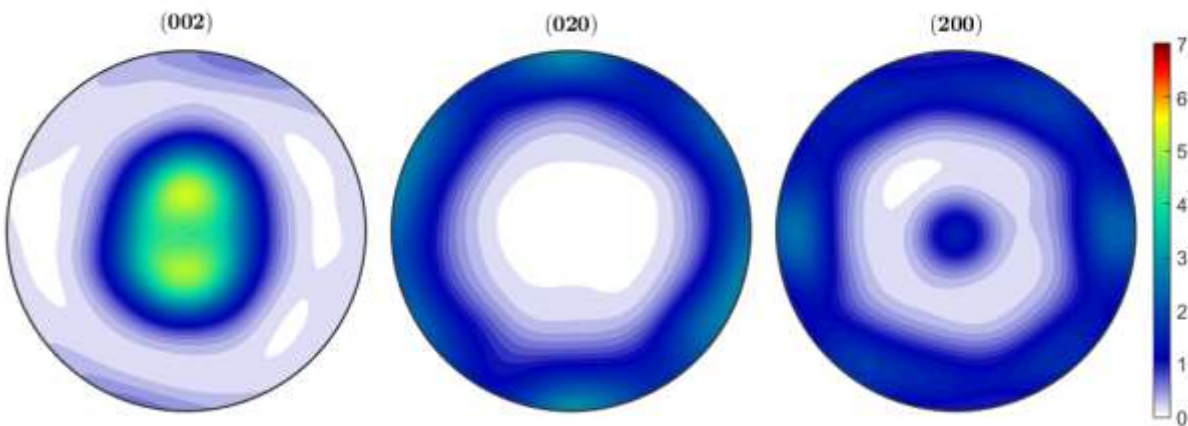


Figure 20 – FE-VPSC texture from midplane material point trace (1 pass). RD points upward, TD points right, and ND points out of the page.

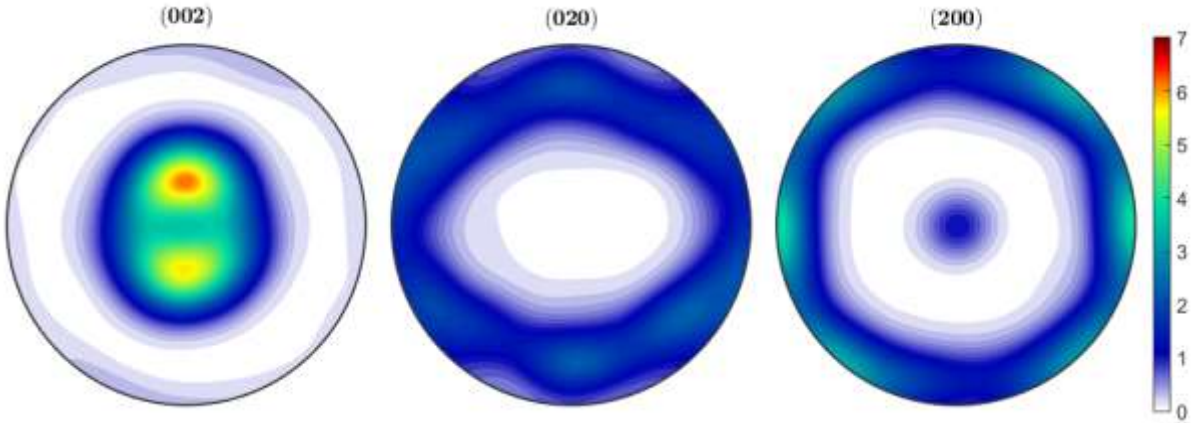


Figure 21 - FE-VPSC texture from midplane material point trace (2 passes). RD points upward, TD points right, and ND points out of the page.

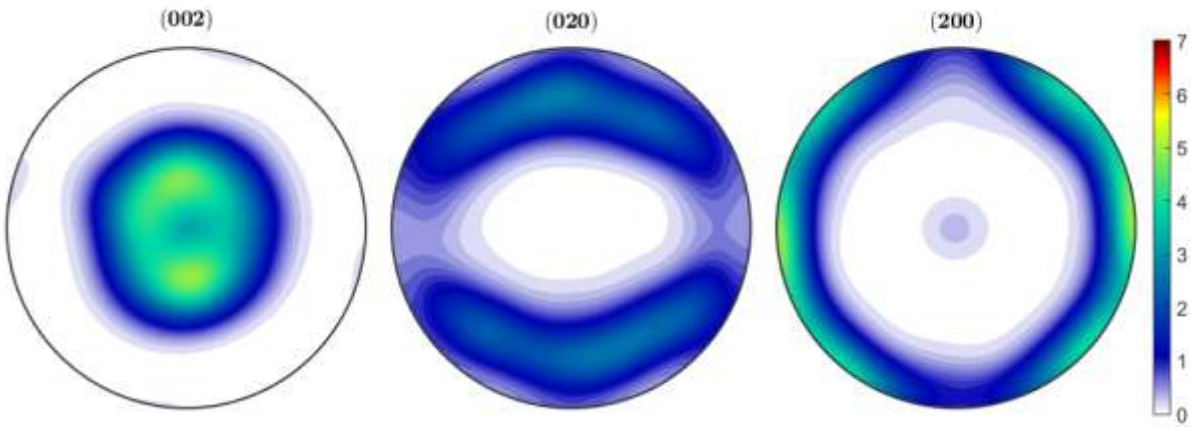


Figure 22 - FE-VPSC texture from midplane material point trace (3 passes). RD points upward, TD points right, and ND points out of the page.

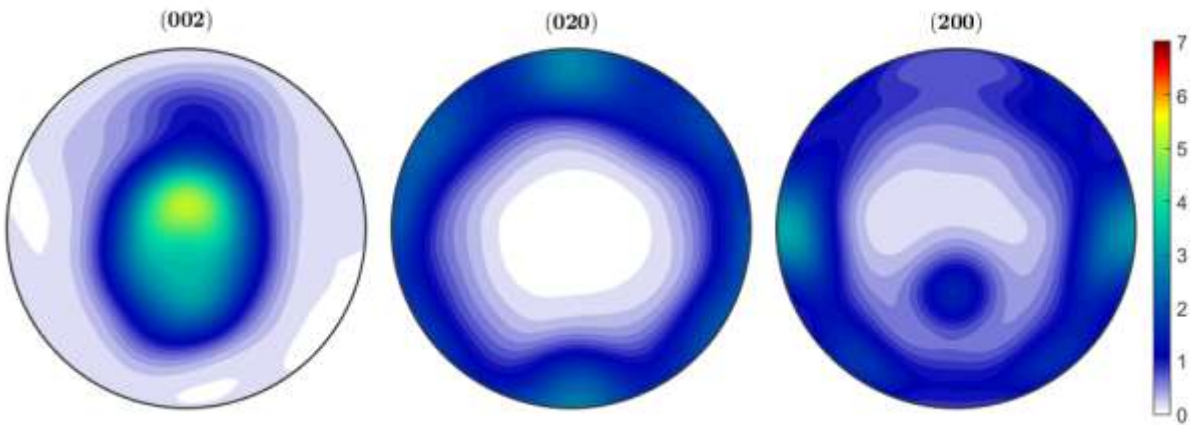


Figure 23 - FE-VPSC texture from surface material point trace. RD points upward, TD points right, and ND points out of the page.

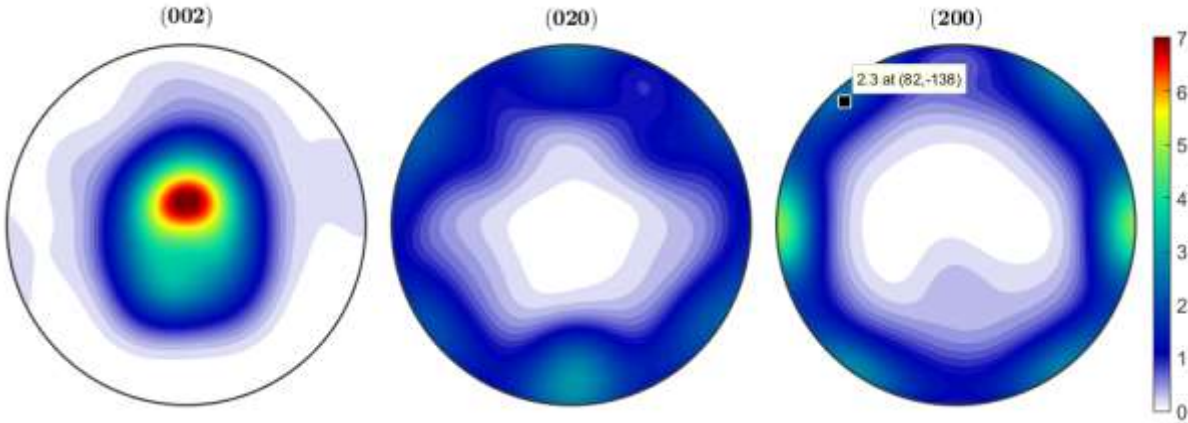


Figure 24 - FE-VPSC texture from surface material point trace (2 passes). RD points upward, TD points right, and ND points out of the page.

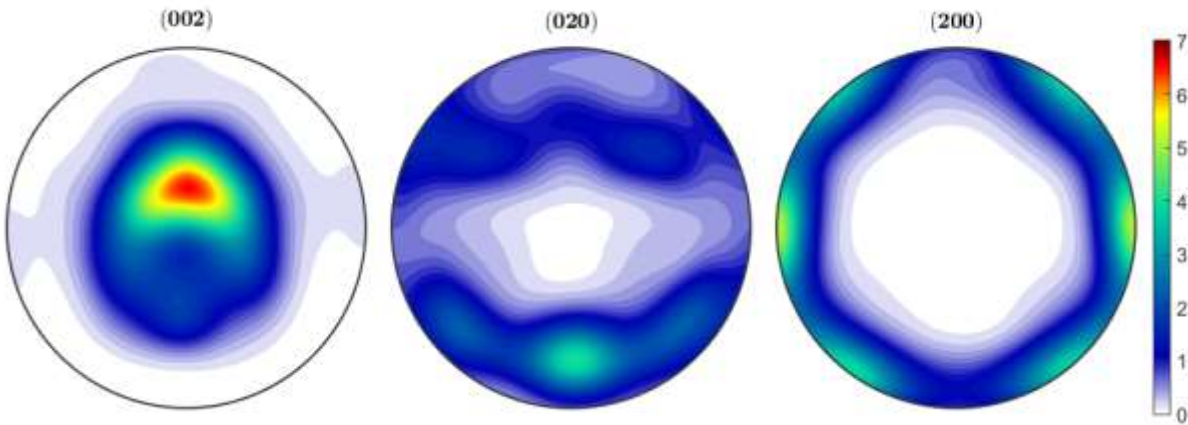


Figure 25 - FE-VPSC texture from surface material point trace (2 passes). RD points upward, TD points right, and ND points out of the page.

Textures measured by Knezevic et al. for a variety of rolled α -U plate (e.g., straight and clock rolled) with intermediate annealing steps also contain the feature of aligning the (002) poles with the ND with a tilt towards TD. Lloyd et al. explore the effects of annealing on cold-rolled uranium sheet [32]. Prior to annealing, they determine that rolled uranium has a texture such that the (002) poles are aligned with ND, but tilted towards RD, matching the results predicted by the FE-VPSC simulation, visualized in Figure 20. Upon recrystallization, the texture begins to develop the feature of having the (002) poles pointing towards ND but with a tilt towards TD, as illustrated in Figure 26. This shows that the present approach (modeling deformation texture alone) will not succeed in capturing the observed texture features. Rather,

a method for incorporating the effect of recrystallization must be developed. A fellow group-member, Dr. Matthew Steiner, is presently drafting a paper for submission to *Acta Materialia* on that very topic at the time this thesis is being prepared. In future work, a combined deformation plus recrystallization strategy should be attempted.

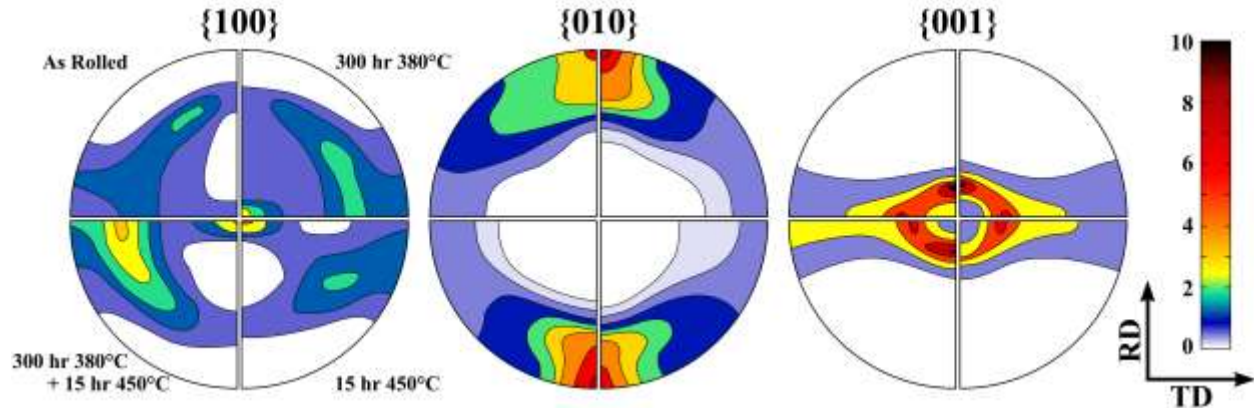


Figure 26 – Recontoured pole figure plots of the recrystallized texture of a rolled uranium sample from Lloyd et al. [32]. The recontouring was performed by Dr. Steiner. The RaD points upward, the TD points to the right, and ND faces out of the page.

Zecevic et al. employ a multiscale modeling approach in which they predict the crystallographic texture of rolled uranium [31]. At the largest scale, their model uses FE analysis, with each integration point's constitutive response modeled via VPSC. This approach also includes the composite grain model (TW) to account for lattice reorientation due to deformation twinning, and governs the threshold stresses for the slip modes via stored dislocation density (DD). Their simulation makes a pole figure prediction for a 60% reduction in five passes with the FE portion of the model employing CPE4 plane strain elements of comparable size to the elements used for the research in this thesis. Zecevic et al. predict that the (002) poles will preferentially align towards the ND and then split $\sim 20^\circ$ towards the RD with a maximum intensity of 9 MRD with the symmetry of the split reduced as the evaluated material point moves toward the surface of the deformed uranium. They further predict that the (020) poles will preferentially align away from the ND. These results match those presented in this thesis, with any slight differences explainable by the different levels of strain investigated.

The thermo-elastic properties of single crystals (left) are available in the literature [33] and are presented alongside predictions of textured polycrystal (right) predictions are shown in Figure 27 - Figure 30. These predictions were performed by using the approach described by Calhoun et al. [24]. For all of these figures, the 1 direction is equivalent to RD, 2 to ND, and 3 to TD. In Figure 27, the unusual behavior of orthorhombic U manifests itself in the negative coefficient of thermal expansion (CTE) parallel to the [010] direction of the crystal. This helps rationalize the CTE behavior observed in the polycrystalline material, where the red curve shows that the CTE parallel to the RD is lowest, since there is a preponderance of grains with the (020) poles aligned with the RD (as shown in Figure 19). Given the orthorhombic symmetry of rolled sheet material, the three independent coefficients provided here are sufficient to describe the complete CTE behavior. If the texture of the polycrystalline material were random, only a single coefficient would be required (i.e. the three polycrystal curves would overlap, and be approximately of the same magnitude of the 3 curve shown in black).

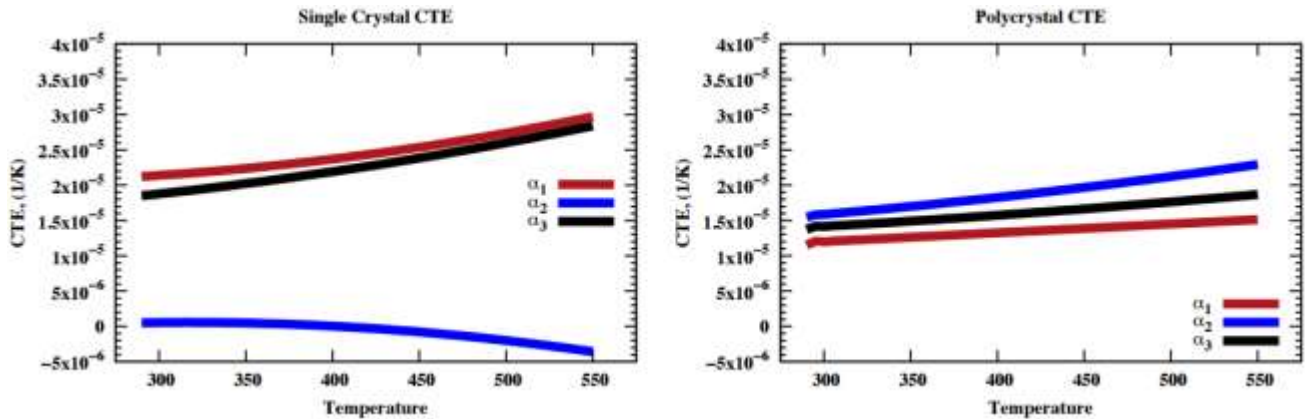


Figure 27 - The predicted coefficient of thermal expansion for single crystal (left) and polycrystal (right) α -uranium.

Figure 28 - Figure 30 show the single crystal elastic stiffness parameters on the left and the polycrystal parameters on the right. Because both the crystal and the sheet sample exhibit orthorhombic symmetry, only nine of the possible twenty-one independent coefficients in the stiffness tensor, \mathbf{C} , are required (three

of them are presented in each of the figures below). Figure 28 suggests that the polycrystalline foil material exhibits near in-plane elastic isotropy (note that C_{11} (RD) and C_{33} (TD) are essentially equivalent). The three shear moduli: C_{44} , C_{55} , C_{66} are essentially equivalent over the entire temperature range considered (Figure 29). The components related to the Poisson effect are presented in Figure 30.

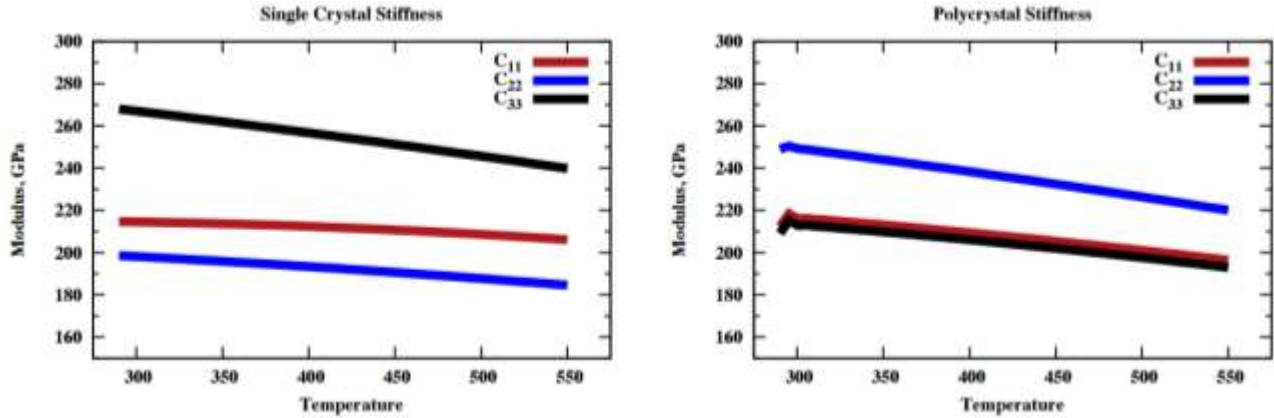


Figure 28 - The predicted stiffness tensor values (C_{11} , C_{22} , C_{33}) for single crystal (left) and polycrystal (right).

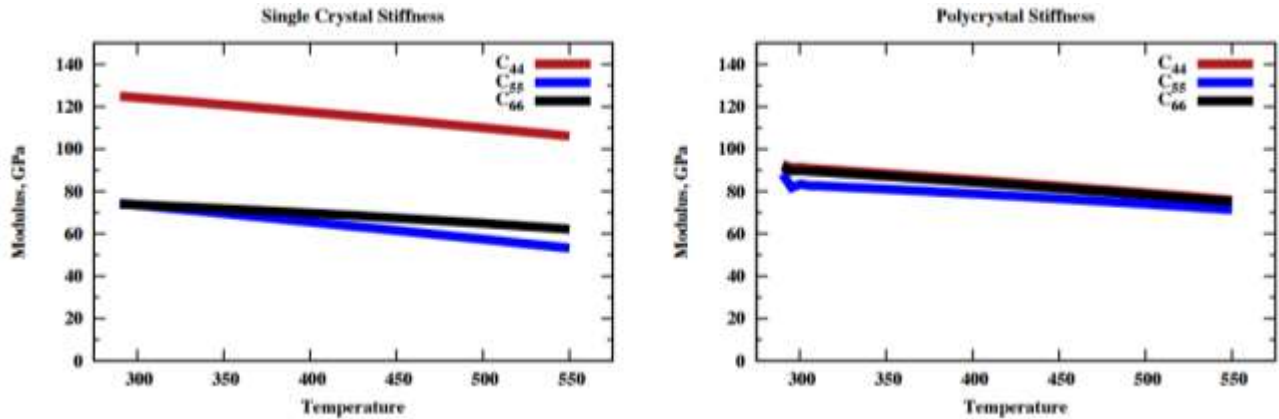


Figure 29 - The predicted stiffness tensor values (C_{44} , C_{55} , C_{66}) for single crystal (left) and polycrystal (right).

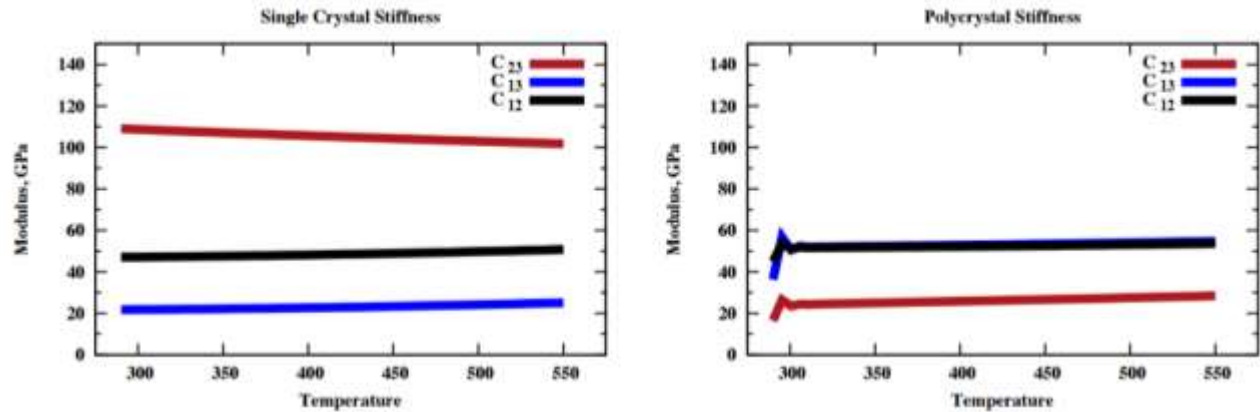


Figure 30 - The predicted stiffness tensor values (C_{23} , C_{13} , C_{12}) for single crystal (left) and polycrystal (right).

Beginning with a texture consisting of no preferred orientation (i.e. random texture), VPSC simulation was carried out to 20% strain for both compression and tension in directions parallel with the RD, TD, and ND. As expected, the results, presented in Figure 31, show that such a randomly textured material will exhibit isotropy as the compression curves for all three directions overlap each other, as do the tension curves. However, Figure 31 also shows that a randomly texture material yields at a slightly lower stress in tension than in compression. In short, the plastic response of this randomly textured material can be characterized as isotropic and weakly asymmetric. This asymmetry in the strength can be understood by referring to the slip and twinning mode activity plots for tension and compression (Figure 32). The activity plots for tension show that the twin systems, especially the $\{130\}$ twins, are dominant, while compression is forced to rely more heavily upon the harder wall system.

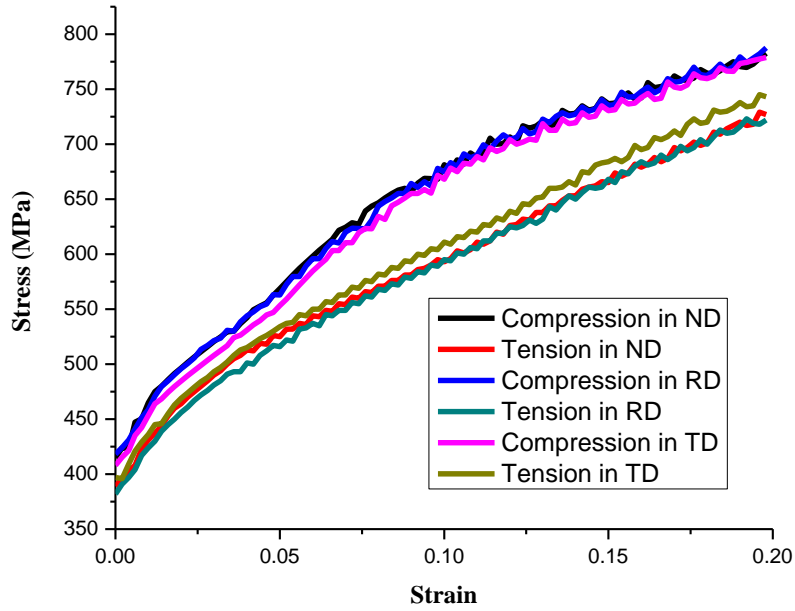


Figure 31 - VPSC based simulated curves of the stress-strain response of a random texture.

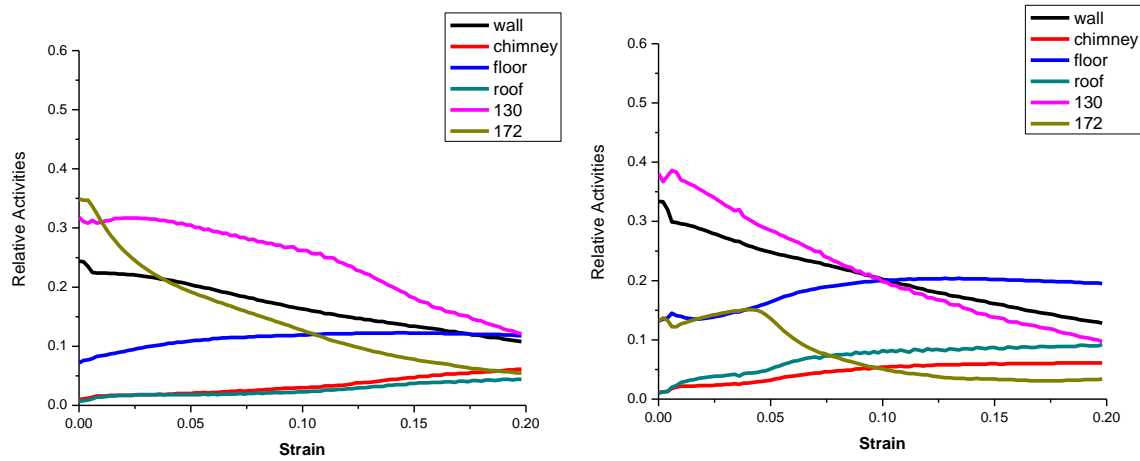


Figure 32 - Relative activities for slip and twin systems plotted against strain for the case of tension (left) and compression (right) parallel to the ND for the random texture.

For the experimentally measured foil texture, visualized earlier in Figure 19, the stress-strain curves, presented in Figure 33, indicate that the material is no longer isotropic. The material is most resistant to compression performed parallel to the ND (shown in the black curve of Figure 33). It seems to be initially softest when either put in tension along its ND or when compressed parallel to the RD. Note that tension parallel to ND is a rather hypothetical case, as the foil is only 170 μm thick. As observed for the

randomly textured material, this asymmetry is rooted in the polarity of twinning. The $\{130\}$ twinning mode is particularly well-oriented to operate during ND tension, but suppressed during ND compression (Figure 34), which forces a reliance on the floor slip system for compression along the ND. Floor slip has a higher critical resolved shear stress (CRSS) value than either of the twin systems [17]. The RD is not as symmetric as the ND, though compression along RD is quite soft. It is also interesting to note the relative symmetry of the tension and compression response along the TD. Consultation with activity plots reveals that a similar mix of deformation mechanisms is activated in tension and compression.

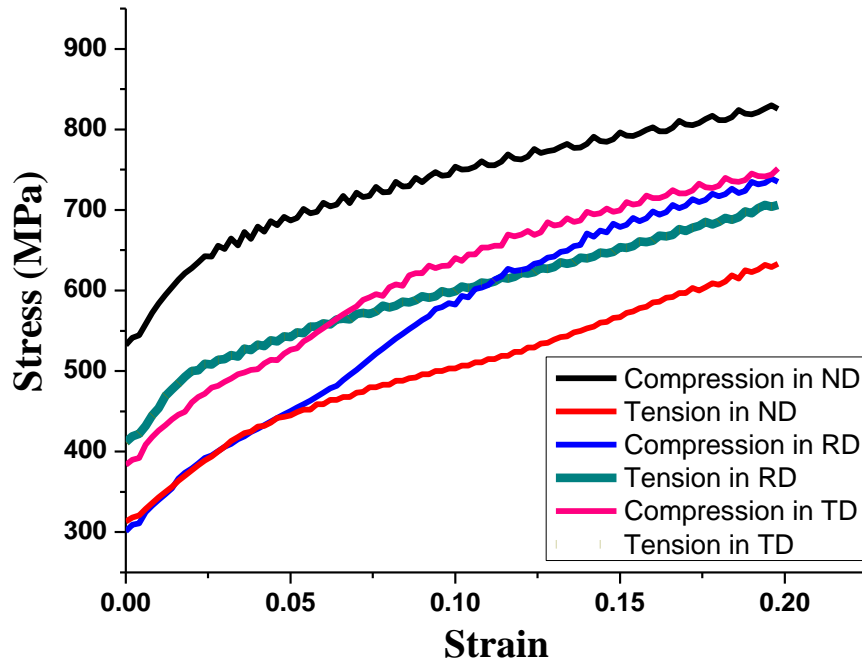


Figure 33 - VPSC based simulated curves of stress-strain response of the experimentally measured foil texture.

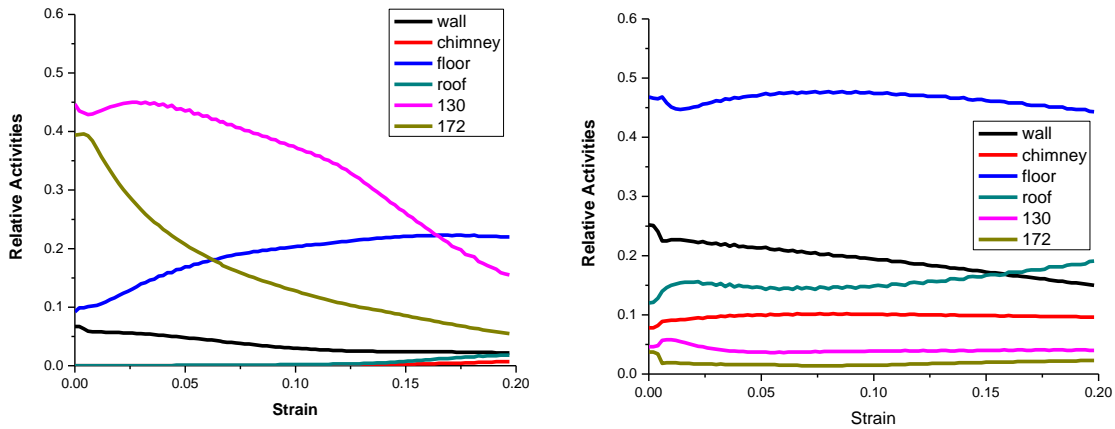


Figure 34 - Relative activities for slip and twin systems plotted against strain for the case of tension (left) and compression (right) parallel to the ND for the foil texture.

Using the VPSC code, one can calculate a two-dimensional projection of the polycrystal yield surface (PCYS). Stress levels within the yield surface are elastic and those on the yield surface give rise to plasticity (yielding) in a direction normal to the yield surface (i.e. associative flow). Presenting a π -plane projection of the yield surface is advantageous because anisotropy is readily visualized as a departure from radial symmetry about the origin. The π -plane is defined as the plane which cuts through principal stress space at all points with zero pressure, i.e. $\sigma_1 + \sigma_2 + \sigma_3 = 0$. The σ' axes in the yield surface plots (Figure 35) represent the projections of the principal axes (labeled based on their relationship to the sample axes) onto the π -plane. The positive σ' annotations are used to denote the positive (i.e. tensile) direction.

Figure 35 shows the π -plane projections of the predicted yield surfaces for uranium with random texture (blue) and the foil texture (green). The random texture almost has near-isotropic von Mises (black) behavior, which is characterized in the projection by a circle with a uniform radius. This is appropriate especially in the context of the earlier discussion which concluded the isotropy and weak asymmetry of randomly textured material. Contrasting with this is the foil yield surface, which shows a lot of resistance to ND compression, as expected from the stress-strain curves of Figure 33.

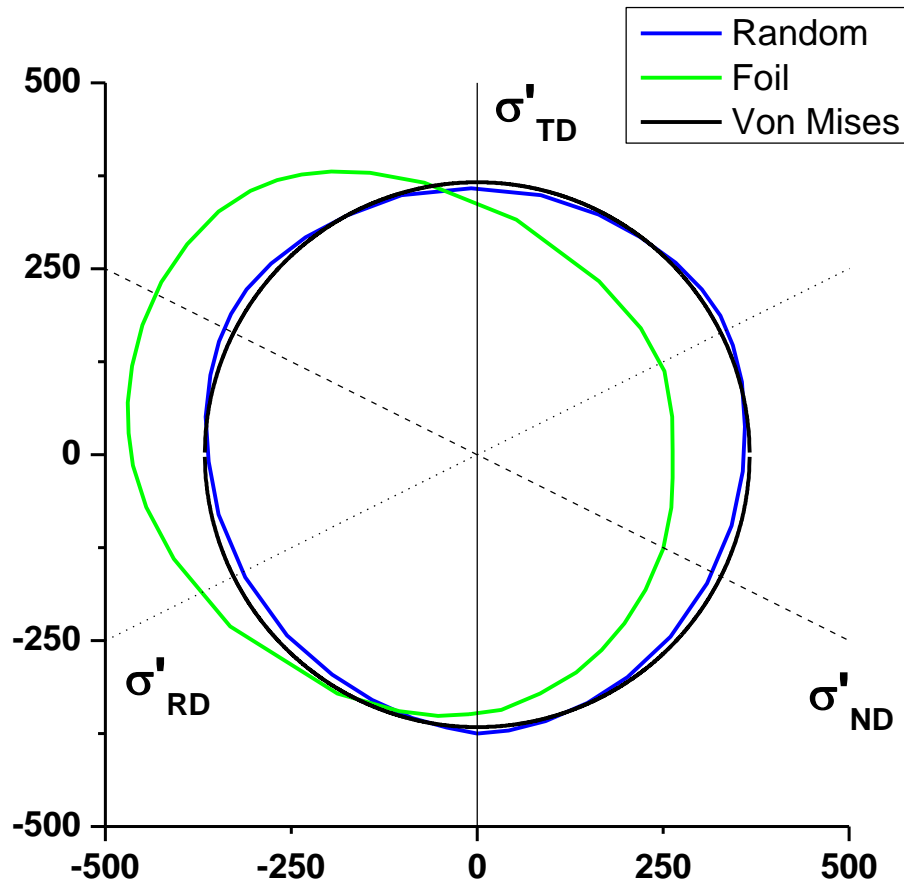


Figure 35 - π -plane projections of the yield surfaces for a random texture as well as the measured texture from the foil.

4.2 Extrusion of Magnesium

4.2.1 Model Results

This section adapted from, "Development of Thin-walled Magnesium Alloy Extrusions for Improved Crash Performance Based Upon Texture Control," by Bruce W. Williams, Sean R. Agnew, Robert W. Klein, and Jonathan McKinley [6].

The FE-VPSC model results for Profile #3 (Figure 36) and Profile #8 (Figure 38) (both described in Table 3Error! Reference source not found.) are developed to characterize the range of producible textures via the extrusion process, even hypothetical processes which may not be physically realizable. The evolution

of the components of the deformation gradient for Profile #3 show that the material initially undergoes a compression in the y-direction (F_{22} in Figure 37a) as the material flows into the 3 mm gap (Figure 36), followed by tension as the material flows around the sharp corner. The opposite trend is predicted for F_{11} . F_{33} indicates that the material undergoes tension in the z-direction as the material flows from a bar to a tube of larger circumference. The F_{12} and F_{21} components indicate a strong reversal in the sense of shear as the material first undergoes strong shear in one direction as it flows into the gap and then shears in the opposite sense as it flows around the corner. The velocity gradient in Figure 37b shows that the largest magnitudes, both negative and positive, occur as the material initially flows into the gap and then around the corner. This same trend is present in all of the tube extrusion simulations, though the level of shear and reverse shear are different for the different profiles. The trends are slightly different in Profile #8. Figure 39a indicates that the material undergoes a large tensile strain in the y-direction (F_{22}) as the material is compressed in the x-direction (F_{11}). F_{33} indicates compression as the material flows from the pierced billet of larger outer circumference to a tube of reduced circumference. Figure 39b indicates that the magnitudes of the velocity gradients are largest for the shear component L_{21} as the material flows through the transition zone (Figure 38).

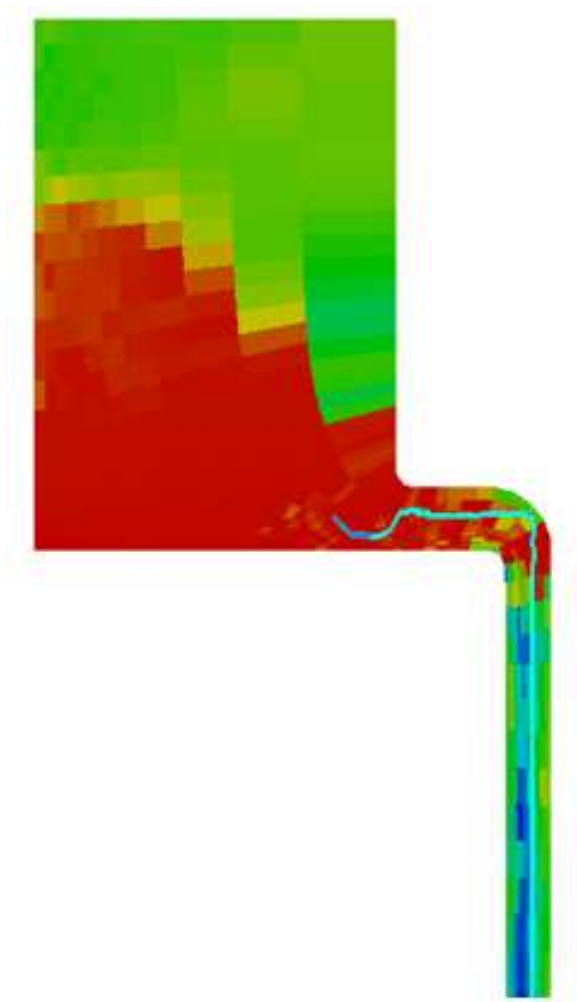
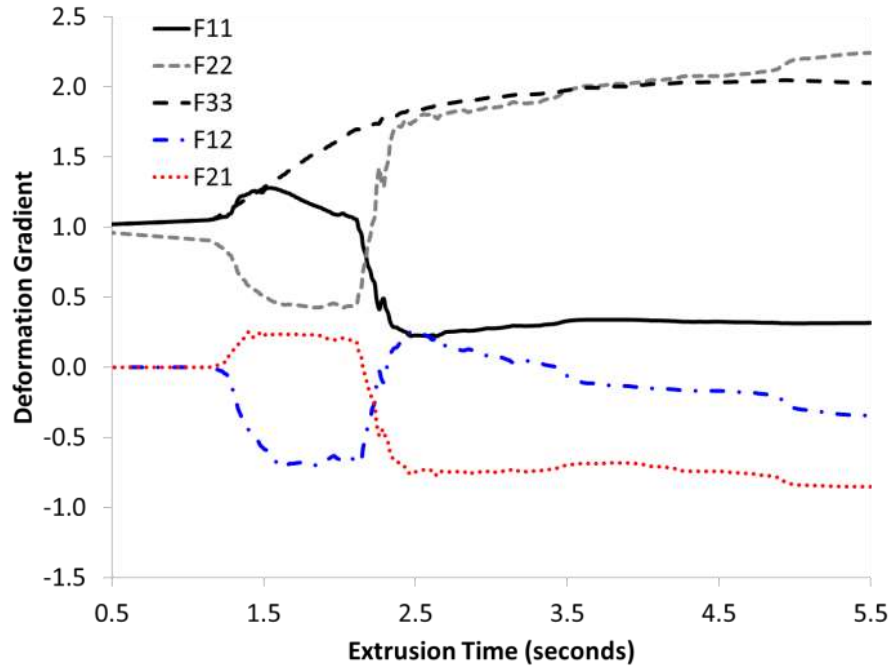
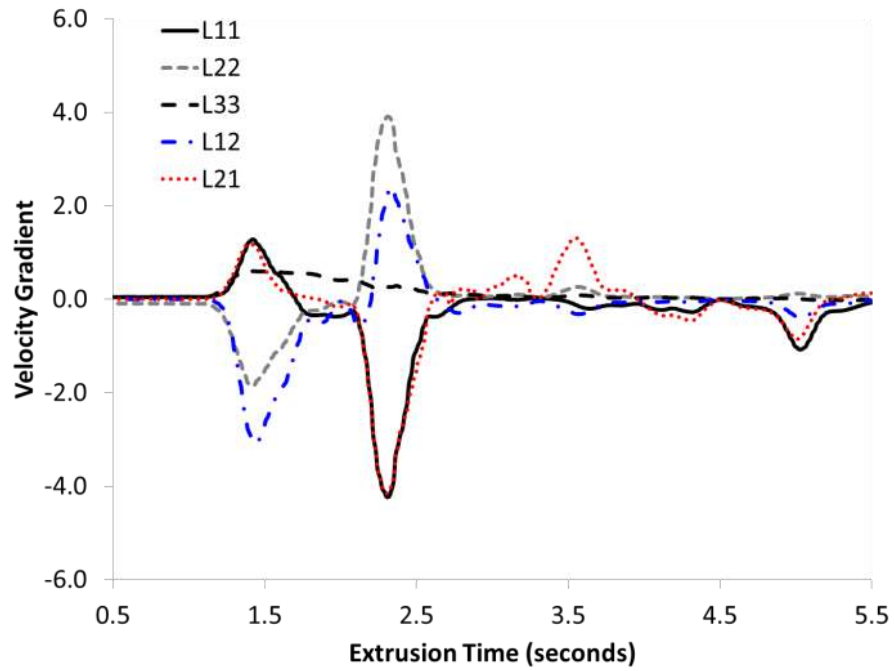


Figure 36 - Path line utilized to track deformation gradient during extrusion simulations from Profile #3. Contours of von Mises effective stress, max = 105 MPa. The color contouring represents von Mises effective stress, max = 105 MPa is colored red.



a)



b)

Figure 37 - Time evolution of the components of a) the deformation and b) the velocity gradient predicted from the simulation of Profile #3.

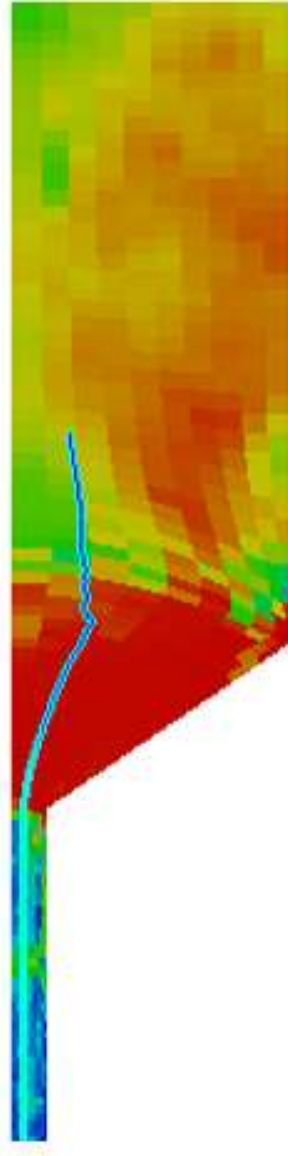


Figure 38 - Path line utilized to track deformation gradient during extrusion simulations from Profile #8. Contours of von Mises effective stress, max = 105 MPa. The color contouring represents von Mises effective stress, max = 105 MPa is colored red.

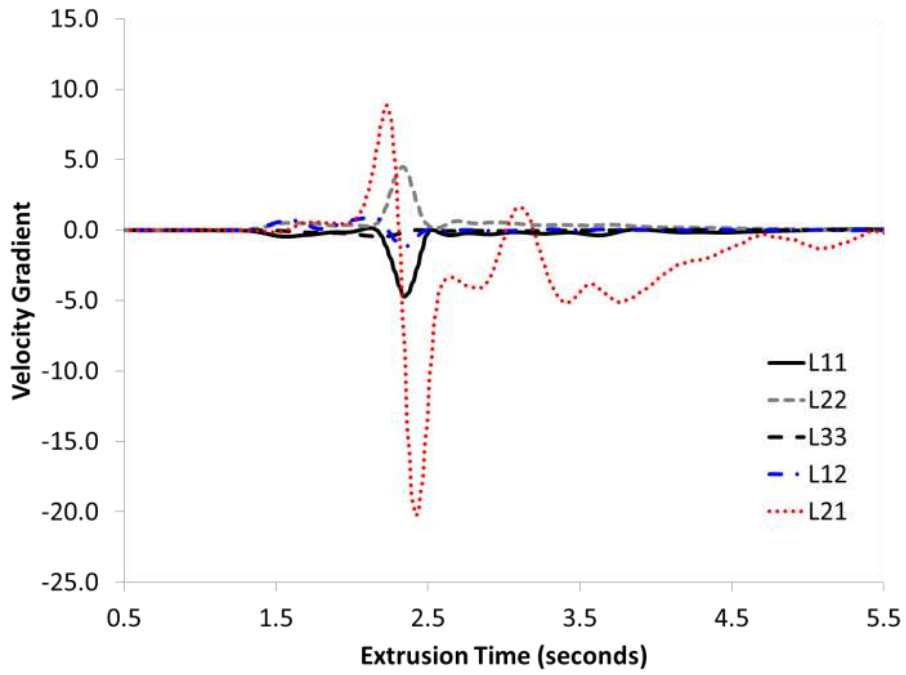
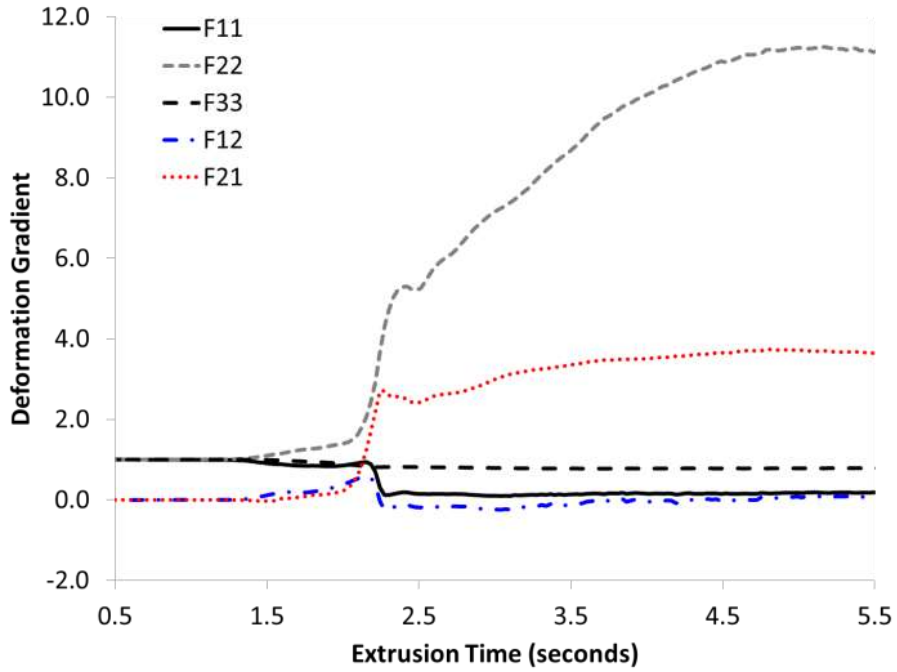


Figure 39 - Time evolution of the components of a) the deformation and b) the velocity gradient predicted from the simulation of Profile #8.

Figure 40 and Figure 41 show the result of applying the strain histories obtained from Profile #3 and Profile #8, respectively, and employing them as inputs to the VPSC code. The (00.2) pole figures for

Profile #3 and Profile #8 both feature intensities aligning with the RaD (Radial direction). The rotation of the features such that they do not perfectly align with RaD is a function of the shear experienced during the extrusion process. Profile #8 also includes a feature with some intensity sweeping from the RaD across to the hoop direction. The texture observed in the pole figures for Profile #8 is a rational combination of that observed in axisymmetric bar extrusion, which results in (10.0) poles parallel to the ED, and plane strain compression, which places the (00.1) poles nearly parallel to the RaD.

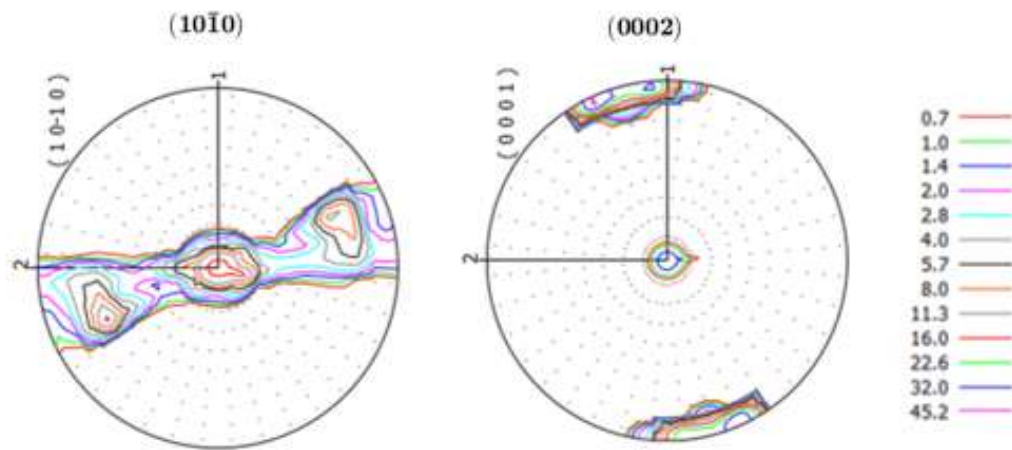


Figure 40 - Basal and prismatic pole figure resulting from the extrusion of Profile #3 with CRSS ratio of 1:6:6. RaD points upward, and ED points to the right.

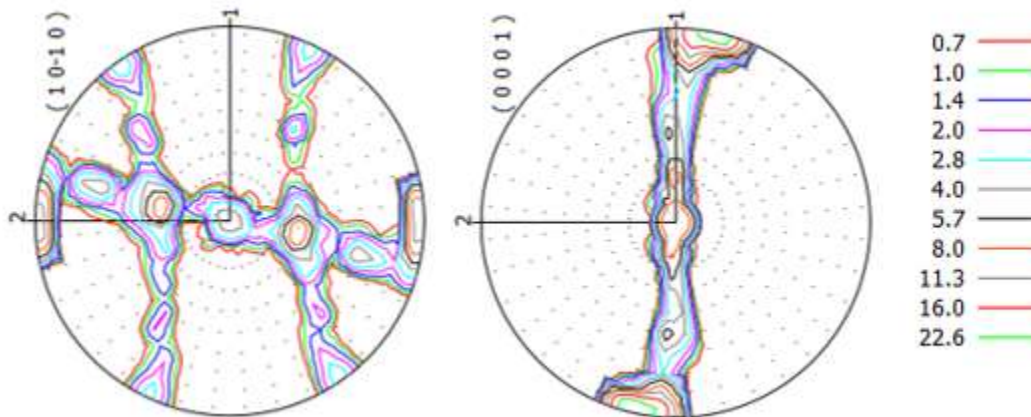


Figure 41 - Basal and prismatic pole figure resulting from the extrusion of Profile #8 with CRSS ratio of 1:6:6. RaD points upward, and ED points to the right.

4.2.2 Microstructure Results

This section adapted from, "Exploration of Thin-walled Magnesium Alloy Tube Extrusion for Improved Crash Performance," by Robert W. Klein, Bruce W. Williams, Jonathan McKinley, John R. Einhorn, and Sean R. Agnew [5].

The billets used in this study were commercially extruded AZ31B and laboratory cast ZEK100, and their textures were investigated using XRD. The recalculated pole figures obtained from the pre-extruded AZ31B billet are presented in Figure 42a, viewed down the axis of extrusion. These pole figures show axisymmetry with two components, one with the (00.2) poles parallel and the other with (00.2) poles nearly perpendicular to the extrusion axis. The ZEK100 alloy was investigated via representative specimen, which was cut from the center of the casting (Figure 42b). As expected, the overall texture of this as-cast material is weak. There is an unexpected feature of the texture as the (00.2) poles appear to have a preferred orientation rotated away from the axis of the casting.

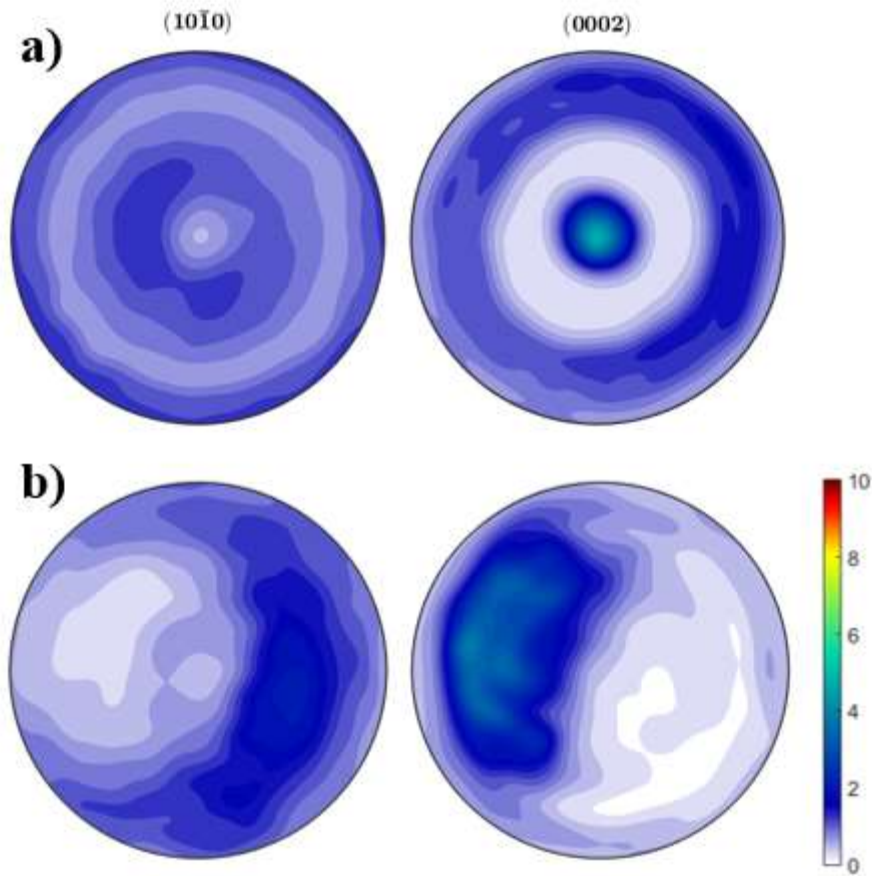


Figure 42 - Recalculated pole figures from the pre-extruded billet of AZ31B (a) and the as-cast ingot of ZEK100 (b). Pole figures are viewed down the axis of the samples (Note all of the Mg-alloy pole figures employ the same contouring and color spectrum).

The texture of the thin-walled top-hat specimen of the AZ31B is presented in Figure 43. The texture of the outermost surface is presented in Figure 43a and that of the mid-plane of the “bridge” section (obtained by grinding through sufficient material) is shown in Figure 43b. The surface texture shows that the (00.2) poles lie near the normal direction (ND), similar to a conventional Mg alloy sheet texture [12], albeit with a slight tilt, due to the shear induced by contact with the die. For the mid-plane, there is a band of (00.2) pole intensity perpendicular to the extrusion axis, with the highest intensity components tilted from the normal direction and towards the transverse direction.

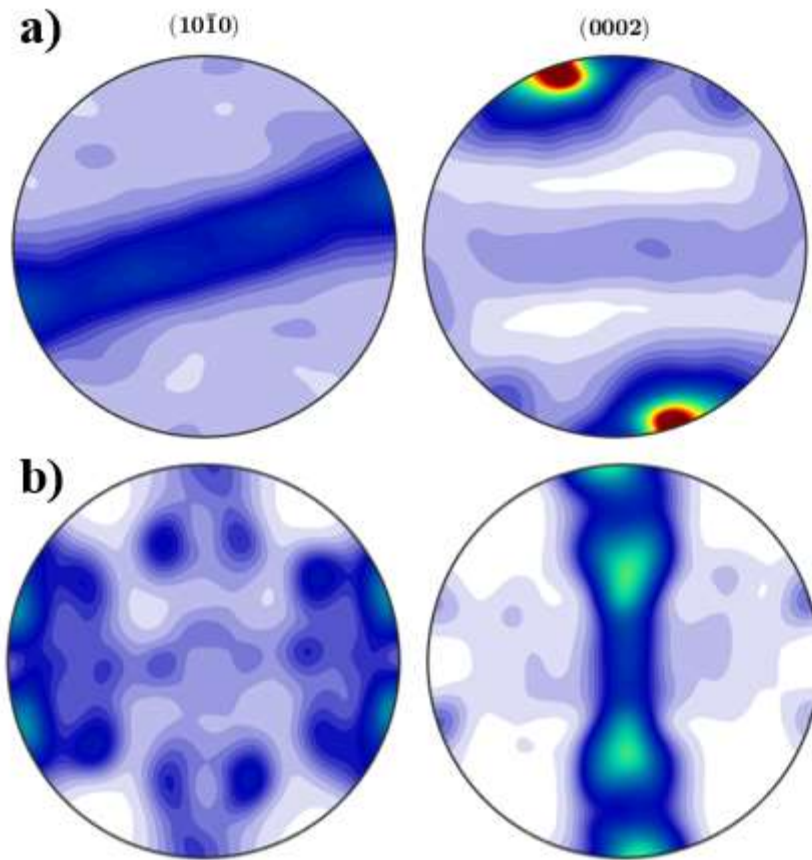


Figure 43 - Recalculated pole figures for the AZ31B top-hat specimen at the a) surface and b) mid-plane. Pole figures plotted with the ND pointing upwards and the ED facing left.

The texture of the thin-walled top-hat specimen of the ZEK100 is presented in Figure 44. The texture of the outermost surface is presented in Figure 44a and that of the mid-plane of the “bridge” section is shown in Figure 44b. The surface texture of the ZEK100 sample shows the (00.2) poles to be only slightly inclined from the ND, as observed for alloy AZ31B. In the mid-plane pole figures, the ZEK100 texture is shown to have a feature where the (00.2) poles are nearly perfectly aligned with the ND. The mid-plane (00.2) pole figure also features a band of preferred orientations sweeping from the extrusion direction (ED) to the transverse direction.

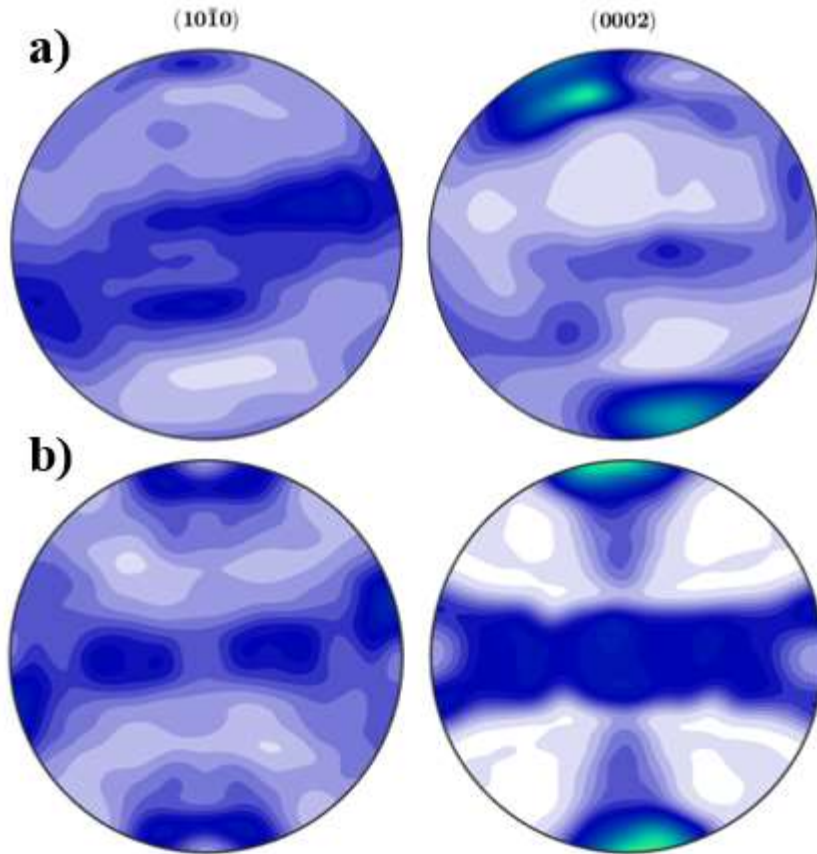


Figure 44 - Recalculated pole figures for the ZEK100 top-hat specimen at the a) surface texture and b) mid-plane. Pole figures plotted with the ND pointing upwards, and the ED facing left.

The measured surface textures of the top-hat specimens of both AZ31B and ZEK100 are qualitatively similar, though the AZ31B texture is stronger. Pole figures for both alloys possess dyadic symmetry, and show the c-axes close to ND. The slight rotation of the c-axes from ND counter clockwise about the TD gives the impression of shear from friction, a notion supported by the absence of this feature in the mid-plane textures. The dyadic symmetry and near ND preference of the (00.2) poles correlates well with textures predicted by crystal plasticity simulations in a previous study [14].

Measured mid-plane textures for the top-hat specimens of AZ31B and ZEK100 are more dissimilar from each other. Both textures exhibit near orthotropic symmetry and have the c-axes of the grains closely aligned with the ND. The degree of symmetry suggests that the mid-planes experience pure shear

deformation. A difference between the AZ31B and ZEK100 pole figures is the presence of lobes, tilted between ND and TD (transverse direction), in the (00.2) pole figure of the AZ31B texture measurement. The absence of these lobes in the ZEK100 pole figure could be explained by the rare-earth alloying elements impeding recrystallization, which is one explanation that has been invoked to explain the weaker textures sometimes observed in rare earth containing alloys [11] [34].

A thin-walled tube specimen of the AZ31B made via the mandrel tooling was investigated using EBSD. Three EBSD scans were performed on this sample. The EBSD scans were taken at varying distances along the radial direction (RaD) on a plane normal to the tangential (hoop) direction (HD), as visualized in Figure 45. A thin-walled tube specimen of the ZEK100 alloy, also made by means of the mandrel tooling, was investigated using EBSD. Five EBSD scans were performed on this sample, at different locations along the radial direction of piece, on a plane normal to ED, as drawn schematically in Figure 46. The microstructure is shown as an inverse pole figure map for AZ31B (Figure 47a) and ZEK100 (Figure 47b). Note that the grain size is finer in the ZEK100. Notably, no strong variations in microstructure were observe along the tube radial direction in either case, though the AZ31B had a slightly finer grain size close to the inner surface tube.



Figure 45 - Schematic representation of site locations for EBSD performed on the thin-walled tube of AZ31B.

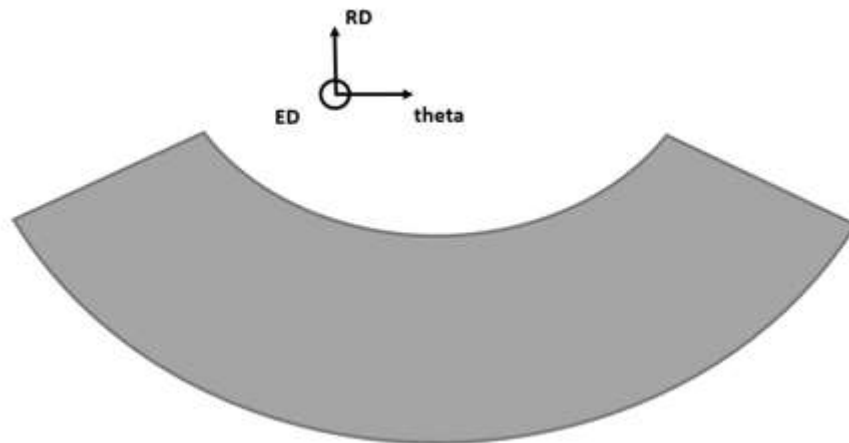


Figure 46 - Schematic representation of site locations for EBSD performed on the thin-walled tube of ZEK100.

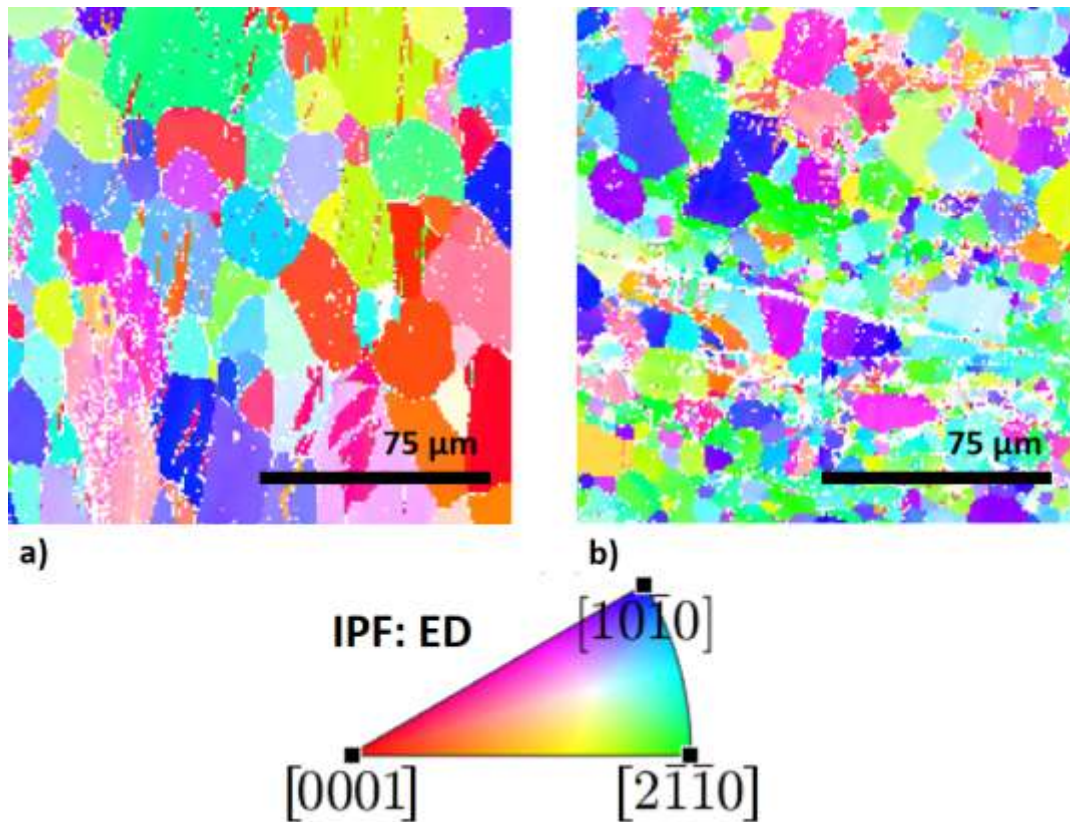


Figure 47 - Extrusion direction (ED) inverse pole figure maps showing the microstructures of a) AZ31B and b) ZEK100 extruded tubes.

As there was no significant texture gradient observed along the RaD for the AZ31B tube, a set of averaged, recalculated pole figures is featured in Figure 48. These pole figures show a preference for the c-axes of the grains to align close to the RaD, although they are tilted slightly aft of the precise RaD. Additionally, there is a weaker texture component with (00.2) poles parallel to the HD. The (10.0) recalculated pole figure exhibits a band of preferred orientations from the extrusion direction to theta, with highpoints along the ED and HD. Note also the 6-fold symmetry of the weak (10.0) peaks along the rim of the pole figure, which correspond to the (00.2) poles parallel to the HD (at the center of that pole figure).

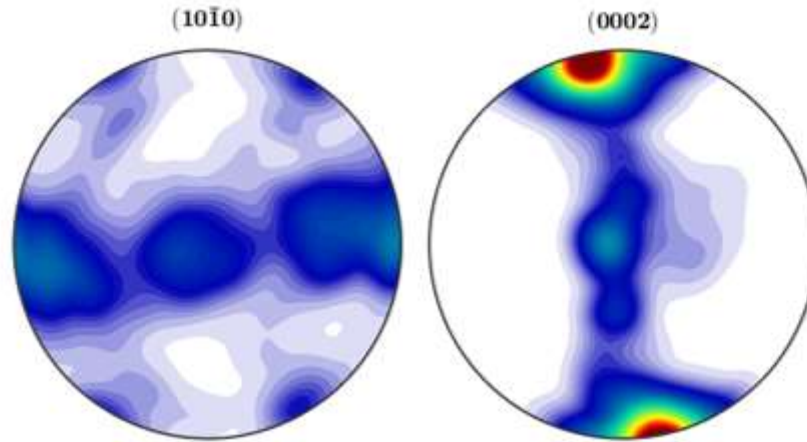


Figure 48 - Full pole figures recalculated from the complete ODF of an AZ31B thin-walled tube specimen. Pole figures plotted with the RaD points upwards, and the ED faces left.

Again, no significant gradient was seen in the texture of the ZEK100 tube, so the average recalculated pole figures are featured in Figure 49. The (00.2) poles lie along the radial direction for this texture, with a slightly larger rotation towards the ED. Further, the (10.0) poles sweep from ED to HD, with a slight preference to lie parallel to the ED and no preference for the HD which was observed in the case of AZ31B.

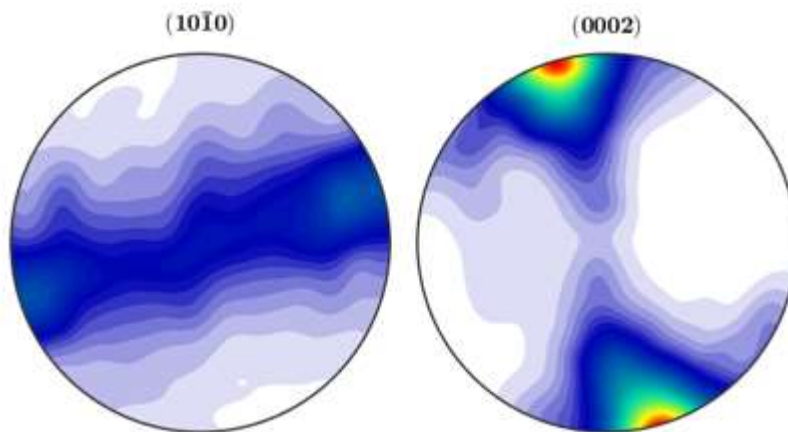


Figure 49 - Full pole figures recalculated from the complete ODF of a ZEK100 thin-walled tube specimen. Pole figures plotted with the RaD pointing upwards, and the ED pointing left.

The measured textures of the extruded tubes of both AZ31B and ZEK100 are also qualitatively similar, with the AZ31B texture appearing slightly stronger. While both of the textures show the c-axes close to the RaD, the AZ31B (00.2) pole figure contains an additional feature, a preferred orientation along the HD. Results from previous work suggest that this texture might be characteristic of deformation by plane strain compression due to its similarity to rolled Mg textures, and was most prominent in cases where the prismatic slip mechanism was dominant [14].

Two thin-walled tubes of the WE43 made via the mandrel tooling were also investigated using EBSD. The first of these thin-walled tubes was characterized in its as-extruded condition, while the other had an annealing step performed post-deformation. The EBSD scans performed on the tubes were done along at varying distances along the radial direction of the samples, as was done with the ZEK100 sample, visualized in Figure 46. The microstructure is shown as an inverse pole figure map for the as-extruded (Figure 50a) and the annealed (Figure 50b). No strong gradients were observed along the tube radial direction in either case. The grain size is considerably finer in the as-extruded condition than in the annealed condition.

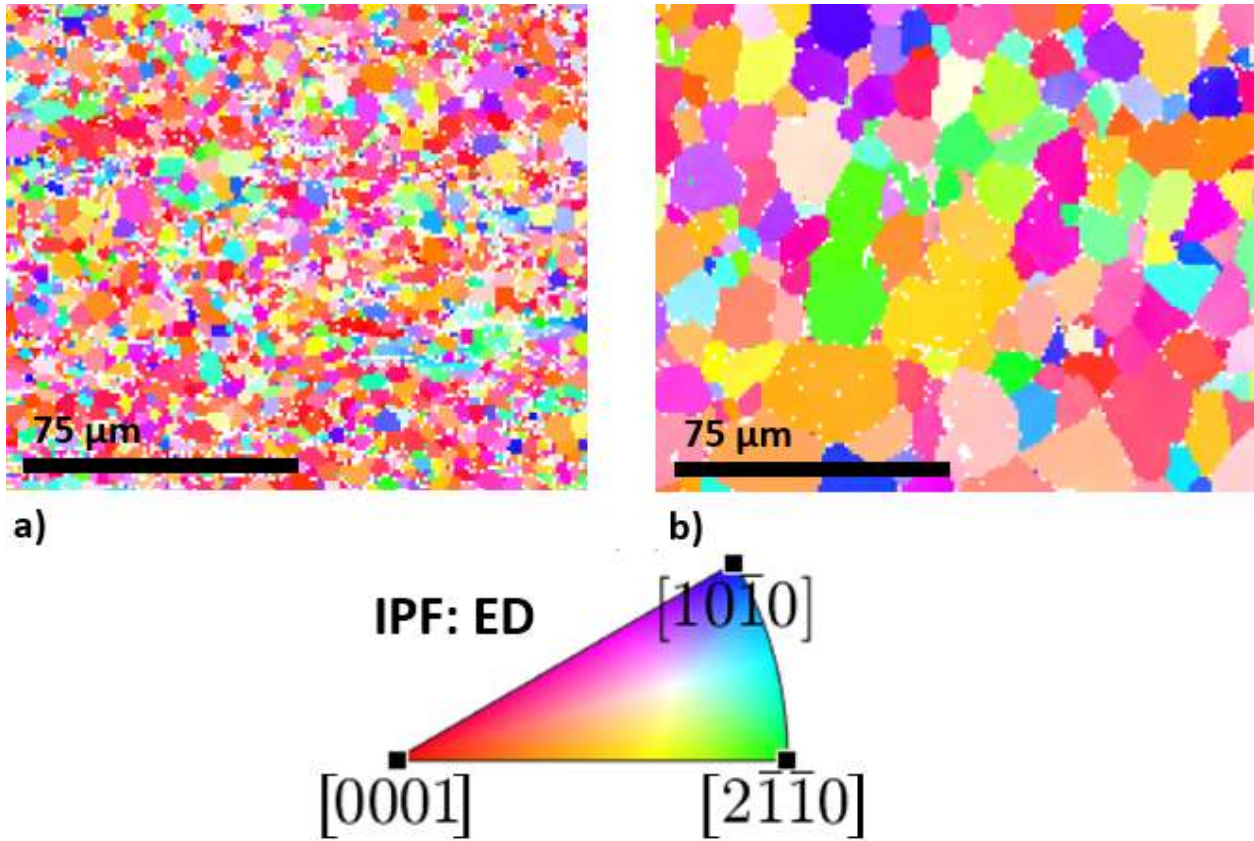


Figure 50 - Extrusion direction (ED) inverse pole figure maps showing the microstructures of a) as-extruded WE43 and b) annealed WE43 extruded tubes.

The recalculated pole figure plots for the as-extruded sample are presented in Figure 51. These pole figures show a preference for the c-axes of the grains to align close to the RaD, but like the textures of the AZ31B and ZEK100 tubes, the c-axes are tilted slightly aft of the precise RaD. The (00.2) poles also show a preferential orientation set 45° from the ED. This texture is weaker than those previously discussed for the extruded material, but this is probably a feature of the larger number of grains sampled via the finer microstructure.

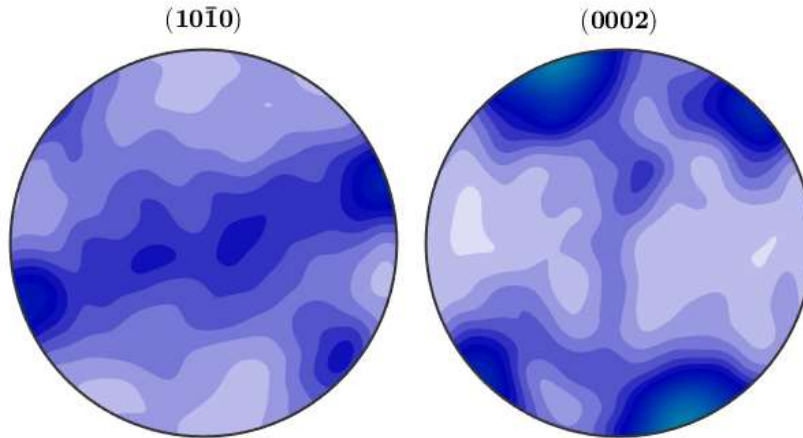


Figure 51 - Full pole figures recalculated from the complete ODF of an as-extruded WE43 thin-walled tube specimen. Pole figures plotted with the RaD pointing upwards, and the ED facing left.

The texture of the annealed thin-walled tube specimen of WE43 is presented in Figure 52. This recalculated pole figure shows a preference for the (00.2) poles to align just aft of the RaD. Similarly to the as-extruded WE43 texture, there is an additional preference for the (00.2) poles to align 45° from the ED. An additional feature of this texture is that some c-axes align near the ED. Both of the features unique to the WE43 textures, (00.2) alignment 45° from the ED and (00.2) alignment near the ED, are also observed in XRD investigations of these samples, as shown in Appendix A.

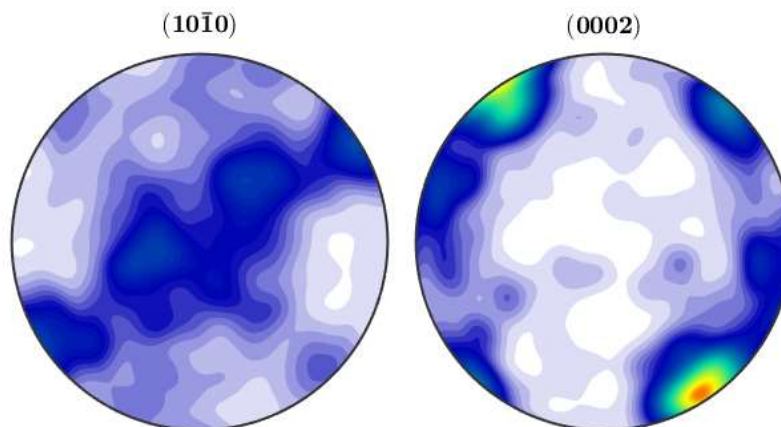


Figure 52 - Full pole figures recalculated from the complete ODF of an annealed WE43 thin-walled tube specimen. Pole figures plotted with the RaD pointing upwards, and the ED facing left.

4.2.3 Axial Crush Results

This section adapted from, "Exploration of Thin-walled Magnesium Alloy Tube Extrusion for Improved Crash Performance," by Robert W. Klein, Bruce W. Williams, Jonathan McKinley, John R. Einhorn, and Sean R. Agnew [5].

Subsequent axial crush tests were performed on the AZ31B, ZEK100, and WE43 circular tube extrusions. In all cases, the tubes fractured on the first fold as opposed to the progressive buckling observed for steel and aluminum alloy tubes under axial crush (Figure 53, Figure 54, and Figure 55). The force versus displacement curves for the AZ31B samples are shown in Figure 56 and for the ZEK100 samples in Figure 57. In Figure 58, the force displacement curves for the WE43 samples are shown.



Figure 53 - Final specimen condition of the axial crush tests performed on AZ31B thin-walled tubes extruded at (from left to right): 250, 300, 350, 250 (and annealed), 300 (and annealed), and 350 and annealed.



Figure 54 - Final specimen condition of the axial crush tests performed on ZEK100 thin-walled tubes extruded at (from left to right): 275, 300, 450, 275 (and annealed), 300 (and annealed), and 450 and annealed.



Figure 55 - Final specimen condition of the axial crush tests performed on WE43 thin-walled tubes extruded at (from left to right): 350, 400, 450, 350 (and annealed), 400 (and annealed), and 450 and annealed.

The initial load at yielding for the ZEK100 tubes was greater than the peak load for the AZ31B tubes.

The initial yielding load of about 51 kN for the ZEK100 tube extruded using the mandrel at 350 °C was higher than most of the other tubes for which the initial buckling load was between 34 to 40 kN.

Interestingly, the yielding load of the slow AZ31B tube extruded using the mandrel at 400 °C was only about 22 kN. After initial yielding, the force response for all of the tubes was similar with an increasing load to about 60 kN. The only exception to this trend of increasing load was for the ZEK100 tube extruded using the mandrel at 350 °C in which the load increases only slightly to a displacement of 7 mm before decreasing. After initial yield, the AZ31B and ZEK100 tubes experience a plateau, which indicates that the strain is being accommodated via twinning modes.

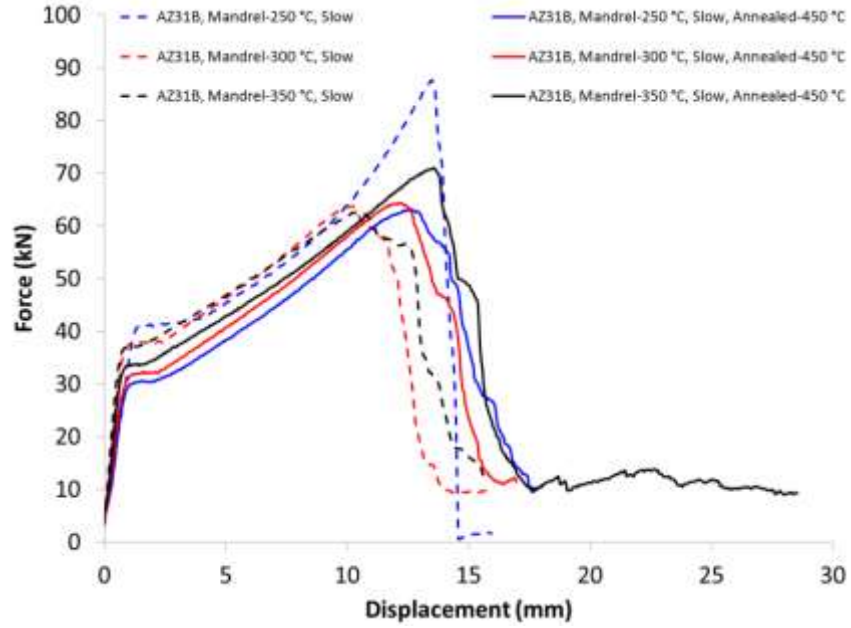


Figure 56 - AZ31B Axial Crush Results displayed as a curve measuring force against displacement. Different lines represent the different processing history of the tubes subjected to the crush test.

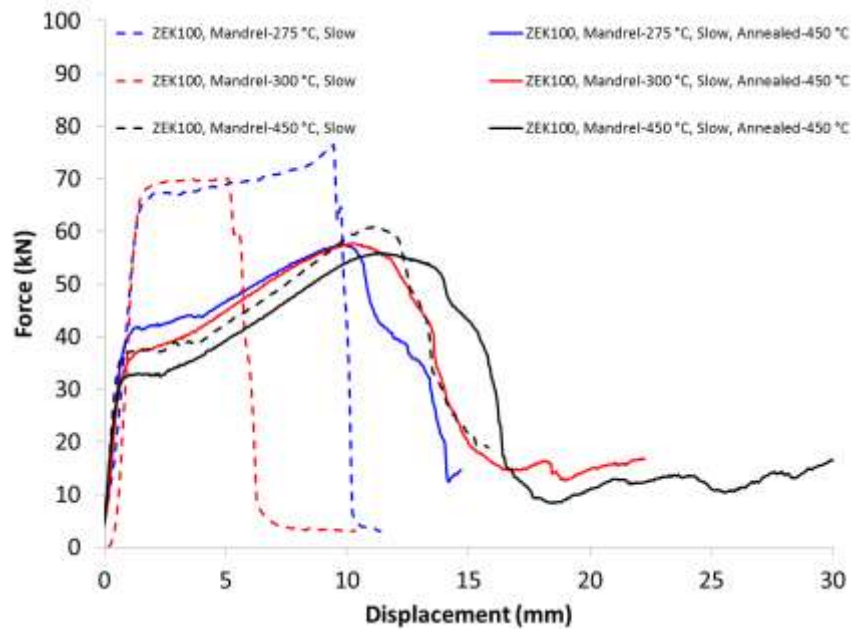


Figure 57 - ZEK100 Axial Crush Results displayed as a curve measuring force against displacement. Different lines represent the different processing history of the tubes subjected to the crush test.

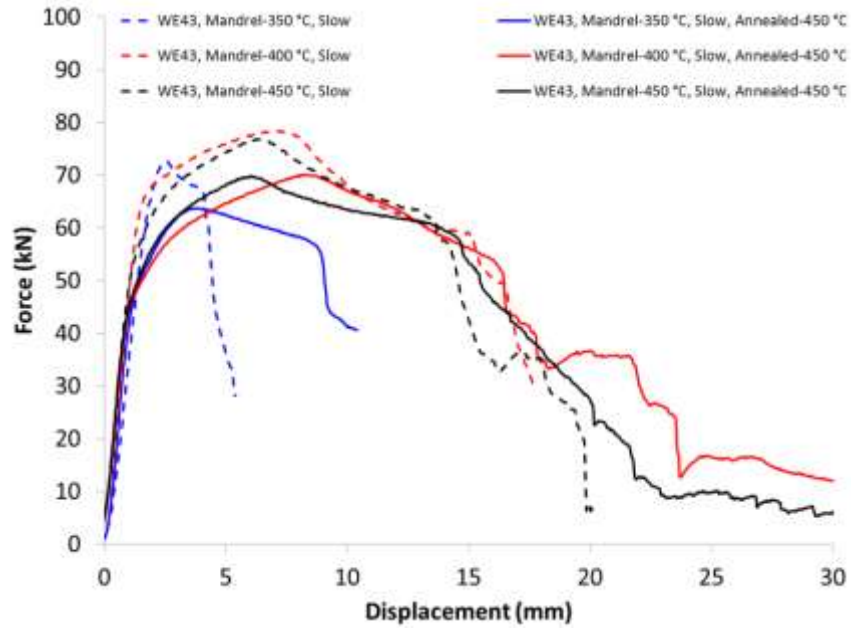


Figure 58 - WE43 Axial Crush Results displayed as a curve measuring force against displacement. Different lines represent the different processing history of the tubes subjected to the crush test.

The figure of merit for this crush response investigation is energy absorption, which can be measured as the integral area under the presented force-displacement curves, measured out to 30 cm (Figure 59). In general, the ZEK100 tubes exhibited only a slight improvement in the axial crush response compared to the AZ31B tubes. There are two possible explanations for the observed behavior. The first is the possibility that the ZEK100 tube has a higher overall strength due to the finer grain size. The other relates to the possibility that the distinct crystallographic texture (i.e., the slightly higher degree of tilt of the basal poles away from RaD) causes a specific increase in the compressive strength. Note that the hcp crystals compressed orthogonal to the c-axes are prone to undergo tensile twinning. By rotating the c-axes away from the RaD, twinning deformation is suppressed. This could have the effect of reducing the tension-compression asymmetry and improving the compressive ductility by blending a combination of slip and twin accommodated deformation, rather than relying on twin dominated deformation, which has been associated with premature compression failures of highly textured extrusions. Because the texture is only slightly different between the two cases, it is suggested that the grain size difference is the major

contributor. Simulations of a compression response using the two extrusion textures as input would be informative.

The WE43 tubes show a significant improvement in energy absorption over their AZ31B and ZEK100 counterparts. Most of delta in area under the force-displacement curve comes from the initial hardening. AZ31B and ZEK100 tubes experience a twinning-type hardening plateau, but the WE43 tubes experience a parabolic hardening curve, which is indicative of slip accommodating the strain. As noted in the literature, twinning is much harder in WE43 [35]. The texture of the WE43 components can also explain the absence of the twinning-type plateau. Two additional features appear in the WE43 pole figures. One of these is oriented 45° from the ED, and shows grains which can better accommodate basal slip. The other feature directly aligns with ED, and opposes c-axis extension twinning.



Figure 59 - Portrays the figure of merit, energy absorption, as a function of alloy and processing history (extrusion temperature and anneal conditions).

Chapter V

5 Conclusions

5.1 Microstructure and Properties of Cold-rolled α -U Foil

A finite element model of rolling with geometry appropriate for the U foil rolling process was developed using ABAQUS explicit. Strain histories (i.e., velocity gradients) were determined using the EnSight post-processing software. The FE-VPSC modeling methodology, which employed these strain histories as inputs, predicts a cold rolled α -uranium texture typical of plane strain compression. The predicted texture does exhibit some asymmetry due to roller-foil contact, especially at the surface of the simulated workpiece.

The experimental U foil texture exhibits the (020) poles oriented in all direction perpendicular to the ND, with a strong preference to align with the RD. In addition, the (002) peaks preferentially align towards the ND, but with two symmetrically equivalent peaks tilted towards the TD. The FE-VPSC modeling methodology predicts a cold rolled α -uranium texture that also has (020) poles oriented in all directions perpendicular to the ND, with a preference for near the RD. The cold rolled texture prediction features the (002) poles preferentially aligning towards the ND, and splitting towards the RD. This predicted texture has less symmetry at the surface than at the midplane of the simulated workpiece. Both the midplane and surface texture predictions are similar to the midplane and surface predictions made by Zecevic et al. [31]. Recrystallization effects are necessary to explain the observed differences between the experimentally measured texture and the predicted texture.

The resulting microstructure and predicted property highlights the foil's anisotropy. Elastic and thermal properties were predicted based upon the functional forms of single crystal thermo-elastic properties and self-consistent polycrystal averaging. Plastic properties were predicated via VPSC's capability to

generate yield surfaces and stress-strain curves based upon inputs of the single crystal plastic behavior and a texture input. The property predictions reveal that the resulting foil will exhibit near elastic isotropy, moderate thermal expansion anisotropy, and strong plastic anisotropy.

5.3 Texture Control of Extruded Mg-Alloy Thin-Walled Tube Components

Force versus displacement curves were measured in a series of axial crush tests performed on thin-walled tube components made of either AZ31B, ZEK100, or WE43. WE43 alloy tubes demonstrate improved energy absorption over tubes made of different Mg-alloys. The hardening behavior of the WE43 tubes is parabolic, which sharply contrasts with the twinning-type plateau experienced by the other two alloys. The texture of the WE43 alloy tubes contains unique features which explain absence of twinning plateau in its force-displacement curves. The WE43 alloy tubes have a preferred orientation of the (00.2) poles 45° from the ED, which makes basal slip more accessible of a deformation mode to accommodate strain. In addition, the WE43 texture contains a feature with (00.2) poles aligning near the ED, which impedes c-type extension twinning.

The range of feasible textures produced via altered extrusion tooling in thin-walled Mg-alloy extrusion is limited. Vastly different strain paths were investigated via a continuum level FE approach. The strain histories from the FE models were used as inputs to a VPSC code, which predicted textures that contain the feature of (00.2) preferring to align near the RaD. One extrusion tooling profile, dubbed Profile #8 as noted in Table 3, also includes a feature with some intensity sweeping from the Rad across to the hoop direction.

Appendix A: Experimental Pole Figures

A.1 DU Pole Figures

The uranium foil samples were investigated with both Cu and Mo radiation sources. The text features a recalculated pole figure from the completed ODF as investigated by the Cu radiation source. Each of the pole figure plots for the samples are featured here to provide a complete data set.

RD points upward, TD points right, and ND points out of the page.

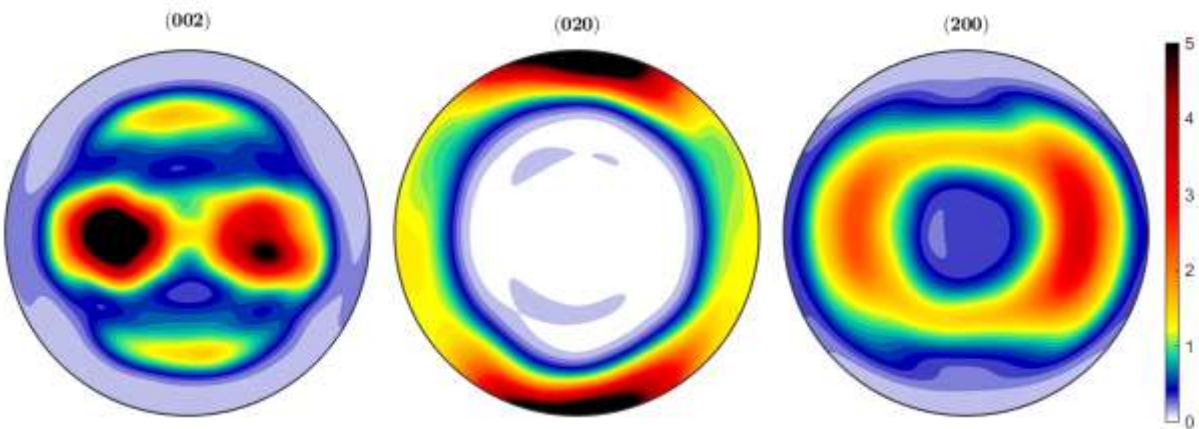


Figure 60 - Experimentally measured texture of first DU foil sample via Cu radiation source. RD points upward, TD points right, and ND points out of the page.

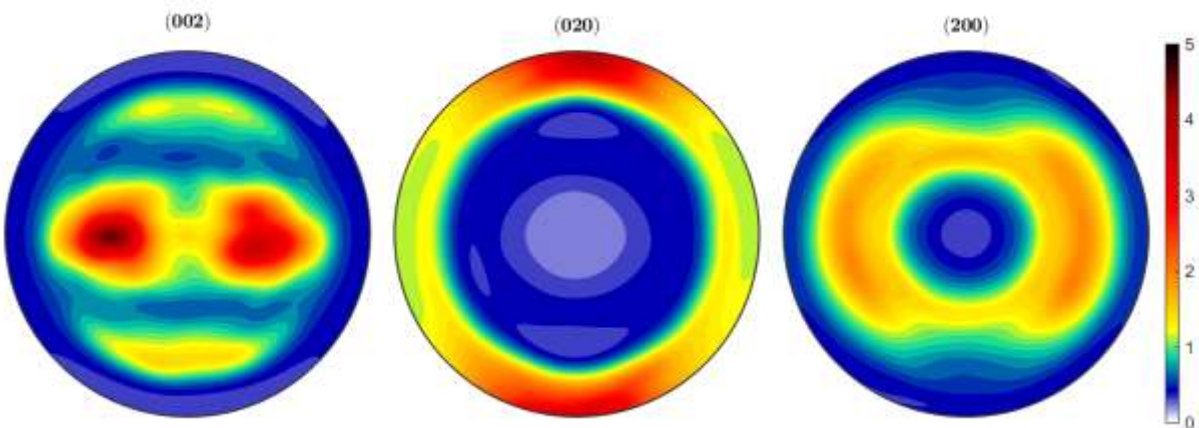


Figure 61 - Experimentally measured texture of second DU foil sample via Cu radiation source. RD points upward, TD points right, and ND points out of the page.

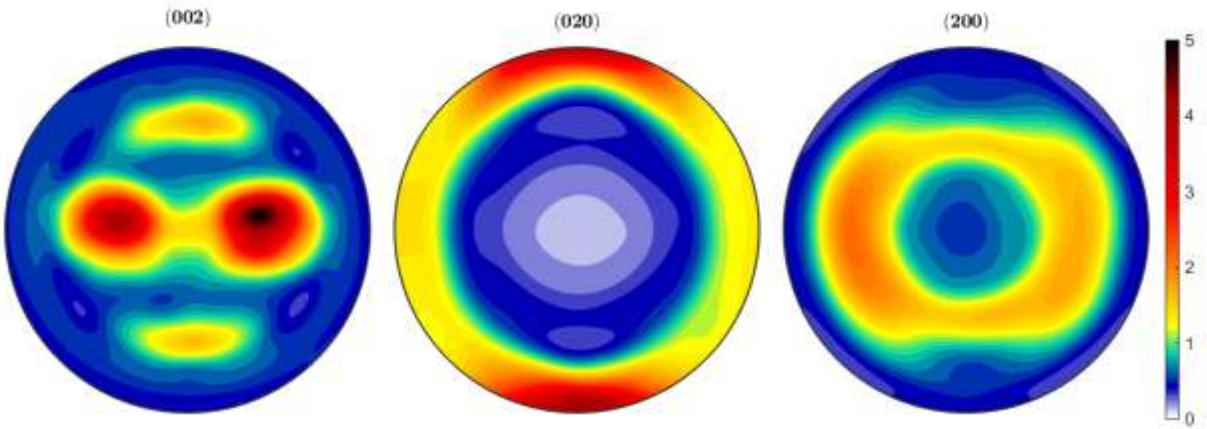


Figure 62 - Experimentally measured texture of third DU foil sample via Cu radiation source. RD points upward, TD points right, and ND points out of the page.

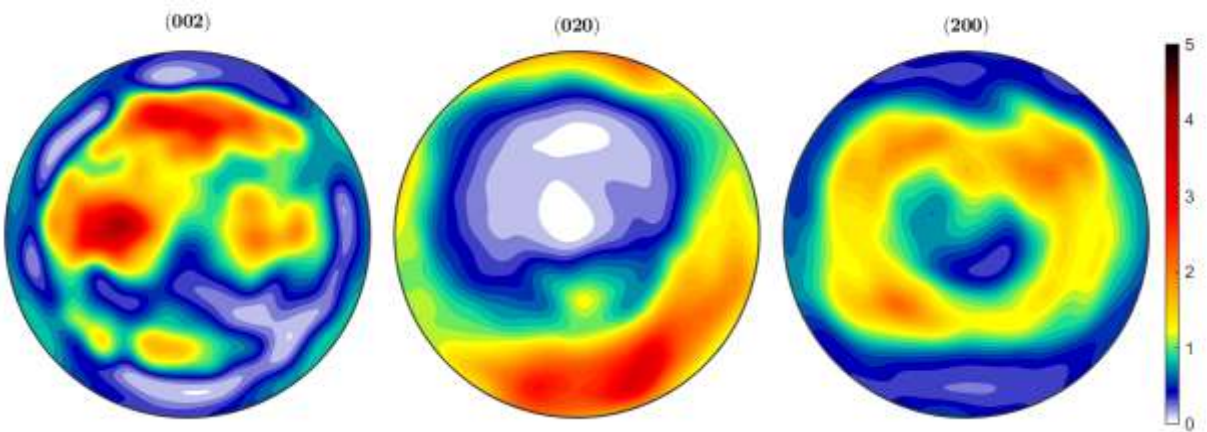


Figure 63 - Experimentally measured texture of first DU foil sample via Mo radiation source. RD points upward, TD points right, and ND points out of the page.

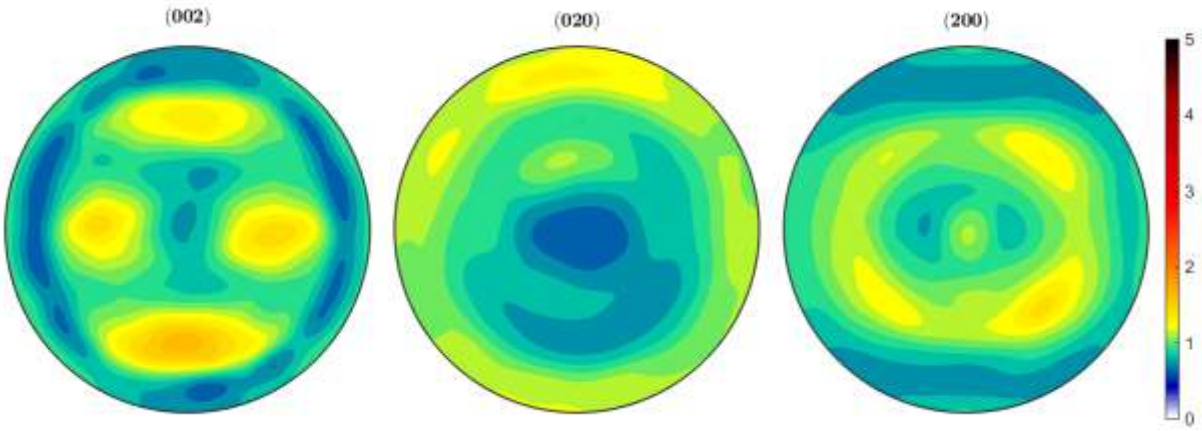


Figure 64 - Experimentally measured texture of second DU foil sample via Mo radiation source. RD points upward, TD points right, and ND points out of the page.

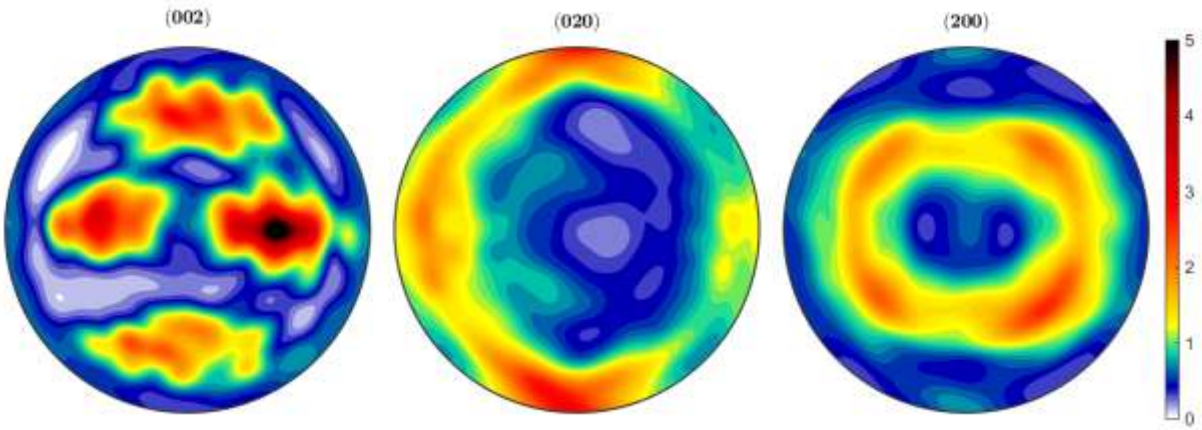


Figure 65 - Experimentally measured texture of third DU foil sample via Mo radiation source. RD points upward, TD points right, and ND points out of the page.

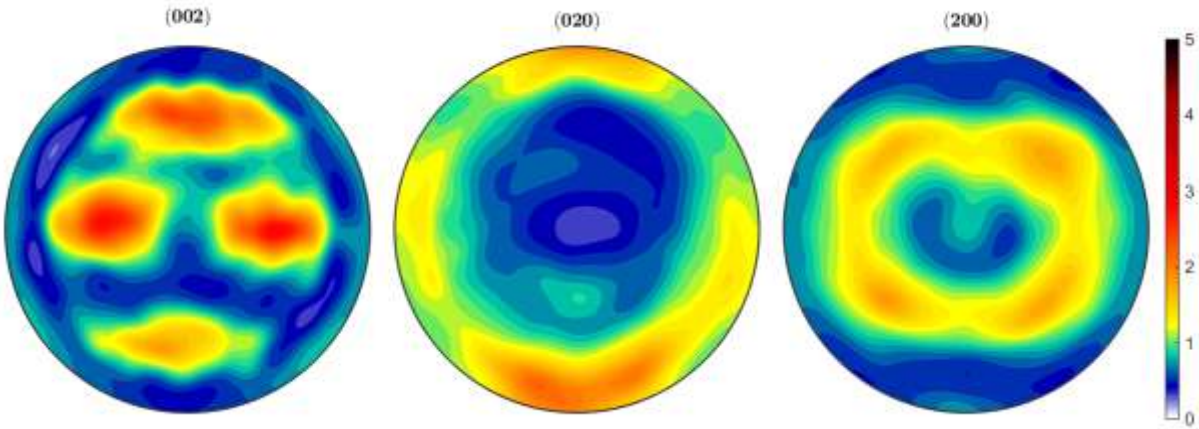


Figure 66 - Experimentally measured texture of the DU foil samples. Generated via an averaged ODF across all three samples measured with Mo radiation. RD points upward, TD points right, and ND points out of the page.

A.2 Mg Pole Figures

Additional texture data were collected on the WE43 samples via XRD analysis. Although the original sample configuration, a thin-walled tube component, was not conducive to XRD analysis (which requires a flat surface approximately 2 cm x 2 cm), a sample preparation technique was devised to enable this characterization method. Tubes were cut into a series of strips down the extrusion direction via near-radial cuts. These strips were mounted within minimal spacing between them, and polished down to a flat surface, as shown in Figure 67.



Figure 67 - Strip sample configuration, viewed down the ED of the strips. Schematic is not drawn to scale, but rather to be illustrative of the series of radial cuts and flattening of the curved surface.

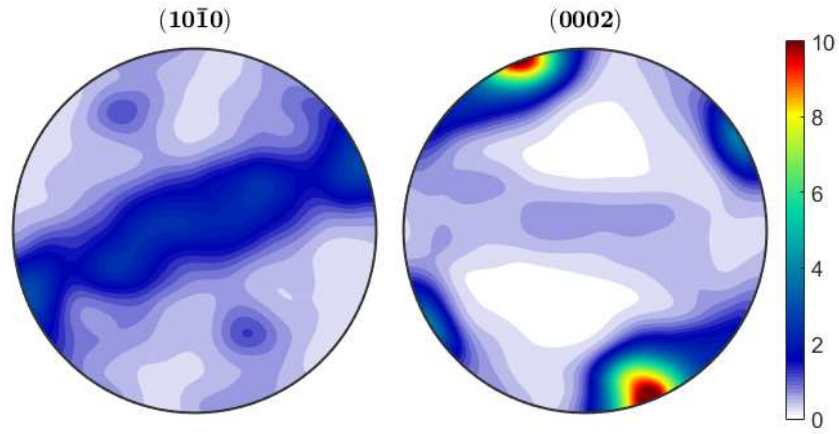


Figure 68 - Recalculated pole figures from the complete ODF measured on an as-extruded WE43 sample.

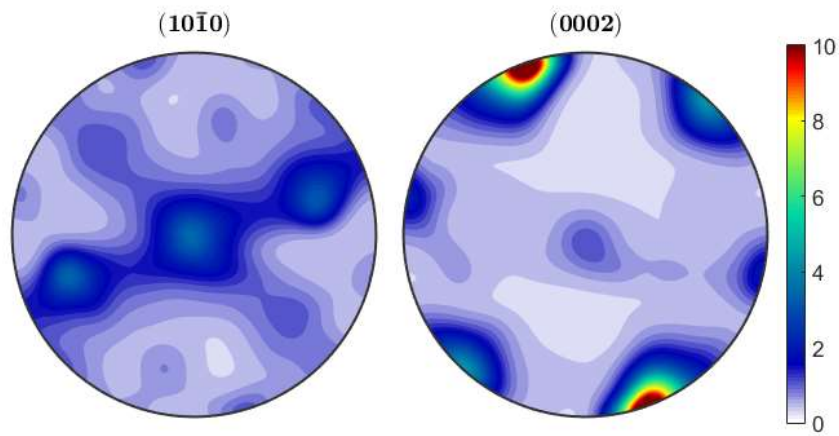
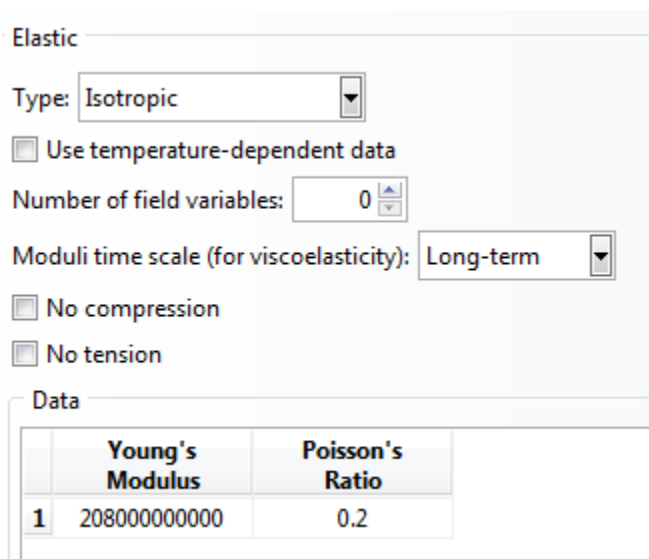


Figure 69 - Recalculated pole figures from the complete ODF measured on an as-extruded WE43 sample.

Appendix B: Cold Rolling FE Model Parameters

This appendix features details used in the creation of the cold rolling FE model. It is worth noting that ABAQUS does not have an internal unit system, and that the user is forced to remain consistent within their own notation (SI units in this case). The material properties are meant to be characteristic of α -uranium.



The image shows a software interface for defining elastic properties. It includes a 'Type' dropdown menu set to 'Isotropic', a checkbox for 'Use temperature-dependent data' which is unchecked, a 'Number of field variables' spinner set to 0, a 'Moduli time scale (for viscoelasticity)' dropdown set to 'Long-term', and two unchecked checkboxes for 'No compression' and 'No tension'. Below these options is a 'Data' section containing a table with two columns: 'Young's Modulus' and 'Poisson's Ratio'. The table has one data row with the values 208000000000 and 0.2 respectively.

	Young's Modulus	Poisson's Ratio
1	208000000000	0.2

Figure 70 - Elastic properties of the workpiece used in the cold rolling FE model of uranium [16].

Plastic

Hardening: Isotropic

Use strain-rate-dependent data

Use temperature-dependent data

Number of field variables: 0

	Yield Stress	Plastic Strain
1	595000000	0
2	687308126.4	0.00364
3	783754668.8	0.00726
4	846736957	0.0109
5	917264433	0.0166
6	980748965.3	0.0236
7	1020616164	0.0291
8	1064447474	0.0363
9	1104592819	0.0441
10	1144717674	0.0532
11	1177449349	0.0617
12	1205071651	0.0697
13	1228725316	0.0772
14	1254213875	0.086
15	1273540915	0.0932
16	1307431036	0.107
17	1327669276	0.116

	Yield Stress	Plastic Strain
18	1344617627	0.124
19	1360702421	0.132
20	1376016204	0.14
21	1394191893	0.15
22	1409729308	0.159
23	1424570088	0.168
24	1435673991	0.175
25	1446423848	0.182
26	1456843937	0.189
27	1464097114	0.194
28	1471200456	0.199
29	1478160707	0.204
30	1484984154	0.209
31	1491676663	0.214
32	1498243721	0.219
33	1504690464	0.224
34	1511021711	0.229

Data		
	Yield Stress	Plastic Strain
35	1517241984	0.234
36	1523355540	0.239
37	1529366386	0.244
38	1535278300	0.249
39	1541094848	0.254
40	1546819402	0.259
41	1552455151	0.264
42	1558005116	0.269
43	1563472161	0.274
44	1568859006	0.279
45	1574168233	0.284
46	1579402297	0.289
47	1584563537	0.294
48	1589654178	0.299
49	1594676342	0.304
50	1599632055	0.309
51	1604523251	0.314
52	1609351776	0.319

Data		
	Yield Stress	Plastic Strain
52	1609351776	0.319
53	1614119397	0.324
54	1618827806	0.329
55	1623478620	0.334
56	1628073391	0.339
57	1632613606	0.344
58	1637100691	0.349
59	1641536017	0.354
60	1645920899	0.359
61	1650256602	0.364
62	1654544341	0.369
63	1658785286	0.374
64	1662980564	0.379
65	1667131258	0.384
66	1671238415	0.389
67	1675303042	0.394
68	1679326110	0.399

Data		
	Yield Stress	Plastic Strain
70	1687251290	0.409
71	1691155181	0.414
72	1695021077	0.419
73	1698849793	0.424
74	1702642119	0.429
75	1706398820	0.434
76	1710120635	0.439
77	1713808279	0.444
78	1717462447	0.449
79	1721083808	0.454
80	1724673016	0.459
81	1728230700	0.464
82	1731757473	0.469
83	1735253928	0.474
84	1738720643	0.479
85	1742158176	0.484
86	1745567071	0.489

Data		
	Yield Stress	Plastic Strain
72	1695021077	0.419
73	1698849793	0.424
74	1702642119	0.429
75	1706398820	0.434
76	1710120635	0.439
77	1713808279	0.444
78	1717462447	0.449
79	1721083808	0.454
80	1724673016	0.459
81	1728230700	0.464
82	1731757473	0.469
83	1735253928	0.474
84	1738720643	0.479
85	1742158176	0.484
86	1745567071	0.489
87	1748947856	0.494
88	1752301043	0.499
89	1755627131	0.504

Figure 71 - Tabular data, from the Holloman equation, for the plastic behavior of uranium [15] [17].

Appendix C: VPSC Model Parameters

As stated in the text, the slip and twinning mode parameters for the VPSC model are based on those reported by Zecevic et al. [31]. Zecevic et al. detail having the same grain sizes as reported in Knezevic et al. [17].

	$\alpha = 1 [1\ 0\ 0](0\ 1\ 0)$	$\alpha = 2 [1\ 0\ 0](0\ 0\ 1)$	$\alpha = 3 \langle 1\ \bar{1}\ 1 \rangle \{1\ 1\ 0\}$	$\alpha = 4 \langle 1\ \bar{1}\ 2 \rangle \{0\ 2\ 1\}$
b^α (nm)	2.85×10^{-1}	2.85×10^{-1}	6.51×10^{-1}	11.85×10^{-1}
κ_1^α (m^{-1})	1.2×10^8	1.0×10^7	2.0×10^7	2.2×10^8
g^α	0.01	0.01	0.01	0.01
D_o^α (MPa)	446	126	70	126
τ_o^α (MPa)	122	266	90	669
q	18	0	4	80

	$\beta = 1\{1\ 3\ 0\}$	$\beta = 2\{1\ 7\ 2\}$
τ_o^β (MPa)	100	500
$C^{\alpha\beta}$, $\alpha = 1$	5500	5500
$C^{\alpha\beta}$, $\alpha = 2$	5500	5500
$C^{\alpha\beta}$, $\alpha = 3$	8500	8500
$C^{\alpha\beta}$, $\alpha = 4$	6800	6100
b^β (nm)	0.1036	1.433

Works Cited

- [1] R. W. Klein, J. R. Einhorn, M. Steiner, C. Calhoun, E. Garlea and S. R. Agnew, "Texture Measurement and Property Prediction of Rolled α -uranium," *Submitting to Computational Materials Science*, 2016.
- [2] C. Whipple and S. Larson, "Medical Isotope Production Without Highly Enriched Uranium," *The National Academies Press*, 2009.
- [3] A. Lokhov, "The Supply of MEditional Radioisotope: Review of Potential Molybdenum-99/Technetium-99m Production Technologies," Nuclear Energy Agency, 2010.
- [4] S. Govindarajan, B. Graybill, P. Makarewicz, Z. Xie and G. Solbrekken, "Assembly and Irradiation Modeling of Residual Stresses in Low-Enriched Uranium Foil-Based Annular Targets for Molybdenum-99 Production," *Science and Technology of Nuclear Installations*, vol. 2013, 2013.
- [5] R. W. Klein, B. W. Williams, J. McKinley, J. R. Einhorn and S. R. Agnew, "Exploration of Thin-walled Magnesium Alloy Tube Extrusion for Improved Crash Performance," in *Magnesium Technology*, Nashville, TN, 2016.
- [6] B. W. Williams, S. R. Agnew, R. W. Klein and J. McKinley, "Development of Thin-Walled Magnesium Alloy Extrusions for Improved Crash Performance Based Upon Texture Control," in *Magnesium Technology 2015*, Hoboken, NJ, John Wiley & Sons, Inc., 2015.
- [7] J. L. Y. & H. H. Yoon, " Investigation of deformation and collapse mechanism for magnesium tube in axial crushing test," *Journal of Mechanical Science and Technology*, vol. 27, no. 10, pp. 2917-2921, 10 2013.
- [8] Y. Chino, K. Sassa and M. Mabuchi, "Enhancement of tensile ductility of magnesium alloy produced by torsion extrusion," *Scripta Materialia*, vol. 59, no. 4, pp. 399-402, 2008.

- [9] D. Orlov, G. Raab, T. Lamark, M. Popov and Y. Estrin, "Improvement of mechanical properties of magnesium alloy ZK60 by integrated extrusion and equal channel angular processing," *Acta Materialia*, vol. 59, no. 1, pp. 375-385, 2011.
- [10] S. Seipp, M. Wagner, K. Hockauf, I. Schneider, L. Meyer and M. Hockauf, "Microstructure, crystallographic texture and mechanical properties of the magnesium alloy AZ31B after different route of thermo-mechanical processing," *International Journal of Plasticity*, vol. 35, pp. 155-166, 2012.
- [11] D. Li, V. Joshi, C. Lavender, M. Khaleel and S. Ahzi, "Yield asymmetry design of magnesium alloys by integrated computational materials engineering," *Computational Materials Science*, vol. 79, pp. 448-455, 2013.
- [12] J. Bohlen, M. Nurnberg, J. Senn, D. Letzig and S. R. Agnew, "The texture and anisotropy of magnesium-zinc-rare earth alloy sheets," *Acta Materialia*, vol. 55, no. 6, pp. 2101-2112, 2007.
- [13] T. Mukai, M. Yamanoi and K. Higashi, "Ductility Enhancement in Magnesium Alloys under Dynamic Loading," *Materials Science Forum*, Vols. 350-351, pp. 97-104, 2000.
- [14] G. Z. J. & D. J. Liu, "FE analysis of metal flow and weld seam formation in a porthole die during the extrusion of a magnesium alloy into a square tube and the effect of ram speed on weld strength," *Journal of materials processing technology*, vol. 200, no. 1, pp. 185-198., 2008.
- [15] M. Knezevic, R. J. McCabe, C. N. Tomé, R. A. Lebensohn, S. R. Chen, C. M. Cady, G. T. Gray III and B. Mihaila, "Modeling mechanical response and texture evolution of α -uranium as a function of strain rate and temperature using polycrystal plasticity," *International Journal of Plasticity*, vol. 43, pp. 70-84, 2013.
- [16] B. Beeler, C. Deo, M. Baskes and M. Okuniewski, "First principles calculations of the structure and elastic constants of α , β , and γ uranium," *J. Nucl. Mater.*, vol. 433, pp. 143-151, 2013.

- [17] M. Knezevic, L. Capolungo, C. N. Tomé, R. A. Lebensohn, D. J. Alexander, B. Mihaila and R. J. McCabe, "Anisotropic stress-strain response and microstructure evolution of textured α -uranium," *Acta Materialia*, vol. 60, no. 2, pp. 702-715, 2012.
- [18] L. Hao, D. Jiang and X. Chen, "Finite element analysis of roll bit behaviors in cold foil rolling process," *AIP Conference Proceedings*, vol. 1532, pp. 478-483, 2013.
- [19] Computational Engineering International Inc., "EnSight User Manual for Version 10.0," Apex, NC, 2012.
- [20] Mathworks, "Condition number with respect to inversion - Mathworks cond," 2016. [Online]. Available:
<http://www.mathworks.com/help/matlab/ref/cond.html?searchHighlight=condition%20number>. [Accessed 18 July 2016].
- [21] Dassault Systemes, *ABAQUS Theory Manual*, Providence, RI, 2011.
- [22] J. Liu, Z. Cui and C. Li, "Modelling of flow stress characterizing dynamic recrystallization for magnesium alloy AZ31B," *Computational Materials Science*, vol. 41, pp. 375-382, 2008.
- [23] K. Turner, G. Solbrekken and C. Allen, "Thermal-Mechanical Analysis of Annular Target Design for High Volume Production of Mo-99 Using LEU," in *Proceedings of the ASME - International Mechanical Engineering Congress & Exposition*, Lake Buena Vista, Florida, USA, 2009.
- [24] C. A. Calhoun, J. A. Wolmershauser, D. W. Mulay, E. Garlea and S. R. Agnew, "Thermal residual strains in deleted α -U.," *Scripta Materialia*, vol. 69, no. 8, pp. 566-569, 2013.
- [25] C. N. Tomé and R. A. Lebensohn, "Manual for Code: Visco-Plastic Self-Consistent," 13 November 2009. [Online]. Available: http://public.lanl.gov/lebenso/VPSC7c_manual.pdf. [Accessed 2015].
- [26] I. J. Beyerlein and et al., "Non-uniform microstructure and texture evolution during equal channel angular extrusion," *Philosophical Magazine*, vol. 85, pp. 1359-1394, 2005.

- [27] S. R. Agnew and et al., "Crystallographic Texture Evolution of Three Wrought Magnesium Alloys During Equal Channel Angular Extrusion," *Materials Science and Engineering A*, vol. 408, pp. 72-78, 2005.
- [28] E. Orowan, "The Calculation of Roll Pressure in Hot and Cold Flat Rolling," *Institution of Mechanical Engineers*, vol. 150, no. 1, pp. 140-167, 1943.
- [29] E112-13, ASTM Standard, "Standard Test Methods for Determining Average Grain Size," ASTM International, Materials Park, OH, 2013.
- [30] I. J. Beyerlein and C. N. Tomé, "A dislocation-based constitutive law for pure Zr including temperature effects," *International Journal of Plasticity*, vol. 24, pp. 867-895, 2008.
- [31] M. Zecevic, M. Knezevic, I. J. Beyerlein and R. J. McCabe, "Texture formation in orthorhombic alpha-uranium under simple compression and rolling to high strains," *Journal of Nuclear Materials*, vol. 473, pp. 143-156, 2016.
- [32] L. Lloyd and M. Mueller, "Recrystallization in Rolled Uranium Sheet," Argonne National Laboratory, Argonne, Illinois, 1962.
- [33] E. S. Fisher, "Temperature dependence of the elastic moduli in alpha uranium single crystals (298 to 923 K)," Metallurgy Division, Argonne National Laboratory, Argonne, Illinois, USA, 2003.
- [34] N. Stanford, D. Atwell, A. Beer, C. Davies and M. R. Barnett, "Effect of microalloying with rare-earth elements on the texture of extruded magnesium-based alloys," *Scripta Materialia*, vol. 59, no. 7, pp. 772-775, 2008.
- [35] J. J. Bhattacharyya, F. Wang, P. D. Wu, W. R. Whittington, H. E. Kadiri and S. R. Agnew, "Demonstration of alloying, thermal activation, and latent hardening effects on quasi-static and dynamic polycrystal plasticity of Mg alloy, WE43-T5, plate," *International Journal of Plasticity*, vol. 81, pp. 123-151, 2016.

- [36] A. Soulami, C. Lavender, D. Paxton and D. Burkes, "Rolling Process Modeling Report: Finite-Element Prediction of Roll-Separating Force and Rolling Defects," Pacific Northwest National Laboratory, 2014.
- [37] P. Montmitonnet, R. Loge, M. Hamery, Y. Chastel, J.-L. Doudoux and J.-L. Aubin, "3D elastic-plastic finite element simulation of cold pilgering of zircaloy tubes," *Journal of Materials Processing Technology*, Vols. 125-126, pp. 814-820, 2002.
- [38] C. McConnell and J. Lenard, "Friction in cold rolling of a low carbon steel with lubricants," *Journal of Materials Processing Technology*, vol. 99, no. 1-3, pp. 86-93, 2000.
- [39] J. G. Lenard, "The effect of lubricant additives on the coefficient of friction in cold rolling," *J. Mater. Process. Technol.*, Vols. 80-81, pp. 232-238, 1998.
- [40] J. L. Snelgrove, G. L. Hofman, T. C. Wiencek, C. T. Wu, G. F. Vandegrift, S. Aase, B. A. Buchholz, D. J. Dong, R. A. Leonard, B. Srinivasan, D. Wu, A. Suropto and Aliluddin, "Development and Processing of LEU Targets for Mo-99 Production - Overview of ANL Program," Argonne National Laboratory, 1995.
- [41] P. Makarewitz and G. Solbrekken, "Thermal/Mechanical/Hydraulic Experimental Tools for Mo-99 Production Target Analysis," University of Missouri, 2013.
- [42] P. A. Turner and C. N. Tomé, "A study of residual stresses in Zircaloy-2 with rod texture," *Acta metallurgica et Materialia*, vol. 42, no. 12, pp. 4143-4153, 1994.